Understanding molecular and cellular processes using statistical physics

Zhanghan Wu

Dissertation submitted to the faculty of the
Virginia Polytechnic Institute and State University
in partial fulfillment of the requirements for the degree of

Doctor of Philosophy
in
Genetics, Bioinformatics and Computational Biology

Jianhua Xing, chair
Yang Cao
Daniela Cimini
Richard A. Walker

May 4, 2011
Blacksburg, Virginia

Keywords: Mathematical Modeling, Microtubule Dynamics, Enzyme Conformational Changes, Single Molecular Fluctuations

Understanding molecular and cellular processes using statistical physics

Zhanghan Wu

Abstract

Using statistical physics principles to solve problems in biology is one of the most promising directions due to the complexity and non-equilibrium fluctuations in biological systems. In this work, we try to describe the dynamics at both cellular and molecular levels. Microtubule dynamics and dynamic disorder of enzyme proteins are two of the examples we investigated. The dynamics of microtubules and the mechanical properties of these polymers are essential for many key cellular processes. However, critical discrepancies between experimental observations and existing models need to be resolved before further progress towards a complete model can be made. We carried out computational studies to compare the mechanical properties of two alternative models, one corresponding to the existing, conventional model, and the other considering an additional type of tubulin lateral interaction described in a cryo-EM structure of a proposed trapped intermediate in the microtubule assembly process. Our work indicates that a class of sheet structures is transiently trapped as an intermediate during the assembly process in physiological conditions. In the second part of the work, we analyzed enzyme slow conformational changes in the context of regulatory networks. A single enzymatic reaction with slow conformational changes can serve as a basic functional motif with properties normally discussed with larger networks in the field of systems biology. The work on slow enzyme dynamics fills the missing gap between studies on intramolecular and network dynamics. We also showed that enzyme fluctuations could be amplified into fluctuations in phosphorylation networks. This can be used as a novel biochemical “reporter” for measuring single enzyme conformational fluctuation rates.

DEDICATION

This dissertation is first dedicated to my family, my wife Rongman Cai and my daughter Magnolia C. Wu, who provided constant and unyielding support during the whole process of application, study, research and graduation. Nothing would be achieved without their help and encouragement.

Also to my parents, Qingyuan Zhang and Chuanfan Wu, all the teachers I had, and all the people that inspired me to be a scientist. Without them, this dissertation would have never been possible.

ACKNOWLEDGEMENT

First of all, I would like to thank my advisor Dr. Jianhua Xing for his support, patience, and encouragement throughout my graduate studies Dr. Xing has been my inspiration as I hurdle all the obstacles in the completion this research work.

I am grateful to my committee members, Dr. Yang Cao, Dr. Daniela Cimini and Dr. Richard A. Walker for providing many valuable comments that improved the presentation and contents of the dissertation.

I am also grateful to my colleagues from the Xing lab, Yan Fu, Ping Wang and Xiaoshan Jiang, for their interesting and good-spirited discussions relating to this research.

Table of Contents

List of Figures

List of Tables

.

Chapter 1

Introduction and Literature review

a. Introduction

Biological systems are complex. The interactions at different levels, genetic, molecular and cellular and even intercellular are all complicated. At each level, there could be thousands of interactions. Even worse, there are fluctuations (noises, in other words) involved literally everywhere. To extract information from complex systems, we need powerful tools to perform the work. In fact, statistical physics was born to solve the problems in complex systems with equilibrium or non-equilibrium fluctuations. Although statistical physics was originally used to solve physical problems, it would be of great significance if one could formulate biological problems so that existing techniques and methods from statistical physics could be used. In fact, there are more and more research efforts along this direction. Using statistical physics principles to solve problems in biology is one of the most promising directions due to the complexity and non-equilibrium fluctuations in biological systems. We utilized some of the principles and techniques to address two problems in biological field: microtubule dynamics and fluctuations of single molecules.

b. Microtubule (MT) dynamics

Microtubules are one of the three major cytoskeleton components in eukaryotic cells [1-3]. They are hollow cylinders consisting of about 13 parallel protofilaments (PF)

formed by the head-to-tail assembly of $\alpha\beta$-tubulin heterodimers (Figure 1.1a). The outer and inner diameter of microtubules are about 25 nm and 15nm, respectively, whereas the length can vary from tens of nanometers to tens or even hundreds of micrometers, frequently spanning the whole cell. Microtubules are one of the major parts to build the framework of cells. They play important roles in many eukaryotic cellular processes, including intracellular transport, cell motility, mitosis and meiosis. Microtubule dynamic instability is known to be a key property for microtubule function. The regulation of microtubule dynamics has been shown to be both of great biological significance during cell division, and of outstanding pharmaceutical value in tumor therapy. Various proteins interact with MTs for their precise cell regulation and function. In brief, microtubules act as mechanical support for cells and as both the stage and players in many important cellular processes.

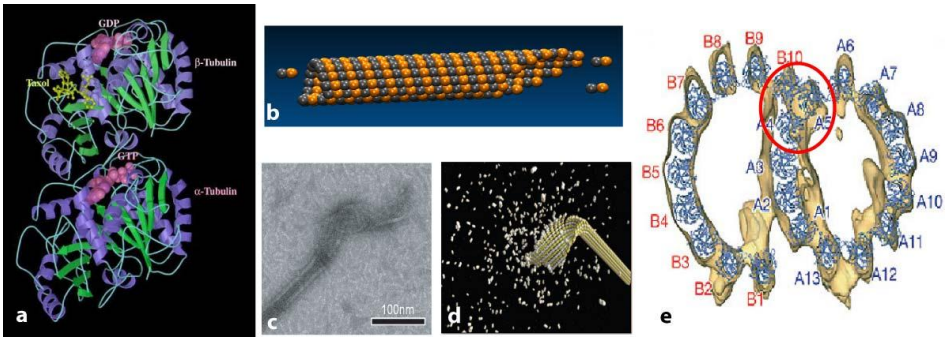

Figure 1.1 **Basic facts about Microtubules**. (a) Atomic crystal structure of the tubulin dimer (Adapted from [5]). (b) Schematic illustration of the MT with tubulin dimer direct-addition model. The sheet structure is explained as an incomplete portion of an MT (the right end in the figure). This explanation has been adopted in general biology textbooks and in many existing model studies [2, 6]. (c) Cryo-EM image of a growing MT shows a long helical sheet structure. (Adapted from [7]). (d) The sheet-intermediate model (reproduced from [8]). No detailed

theoretical analysis exists for this model. (e) Cryo-EM based doublet structure shows a PF interacting with two other PFs simultaneously (circled tubulins) resembling the two types of lateral bonds found in the ribbon structure. (Reproduced from [9]).

Many common diseases are found to be strongly related to the malfunctioning of MT assembly. Huntington's disease (HD) is an autosomal dominant inherited neuro-degenerative disease presenting progressive involuntary movements and cognitive changes. Its gene product has been shown to interact with polymerized MT [10]. Depolymerization of MTs by toxins such as rotenone disrupts vesicular transport and is found to be related to neurodegenerative diseases such as Parkinson's and Alzheimer's disease [11-14]. Down syndrome, one kind of severe genetic disease, is known to be caused by chromosome missegregation which may be due to mitotic spindle MT defects or defects in MT-chromosome binding. MTs and their associated proteins are often serve as therapy targets [15]. For instance, Taxol® is one famous drug targeting MTs. It disrupts cancer cell division by interfering with microtubule disassembly. MT-stablizing drugs are also used in Alzheimer's disease treatment [16, 17].

In the past decades, there has been extensive study in this field, but the nano-mechanical properties and assembly mechanism of MTs are still not fully understood and some parts of them are highly controversial. The most simplistic textbook model for MT assembly is described as $\alpha\beta$-tubulin hetero-dimers added one by one onto the growing end of a MT (Figure 1.1)) [18, 19]. However, experimental evidence indicates that the MT forms open sheet structure at the plus end of MT during the assembly. In fact, the sheet structure during MT assembly is actually not newly found. As early as the 1970s, Erickson reported the presence of an intermediate sheet structure in MT

assembly process [20]. Other researchers confirmed this observation later [21-23]. In 1995, Chretien and coworkers observed that fast growth of existing MTs occurs via the elongation of an outwardly curved sheet-like structure at the growing end of the MT [24]. The conventional explanation of the sheet-like structure is that it is an incomplete portion of the MT lattice at growing stage (Figure 1.1b) [25-27]. However, systematic model studies of VanBuren et al. reach different conclusions (see below) [26]. They argue that the sheet-like structure is due to the unfinished disassembly process and MTs at the growing stage most likely have blunt end.

Bending resistance is another important property of MTs for many of their functions. MTs form the mitotic spindle during mitosis process in cell. Many unicellular eukaryotic organisms and also many cells of higher eukaryotes (such as sperm cells or lung epithelial cells) possess cilia or flagella, specialized MT-based structures, to propel themselves or to pump fluid. MTs also form the core of neuronal axons. The MTs are bent in the conditions mentioned above. The responses of the MT mechanical properties have been investigated extensively in recently years [28-49]. However, the non-linear responses of the MT bending or buckling are not fully understood. Moreover, the linear mechanical properties of MT under various conditions (different binding proteins, different assembly conditions, etc.) are still under debate. For instance, the fine values of the Young's modulus of pure MTs and Taxol treated MTs are still under investigation. Different labs have reached different conclusions on which type of MTs have higher Young's modulus [28, 42-46]. Even for the same type of MTs, a difference of as much as two orders of magnitude was found in different experiments (see Table 1.1 part of the measured results).

Table 1.1 Flexural Rigidity Measurements

Microtubules	Methods	Flexural Rigidity (x 10^{-24} Nm^2)	Temperature (^0C)	References
Pure MT	Buckling force	7.9	33	[43]
	Hydrodynamic flow	8.5	37	[44]
	Hydrodynamic flow	35.8	37	[29]
	Relaxation (RELAX)	3.7	22-25	[45]
	Relaxation	4.7	22-25	[45]
	(WIGGLE)	26.0	37	[46]
	Thermal fluctuation	4.6	37	[44]
	Thermal fluctuation	26.5*	37	[29]
	Thermal fluctuation	18.5		[47]
	Thermal fluctuation	13.7-27.0*	23	[33]
	Thermal fluctuation			
Paclitaxel-	Buckling force	2.0	33	[43]
stabilized MT	Buckling force	2.0-22	37	[28]
	Relaxation (RELAX)	1.0	22-25	[45]
	Relaxation	1.9	22-25	[45]
	(WIGGLE)	21.5	25	[45]
	Thermal fluctuation	32.0	37	[46]
	Thermal fluctuation	2.4	37	[44]
	Thermal fluctuation		37	[48]
	Thermal fluctuation		37	[49]
	Electric force			

*These values of EI were derived from measured persistence length l_p with $EI = k_B T \cdot l_p$.

One breakthrough in the field happened in 2005, when Wang and Nogales reconstructed the structure of a curved sheet of nonhydrolyzable GTP-tubulin stabilized

by low temperature and a high concentration of magnesium (henceforth called the ribbon structure, Figure 1.1)[8, 35]. This ribbon structure was able to directly convert into MTs when the temperature was raised. The authors observed two types of lateral interactions between two tubulins from two neighboring PFs in this structure: one type was indistinguishable from those in MTs, which we call the tube bond, and the other was a new type, which we call the sheet bond [50, 51]. Here we call a noncovalent contact as a bond to follow the convention in the field [52]. Actually structures at lower resolution showing alternative lateral bonds have been obtained before [53]. Wang and Nogales proposed that the ribbon structure was related to the sheet structure observed during MT assembly under normal conditions. This proposal received some skepticism and was not given sufficient attention since the structure was obtained under conditions that were far from physiological: low temperature (4-15^{o}C instead of 37˚C), nonhydrolyzable GTP, and remarkably high Mg^{2+} concentration (8-30 mM instead of ~2 mM). However, another series of experiments in the field of MT mechanical properties provides strong evidence that the sheet bond exists under normal physiological conditions [54, 55]. The non-linear response of MTs to atomic force microscope tip pressure suggests the existence of second lateral interaction.

MT assembly dynamics involve the interplay between intra- and inter-molecular properties and is affected by many cellular factors. Also, the nature of the system prevents direct experimental studies. For example, mutagenesis studies can't be easily performed. Most of the information about the system that we have now is derived indirectly. Therefore, mathematical modeling plays a crucial role in this field [25, 27, 56-66]. For example, Molodtsov et al. and VanBuren et al. constructed detailed models

describing the chemical-mechanical coupling and resultant structural and dynamical properties of MTs [26, 67].

In summary, studying the MT assembly/disassembly process and how MT-associated proteins affect the dynamics of this process is of fundamental importance to understanding the related disease mechanisms and for developing corresponding treatments. Based on the experimental evidence of lateral sheet bond, it is necessary and important to build a mathematical model to include this novel type of tubulin interaction - sheet bond - which has not been systematically studied. This research has the potential to not only modify our current knowledge of this important cellular process, but may also lead to new directions for drug development [50].

c. Dynamic disorder

Michaelis-Menten and Non-Michaelis-Menten kinetics: Rate processes are ubiquitous in chemical, physical, and biological processes. Michaelis-Menten kinetics has been a more than century-long central topic in chemical physics. If asked what is the most important mathematical equation he/she knows, a biochemist most likely suggests the Michaelis-Menten equation. For a typical enzymatic reaction $S + E \underset{k_{-1}}{\overset{k_1}{\rightleftarrows}} \mathrm{E}S \xrightarrow{k_2} E + P$, one has (after certain mathematical approximations)

$$\frac{d[P]}{dt} = \frac{k_2[E]_t[S]}{(k_{-1} + k_2)/k_1 + [S]}. \qquad (1)$$

A key idea here is that each step is characterized by a rate constant.

Most of enzymatic reactions are assumed to follow the hyperbolic Michaelis-Menten

kinetics. However, violations of the hyperbolic relation have also long been known. A large amount of experimental and theoretical investigations have been devoted to understand the non-Michaelis-Menten (NMM) kinetics (we only refer to two reviews [68, 69]). It has long been suggested that the NMM kinetics has cellular regulatory functions [69]. Carl Frieden in fact had introduced the concept of hysteretic enzyme as early as 1970, and since then a sizable literature exists on the enzyme behavior. He also noticed that most of the hysteretic enzymes are regulatory proteins. However, true roles of hysteretic enzymes in cellular regulations are elusive, and yet to be defined and explored (with some exceptions on hysteretic enzyme induced oscillations [70, 71]). We suggest that they can be fully appreciated only being placed at the broader context of regulatory networks.

One of the reasons of the current state of affair, we suggest, is due to a lack of experimental data and theoretical understanding in the "intermediate regime" between single-molecule investigations of individual enzymes (relatively simple) and cellular dynamics (too complex). This realization led us to first focus on the behavior of small cellular network of proteins and enzymes with slow dynamic disorder. In pursuing this line of inquiry, we re-discovered another key behavior of slow conformational dynamic disorder: the mnemonic behavior championed by the French scientist J. Richard and his colleagues [72, 73]. The mnemonic and hysteretic concepts, though both consequences of slow conformational disorder, are distinctly different: one emphasizes the steady-state and one emphasizes the transient kinetics leading to steady state. To further elucidate and compare these issues is a necessary theoretical step toward a true, comprehensive understanding of the consequence of dynamics disorder in cellular

regulatory dynamics.

To understand these observations, it is proposed that proteins may convert slowly between different conformers with different enzymatic activity (see the discussion on dynamic disorder below). Recently, the slow inter-conversion of different conformers has been observed directly through single-molecule enzymology techniques (see the discussion below)[74-76].

We want to emphasize that the concept “hysteresis” has a different meaning in the usual context of network dynamics [77]. A hysteretic enzyme may not be involved in a dynamic hysteresis loop, and a dynamic hysteresis loop may not involve any hysteretic enzymes.

Dynamic disorder: A related phenomenon called dynamic disorder has also been discussed extensively in the physical chemistry and biophysics communities. What is “dynamic disorder”? A molecule fluctuates constantly at finite temperature. Reaction coordinate (RC) is an important concept in chemical rate theories [78]. The RC is a special coordinate in the configurational space (expanded by the spatial coordinates of all the atoms in the system), which leads the system from the reactant configuration to the product configuration. A fundamental assumption in most rate theories (such as the transition state theory) states that the dynamics along the RC are much slower than fluctuations along all other coordinates. Consequently for any given RC position, one may assume that other degrees of freedom approach approximately equilibrium, the so-called adiabatic approximation. Deviation from this assumption is treated as secondary correction [79]. Chemical rate theories based on this assumption are remarkably successful on explaining the dynamics involving small molecules. The dynamics of a

system can be well characterized by a rate constant. However, it is more complicated for macromolecules like proteins, RNAs, and DNAs. Macromolecules have a large number of atoms and possible conformations. The conformational fluctuation time scales of macromolecules span from tens of femtoseconds to hundreds of seconds [80]. Consequently, conformational fluctuations can be comparable or even slower than the process involving chemical bond breaking and formation. The adiabatic approximation seriously breaks down in this case. If one focuses on the dynamics of processes involving chemical reactions, the familiar concept of “rate constant” no longer holds. Dynamic disorders refer to the phenomena that the ‘rate constant’ of a process is actually a random function of time, and is affected by some slow protein conformational motions [81, 82]. Since the pioneering work of Frauenfelder and coworkers on ligand binding to myoglobin [83], extensive experimental and theoretical studies have been performed on this subject (see for example ref. [82] for further references). Recently, existence of dynamic disorders has been demonstrated directly through single molecule enzymology measurements [74, 76, 84]. For example, Xie and coworkers showed that the turnover time distribution of one β-galactosidase molecule spans several orders of magnitude (10^{-3} s to 10 s). It is also shown that under certain conditions dynamic disorder results in non-Michaelis-Menten kinetics [85]. *Single molecule measures on several enzymes suggest that the existence of dynamic disorder in biomolecules is a rule rather than exception [86]*. *An important question to ask is what is the biological consequence of the existence of dynamic disorder*.

Combining several reactions together, one can form reaction networks with emerging dynamic behaviors such as switches, oscillators, etc, and ultimately the life

form [87, 88]. With the idea of systems biology becoming popular, a modeler may deal with hundreds to thousands ordinary differential rate equations describing various biological processes. The hope is that by knowing the network connectivity and associated rate constants (which requires daunting experimental efforts), one can reveal the secret of life and even perform manipulations.

However, one seldom asks a basic question**:** *is it legitimate to use the usual rate equation formalism to model biological networks*? If not, there is a danger of basing our studies on a wrong or poorly-justified assumption, and the results may be misleading.

Many *in vivo* processes involve small numbers of substrate molecules. When the number is in the range of hundreds or even smaller, stochastic effect becomes important. Chemical reactions take place stochastically rather than deterministically. Then one should track the discrete numbers of individual species explicitly in the rate equation formalism. Many studies have shown that one might make erroneous conclusions without considering the stochastic effect [89, 90]. Noise propagation through a network is currently an important research topic [90-98]. One usually assumes that the stochastic effect mainly arises from a small number of identical molecules, and rate constants are still assumed to be well defined.

With the existence of dynamic disorder, the activity of a single enzyme is a varying quantity. This adds another noise source with unique (multi-time scale, non-white noise) properties. For bulk concentrations, fluctuations due to dynamic disorder are suppressed by averaging over a large number of molecules. However, existence of NMM kinetics can still manifest itself in a network. If there are only a small number of protein molecules, as in many *in vivo* processes, with MM or NMM kinetics, dynamic

disorder will affect the network dynamics. It matters if the reaction time scale associated with a specific molecule at a given time is 10^{-3} s or 10 s. The conventionally considered stochastic effect is mainly due to small numbers of identical molecules. Here a new source of stochastic effect arises from small numbers of molecules with the same chemical structure but different conformations. Dynamic disorder induced stochastic effect has some unique properties, which require special theoretical treatment, and may result in novel dynamic behaviors (see the preliminary results below). First, direct fluctuation of the rate constants over several orders of magnitude may have dramatic effects on the network dynamics. Second, the associated time scales have broad range (see above). The Gaussian white noise approximation is widely used in stochastic modeling of network dynamics with the assumption that some processes are much faster than others. Existence of broad time scale distribution makes the situation more complicated. Furthermore, a biological system may actively utilize this new source of noise. Noises from different sources may not necessarily add up. Instead they may cancel each other and result in smaller overall fluctuations [90, 95]. We expect that the existence of dynamic disorder not only further complicates the situation, but may also provide additional degrees of freedom for regulation since the rates can be continuously tuned. Especially we expect that existence of dynamic disorder may require dramatic modification on our understanding of signal transduction networks. Many of these processes involve small numbers of molecules, have short time scales (within minutes), and have high sensitivity and specificity (responding to specific molecules only).

A biological network usually functions in a noisy ever-changing environment. Therefore, the network should be: 1) robust ─ functioning normally despite environment

noises; 2) adaptive ─ the tendency to function optimally by adjusting to the environment; 3) sensitive ─ sharp response to the regulating signals. It is not-fully understood as to how a biological network can achieve these requirements. Previous research emphasizes that the dynamic properties of a network are closely related to its topology. In this work we will systematically examine the largely overlooked coupling between molecular level dynamic properties and network level dynamics.

d. References

1. Alberts, B., et al., *Molecular Biology of the Cell*. 4d ed2002, New York: Garland.
2. Howard, J., *Mechanics of Motor Proteins and the Cytoskeleton*. 1st ed2001, Sunderland, MA: Sinauer.
3. Desai, A. and T.J. Mitchison, *Microtubule polymerization dynamics.* Annu.Rev. Cell Dev. Biol., 1997. **13**: p. 83-117.
4. Frieden, C., *Kinetic Aspects of Regulation of Metabolic Processes. The hysteretic enzyme concept.* J. Biol. Chem., 1970. **245**(21): p. 5788-5799.
5. Nogales, E., S.G. Wolf, and K.H. Downing, *Structure of the alpha beta tubulin dimer by electron crystallography.* Nature, 1998. **391**(6663): p. 199-203.
6. VanBuren, V., L. Cassimeris, and D.J. Odde, *Mechanochemical model of microtubule structure and self-assembly kinetics.* Biophys J, 2005. **89**(5): p. 2911-26.
7. Wang, H.-W. and E. Nogales, *Nucleotide-dependent bending flexibility of tubulin regulates microtubule assembly.* Nature, 2005. **435**(7044): p. 911-915.

8. Wang, H.W., et al., *Assembly of GMPCPP-bound tubulin into helical ribbons and tubes and effect of colchicine.* Cell Cycle, 2005. **4**(9): p. 1157-60.
9. Sui, H. and K.H. Downing, *Molecular architecture of axonemal microtubule doublets revealed by cryo-electron tomography.* Nature, 2006. **442**(7101): p. 475-478.
10. Tukamoto, T., et al., *Huntington's disease gene product, huntingtin, associates with microtubules in vitro.* Mol. Brain Res., 1997. **51**(1-2): p. 8-14.
11. Drewes, G., A. Ebneth, and E.-M. Mandelkow, *MAPs, MARKs and microtubule dynamics.* Trends in Biochemical Sciences, 1998. **23**(8): p. 307-311.
12. Iqbal, K., et al., *Defective brain microtubule assembly in Alzheimer's disease.* The Lancet, 1986. **328**(8504): p. 421-426.
13. Forno, L.S., *Neuropathology of Parkinson's Disease.* J. Neuropathol Exp Neurol, 1996. **55**(4): p. 259-272.
14. Dauer, W. and S. Przedborski, *Parkinson's Disease: Mechanisms and Models.* Neuron, 2003. **39**(6): p. 889-909.
15. Fojo, T., ed. *The role of microtubules in cell biology, neurobiology, and oncology*. Cancer drug discovery and development, ed. B.A. Teicher2008, Humana Press. 587.
16. Ballatore, C., V.M.Y. Lee, and J.Q. Trojanowski, *Tau-mediated neurodegeneration in Alzheimer's disease and related disorders.* Nat Rev Neurosci, 2007. **8**(9): p. 663-672.
17. Skovronsky, D.M., V.M.Y. Lee, and J.Q. Trojanowski, *Neurodegenerative diseases: New concepts of pathogenesis and their therapeutic implications.* Annu Rev Pathol Mech Dis, 2006. **1**(1): p. 151-170.
18. Summers, K. and M.W. Kirschner, *Characteristics of the polar assembly and disassembly of microtubules observed in vitro by darkfield light microscopy.* J. Cell Biol., 1979. **83**(1): p. 205-217.

19. Bergen, L.G. and G.G. Borisy, *Head-to-tail polymerization of microtubules in vitro. Electron microscope analysis of seeded assembly.* J. Cell Biol., 1980. **84**(1): p. 141-150.
20. Erickson, H.P., *Microtubule surface lattice amd subunit structure and observations on reassembly.* J. Cell Biol., 1974. **60**(1): p. 153-167.
21. Detrich, H.W., et al., *Mechanism of microtubule assembly. Changes in polymer structure and organization during assembly of sea urchin egg tubulin.* J. Biol. Chem., 1985. **260**(16): p. 9479-9490.
22. Simon, J. and E. Salmon, *The structure of microtubule ends during the elongation and shortening phases of dynamic instability examined by negative-stain electron microscopy.* J Cell Sci, 1990. **96**(4): p. 571-582.
23. Kirschner, M.W., L.S. Honig, and R.C. Williams, *Quantitative electron microscopy of microtubule assembly in vitro.* J. Mol. Biol., 1975. **99**(2): p. 263-276.
24. Chretien, D., S.D. Fuller, and E. Karsenti, *Structure of growing microtubule ends - 2-dimensional sheets close into tubes at variable rates.* J. Cell. Biol., 1995. **129**(5): p. 1311-1328.
25. Jánosi, I.M., D. Chrétien, and H. Flyvbjerg, *Modeling elastic properties of microtubule tips and walls.* Eur. Biophys. J, 1998. **27**(5): p. 501-513.
26. VanBuren, V., L. Cassimeris, and D.J. Odde, *Mechanochemical Model of Microtubule Structure and Self-Assembly Kinetics.* Biophys. J., 2005. **89**(5): p. 2911-2926.
27. Erickson, H.P. and D. Pantaloni, *The role of subunit entropy in cooperative assembly. Nucleation of microtubules and other two-dimensional polymers.* Biophys. J., 1981. **34**(2): p. 293-309.
28. Kurachi, M., M. Hoshi, and H. Tashiro, *Buckling of a single microtubule by optical trapping forces: Direct measurement of microtubule rigidity.* Cell Motility and the Cytoskeleton, 1995. **30**(3): p. 221-228.

29. Kurz, J.C. and R.C. Williams, Jr., *Microtubule-associated proteins and the flexibility of microtubules.* Biochemistry, 1995. **34**(41): p. 13374-80.
30. Chretien, D., H. Flyvbjerg, and S.D. Fuller, *Limited flexibility of the inter-protofilament bonds in microtubules assembled from pure tubulin.* Eur Biophys J, 1998. **27**(5): p. 490-500.
31. Odde, D.J., et al., *Microtubule bending and breaking in living fibroblast cells.* J Cell Sci, 1999. **112 (Pt 19)**: p. 3283-8.
32. Janosi, I.M., D. Chretien, and H. Flyvbjerg, *Structural microtubule cap: stability, catastrophe, rescue, and third state.* Biophys J, 2002. **83**(3): p. 1317-30.
33. Janson, M.E. and M. Dogterom, *A bending mode analysis for growing microtubules: evidence for a velocity-dependent rigidity.* Biophys J, 2004. **87**(4): p. 2723-36.
34. Needleman, D.J., et al., *Radial compression of microtubules and the mechanism of action of taxol and associated proteins.* Biophys J, 2005. **89**(5): p. 3410-23.
35. Wang, H.W. and E. Nogales, *Nucleotide-dependent bending flexibility of tubulin regulates microtubule assembly.* Nature, 2005. **435**(7044): p. 911-5.
36. Bathe, M., et al., *Cytoskeletal bundle bending, buckling, and stretching behavior.* arXiv.org, 2006. **arXiv:q-bio/0607040v2**.
37. Li, C., C.Q. Ru, and A. Mioduchowski, *Torsion of the central pair microtubules in eukaryotic flagella due to bending-driven lateral buckling.* Biochemical and Biophysical Research Communications, 2006. **351**(1): p. 159-164.
38. van den Heuvel, M.G., M.P. de Graaff, and C. Dekker, *Molecular sorting by electrical steering of microtubules in kinesin-coated channels.* Science, 2006. **312**(5775): p. 910-4.
39. Brangwynne, C.P., F.C. MacKintosh, and D.A. Weitz, *Force fluctuations and polymerization dynamics of intracellular microtubules.* Proc Natl Acad Sci U S A, 2007. **104**(41): p. 16128-33.

40. Heussinger, C., M. Bathe, and E. Frey, *Statistical mechanics of semiflexible bundles of wormlike polymer chains.* Phys Rev Lett, 2007. **99**(4): p. 048101.
41. Munson, K.M., P.G. Mulugeta, and Z.J. Donhauser, *Enhanced Mechanical Stability of Microtubules Polymerized with a Slowly Hydrolyzable Nucleotide Analogue.* The Journal of Physical Chemistry B, 2007. **111**(19): p. 5053-5057.
42. Sept, D. and F.C. MacKintosh, *Microtubule elasticity: connecting all-atom simulations with continuum mechanics.* Phys Rev Lett, 2010. **104**(1): p. 018101.
43. Kikumoto, M., et al., *Flexural Rigidity of Individual Microtubules Measured by a Buckling Force with Optical Traps.* Biophysical Journal, 2006. **90**(5): p. 1687-1696.
44. Venier, P., et al., *Analysis of microtubule rigidity using hydrodynamic flow and thermal fluctuations [published erratum appears in J Biol Chem 1995 Jul 14;270(28):17056].* Journal of Biological Chemistry, 1994. **269**(18): p. 13353-13360.
45. Felgner, H., R. Frank, and M. Schliwa, *Flexural rigidity of microtubules measured with the use of optical tweezers.* Journal of Cell Science, 1996. **109**(2): p. 509-516.
46. Mickey, B. and J. Howard, *Rigidity of microtubules is increased by stabilizing agents.* The Journal of Cell Biology, 1995. **130**(4): p. 909-917.
47. Cassimeris, L., et al., *XMAP215 is a long thin molecule that does not increase microtubule stiffness.* Journal of Cell Science, 2001. **114**(16): p. 3025-3033.
48. Pampaloni, F., et al., *Thermal fluctuations of grafted microtubules provide evidence of a length-dependent persistence length.* Proc Natl Acad Sci U S A, 2006. **103**(27): p. 10248-53.
49. Van den Heuvel, M.G., M.P. de Graaff, and C. Dekker, *Microtubule curvatures under perpendicular electric forces reveal a low persistence length.* Proc Natl Acad Sci U S A, 2008. **105**(23): p. 7941-6.

50. Nogales, E. and H.W. Wang, *Structural intermediates in microtubule assembly and disassembly: how and why?* Curr. Op. Cell Biol., 2006. **18**(2): p. 179-184.
51. Wu, Z., et al., *Simulations of Tubulin Sheet Polymers as Possible Structural Intermediates in Microtubule Assembly.* PLoS ONE, 2009. **4**(10): p. e7291.
52. VanBuren, V., D.J. Odde, and L. Cassimeris, *Estimates of lateral and longitudinal bond energies within the microtubule lattice.* Proc Natl Acad Sci U S A, 2002. **99**(9): p. 6035-40.
53. Burton, P.R. and R.H. Himes, *Electron microscope studies of pH effects on assembly of tubulin free of associated proteins. Delineation of substructure by tannic acid staining.* J. Cell Biol., 1978. **77**(1): p. 120-133.
54. de Pablo, P.J., et al., *Deformation and collapse of microtubules on the nanometer scale.* Phys Rev Lett, 2003. **91**(9): p. 098101.
55. Schaap, I.A., et al., *Elastic response, buckling, and instability of microtubules under radial indentation.* Biophys J, 2006. **91**(4): p. 1521-31.
56. Zong, C., et al., *Nonequilibrium self-assembly of linear fibers: microscopic treatment of growth, decay, catastrophe and rescue.* Phys. Biol., 2006. **3**(1): p. 83.
57. Bayley, P., M. Schilstra, and S. Martin, *Microtubule dynamic instability: numerical simulation of microtubule transition properties using a Lateral Cap model.* J Cell Sci, 1990. **95**(1): p. 33-48.
58. Mogilner, A. and G. Oster, *The polymerization ratchet model explains the force-velocity relation for growing microtubules.* Eur. Biophys. J, 1999. **28**(3): p. 235-242.
59. van Doorn, G.S., et al., *On the stall force for growing microtubules.* Eur. Biophys. J, 2000. **29**(1): p. 2-6.
60. Gardner, M.K., et al., *Microtubule assembly dynamics: new insights at the nanoscale.* Curr. Op. Cell Biol., 2008. **20**(1): p. 64-70.

61. Sept, D. and F.C. MacKintosh, *Microtubule elasticity: connecting all-atom simulations with continuum mechanics.* Phys. Rev. Lett., 2010. **104**: p. 018101.
62. Sept, D., N.A. Baker, and J.A. McCammon, *The physical basis of microtubule structure and stability.* Pro. Sci., 2003. **12**(10): p. 2257.
63. Buxbaum, R.E. and S.R. Heidemann, *A thermodynamic model for force integration and microtubule assembly during axonal elongation.* J. Theor. Biol., 1988. **134**(3): p. 379-390.
64. Hill, T.L., *Microfilament or microtubule assembly or disassembly against a force.* Proc Natl Acad Sci U S A, 1981. **78**(9): p. 5613-7.
65. Kolomeisky, A.B. and M.E. Fisher, *The growth of microtubules against an external force.* Biophys. J., 2001. **80**(1): p. 514a-514a.
66. Kolomeisky, A.B. and M.E. Fisher, *Force-velocity relation for growing microtubules.* Biophys. J., 2001. **80**(1): p. 149-154.
67. Molodtsov, M.I., et al., *A molecular-mechanical model of the microtubule.* Biophys. J., 2005. **88**(5): p. 3167-3179.
68. Neet, K.E. and G.R. Ainslie, Jr., *Hysteretic enzymes.* Methods Enzymol., 1980. **64**: p. 192-226.
69. Frieden, C., *Slow Transitions and Hysteretic Behavior in Enzymes.* Ann. Rev. Biochem., 1979. **48**(1): p. 471-489.
70. Roussel, M.R., *Slowly reverting enzyme inactivation: a mechanism for generating long-lived damped oscillations.* J. Theor. Biol., 1998. **195**: p. 233-244.
71. Masson, P., et al., *Damped oscillatory hysteretic behaviour of butyrylcholinesterase with benzoylcholine as substrate* FEBS Lett, 2004. **271**(1): p. 220-234.
72. Cornish-Bowden, A. and M.L. Cardenas, *Co-operativity in monomeric enzymes.* J. Theor. Biol., 1987. **124**(1): p. 1-23.

73. Ricard, J. and A. Cornish-Bowden, *Co-operative and allosteric enzymes: 20 years on.* Eur. J. Biochem., 1987. **166**(2): p. 255-272.

74. Min, W., et al., *Observation of a power-law memory kernel for fluctuations within a single protein molecule.* Phys. Rev. Lett., 2005. **94**(19): p. 198302.

75. Lu, H.P., L. Xun, and X.S. Xie, *Single-molecule enzymatic dynamics.* Science, 1998. **282**: p. 1877-1882.

76. English, B.P., et al., *Ever-fluctuating single enzyme molecules: Michaelis-Menten equation revisited.* Nat. Chem. Biol., 2006. **2**(2): p. 87-94.

77. Tyson, J.J., K.C. Chen, and B. Novak, *Sniffers, buzzers, toggles and blinkers: dynamics of regulatory and signaling pathways in the cell.* Curr. Opin. Cell Biol., 2003. **15**(2): p. 221-231.

78. Hanggi, P., P. Talkner, and M. Borkovec, *Reaction-rate theory: 50 years after Kramers.* Rev. Mod. Phys., 1990. **62**: p. 254-341.

79. Grote, R.F. and J.T. Hynes, *The stable states picture of chemical-reactions 2: Rate constants for condensed and gas-phase reaction models.* J. Chem. Phys., 1980. **73**(6): p. 2715-2732.

80. McCammon, J.A. and S.C. Harvey, *Dynamics of Proteins and Nucleic Acids*1987, New York: Cambridge Univ Press.

81. Frauenfelder, H., P.G. Wolynes, and R.H. Austin, *Biological physics.* Rev. Mod. Phys., 1999. **71**(2): p. S419-S430.

82. Zwanzig, R., *Rate-Processes with Dynamic Disorder.* Acc. Chem. Res., 1990. **23**(5): p. 148-152.

83. Austin, R.H., et al., *Dynamics of Ligand-Binding to Myoglobin.* Biochemistry, 1975. **14**(24): p. 5355-5373.

84. Xie, X.S. and H.P. Lu, *Single-molecule enzymology.* J. Biol. Chem., 1999. **274**(23): p. 15967-15970.

85. Min, W., et al., *When Does the Michaelis-Menten Equation Hold for Fluctuating Enzymes?* J. Phys. Chem. B, 2006. **110**(41): p. 20093-20097.
86. Min, W., et al., *Fluctuating enzymes: Lessons from single-molecule studies.* Acc. Chem. Res., 2005. **38**(12): p. 923-931.
87. Tyson, J.J., K. Chen, and B. Novak, *Network dynamics and cell physiology.* Nat. Rev. Mol. Cell Biol., 2001. **2**(12): p. 908-916.
88. Kholodenko, B.N., *Cell-signalling dynamics in time and space.* Nat. Rev. Mol. Cell Biol., 2006. **7**(3): p. 165-176.
89. Wylie, D.C., J. Das, and A.K. Chakraborty, *Sensitivity of T cells to antigen and antagonism emerges from differential regulation of the same molecular signaling module.* Proc. Natl. Acad. Sci. U.S.A., 2007: p. 0611482104.
90. Samoilov, M., S. Plyasunov, and A.P. Arkin, *Stochastic amplification and signaling in enzymatic futile cycles through noise-induced bistability with oscillations.* Proc. Natl. Acad. Sci. U.S.A., 2005. **102**(7): p. 2310-2315.
91. Pedraza, J.M. and A. van Oudenaarden, *Noise Propagation in Gene Networks.* Science, 2005. **307**(5717): p. 1965-1969.
92. Rosenfeld, N., et al., *Gene Regulation at the Single-Cell Level.* Science, 2005. **307**(5717): p. 1962-1965.
93. Rao, C.V., D.M. Wolf, and A.P. Arkin, *Control, exploitation and tolerance of intracellular noise.* Nature, 2002. **420**(6912): p. 231-237.
94. Swain, P.S., M.B. Elowitz, and E.D. Siggia, *Intrinsic and extrinsic contributions to stochasticity in gene expression.* Proc. Natl Acad. Sci. USA, 2002. **99**(20): p. 12795-12800.
95. Paulsson, J., O.G. Berg, and M. Ehrenberg, *Stochastic focusing: Fluctuation-enhanced sensitivity of intracellular regulation.* Proc. Natl. Acad. Sci. U.S.A., 2000. **97**(13): p. 7148-7153.

96. Levine, J., H.Y. Kueh, and L. Mirny, *Intrinsic fluctuations, robustness, and tunability in signaling cycles.* Biophys. J., 2007. **92**(12): p. 4473-4481.

97. Shibata, T. and K. Fujimoto, *Noisy signal amplification in ultrasensitive signal transduction.* Proc. Natl Acad. Sci. USA, 2005. **102**(2): p. 331-336.

98. Suel, G.M., et al., *Tunability and noise dependence in differentiation dynamics.* Science, 2007. **315**(5819): p. 1716-1719.

Chapter 2

Simulations of tubulin sheet polymers as possible structural intermediates in microtubule assembly

Zhanghan Wu[1, 2], Hong-Wei Wang[3, 4], Weihua Mu[5, 6], Zhongcan Ouyang[5, 6], Eva Nogales[3, 7], Jianhua Xing[2*]

[1] Program in Genetics, Bioinformatics and Computational Biology, Virginia Polytechnic Institute and State University, Blacksburg, VA 24061

[2] Department of Biological Sciences, Virginia Polytechnic Institute and State University, Blacksburg, VA 24061

[3] Lawrence Berkeley National Laboratory Berkeley, CA 94720

[4] Department of Molecular Biophysics and Biochemistry, Yale University, New Haven, CT 06520

[5] Institute of Theoretical Physics, The Chinese Academy of Sciences, Beijing 100080, China

[6] Center for Advanced Study, Tsinghua University, Beijing 100084, China

[7] Howard Hughes Medical Institute, Department of Molecular and Cell Biology, University of California, Berkeley, CA 94720

a. Abstract

The microtubule assembly process has been extensively studied, but the underlying molecular mechanism remains poorly understood. The structure of an artificially generated sheet polymer that alternates two types of lateral contacts and that directly converts into microtubules, has been proposed to correspond to the intermediate sheet structure observed during microtubule assembly. We have studied the self-assembly process of GMPCPP tubulins into sheet and microtubule structures using thermodynamic analysis and stochastic simulations. With the novel assumptions that tubulins can laterally interact in two different forms, and allosterically affect neighboring lateral interactions, we can explain existing experimental observations. At low temperature, the allosteric effect results in the observed sheet structure with alternating lateral interactions as the thermodynamically most stable form. At normal microtubule assembly temperature, our work indicates that a class of sheet structures resembling those observed at low temperature is transiently trapped as an intermediate during the assembly process. This work may shed light on the tubulin molecular interactions, and the role of sheet formation during microtubule assembly.

b. Introduction

Microtubules are one of the three major cytoskeleton components in eukaryotic cells [1,2]. They are hollow cylinders consisting of about 13 parallel protofilaments (PF) formed by the head-to-tail assembly of $\alpha\beta$-tubulin heterodimers. Microtubules play important roles in many eukaryotic cellular processes, including intracellular transport, cell motility, mitosis and meiosis. Microtubule dynamic instability, the phenomenon by which a microtubule switches stochastically between assembly and disassembly phases, is known to be a key property for microtubule function. The regulation of microtubule dynamics has been shown to be both of great biological significance during cell division, and of outstanding pharmaceutical value in tumor therapy. For example, Taxol©, the most widely used anticancer agent, targets tubulin and alters microtubule dynamics resulting in mitotic arrest. Therefore, studying the microtubule assembly/disassembly processes is of great relevance for both biological and pharmaceutical purposes.

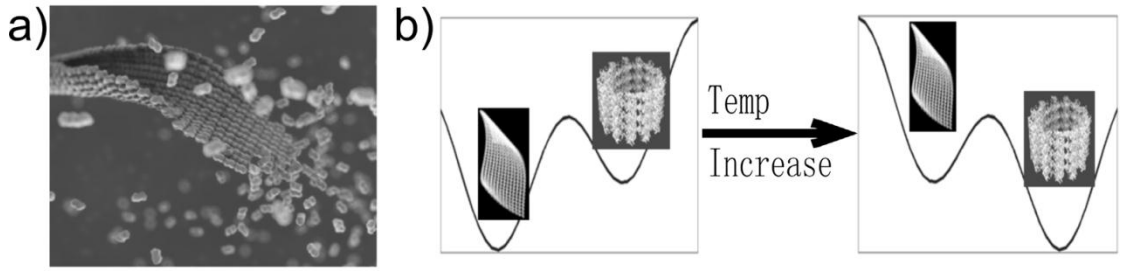

Figure 2.1. Structural model of the microtubule self-assembly pathway. (a) Simplified representation of a sheet intermediate and its conversion into a microtubule based on cryo-EM observation of sheets at the end of fast growing microtubules [7] and the structure of the low-temperature stabilized ribbons by Wang and Nogales [9]. (b) Schematic illustration of the idea that the ribbon structure is thermodynamically more stable than the microtubule structure at low

temperature (left), but less stable at the physiological temperature where microtubule assembly takes place(right). We proposed that tubulin sheet structures are kinetically trapped intermediates.

To explain the process and mechanism of microtubule assembly, various models have been proposed by both experimentalists and theorists [3,4,5,6,7]. In the most simplistic textbook model, during the microtubule assembly process $\alpha\beta$-tubulin heterodimers add one by one onto the growing end of a microtubule. Most of the existing theoretical work is based on this model [4]. However, a number of experimental observations challenge this view. In 1970s Erickson reported an intermediate sheet structure during microtubule assembly (see also Fig. 2.1a) [6]. He proposed that tubulins first form a two-dimensional open sheet, which in turn closes into tubes (see Fig. 2.1a). Several other groups observed that fast growth of existing microtubules occurs via the elongation of a gently curved sheet-like structure at the growing end both *in vitro* and *in vivo* [6,7,8]. Using cryo-electron microscopy, Wang and Nogales reconstructed the structure of a curved sheet assembly of GMPCPP-tubulin stabilized by low temperature and high concentration of magnesium [7,8,9]. The use of GMPCPP avoids the complexity due to GTP hydrolysis. This assembly could then directly convert into microtubules by raising the temperature. The authors proposed that it corresponds structurally to the sheet at growing microtubule ends observed by Chrétien and others [7,9]. In this structure tubulin molecules form slightly curved PFs, in the same head-to-tail manner as those in microtubules. However the PFs are paired, with lateral interactions within one pair being indistinguishable from those in microtubules, but with

distinct contacts between pairs [5]. Importantly, relative longitudinal displacements between neighboring PFs (“stagger”) are the same as in microtubules, indicating that no longitudinal sliding is needed during the sheet-microtubule transition, in agreement with the direct conversion from one to the other. In the remaining of the paper we call this polymer form “ribbon”, and reserve the term “sheet” for the observed structure at the end of a growing microtubule. In this work we suggest that the sheet may contain a class of tubulin structures that include the ribbon, all of which contain alternative lateral bonds different from those observed in microtubules. It is important to mention that in the literature the expression “sheet structure” has been used to refer to a protruding end of an incomplete microtubule [4], with no structural difference in the individual dimers or their interactions with respect to that in the microtubule itself, unlike the two-dimensional sheet of Chrétien and coworkers or the stable ribbon assembly of Wang and Nogales.

Wang and Nogales obtained the sheet structure by stabilizing it at low temperatures. An increase in temperature results in the direct conversion of these structures into microtubules. On decreasing the temperature a GMPCPP microtubule converts into the ribbon structure through peeling (Wang and Nogales, unpublished result; also in [10]). This observation implies that the sheet is thermodynamically more stable than the MT at low temperature, but is less stable at higher temperature (Fig. 2.1b). The conversion resembles a phase transition, which explains the observed sharp temperature dependence [11]. However, the sheet structure is short-lived in conditions under which MTs are formed, suggesting it as a kinetic intermediate [6,7].

The structural observations of Wang and Nogales raised several questions. How can a ribbon structure with alternating lateral interactions be formed during the assembly of tubulins? What is the relation between the ribbon structure and the sheet structures observed at the growing end of a microtubule at physiological conditions? What is the mechanism of the sheet-to-microtubule transition? If the sheet structure is indeed an intermediate in microtubule assembly *in vivo*, is there any biological function for it?

Due to the lack of detailed, atomic formation for the sheet, the ribbon, or the microtubule, as well as detailed kinetic studies, in this work we take an inversed problem approach. First we find out a set of minimal requirements for the system properties to reproduce the experimental observations, specifically the structures of Wang and Nogales. Then we assume that similar properties are applicable to the assembly process at physiological conditions as well, examine the consequent dynamics, and make testable predictions.

c. Methods

1. The model

We assume the $\alpha\beta$-tubulin heterodimer to be the microtubule building block, and neglect direct association/ disassociation of larger filaments, whose contributions are expected to be very small [2]. This assumption is adopted in most existing models. In this work we focus on the GMPCPP tubulins, therefore will not include GTP hydrolysis in the model. We consider three types of reactions (Fig. 2.2a &b):

1) A dimer can longitudinally add or dissociate from the ends of a PF (Fig. 2.2a, process 1). The reaction rates for plus and minus ends are different by a constant ratio δ [12,13]. This ensures that the equilibrium constants are the same for the reactions at both ends, as required by thermodynamics. For convenience in this work we call the noncovalent (longitudinal or lateral) interaction between two tubulins a “bond”.

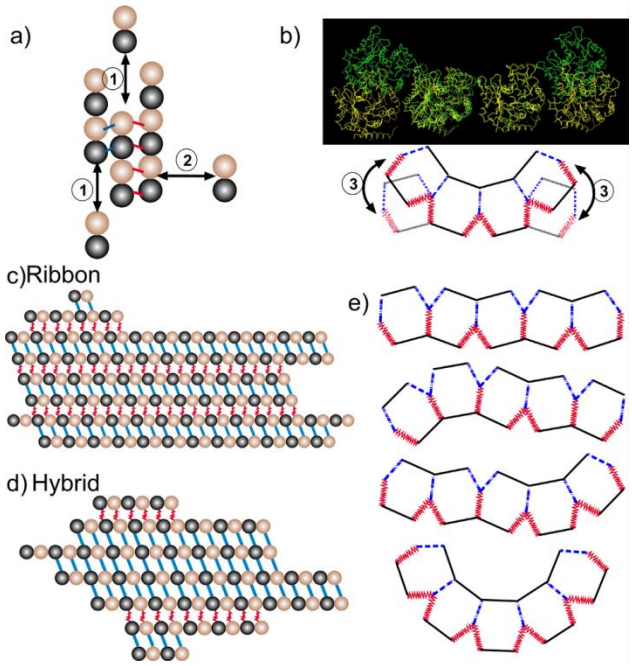

Figure 2.2. Schematic illustration of the basic concepts in the proposed model of tubulin self-assembly. (a) Three types of reactions are being modeled: longitudinal (1) and lateral (2) association/disassociation, and (b) the switch between the *tube* and sheet types of bond (3). Blue lines correspond to the *tube* bond and red lines to the sheet bond. The EM-based structures at the top of (b) show the difference between two lateral bond types [9]. (c) A typical ribbon structure with alternating lateral bonds. (d) A typical hybrid structure with the two types of lateral bonds randomly distributed. (e) An end-on view of several possible 5-PF structures.

2) A dimer can laterally associate with or dissociate from a PF from either side (Fig. 2.2a, process 2). The ribbon structure of Wang and Nogales (Fig. 2.2b) reveals that two neighboring PFs can form two types of lateral bonds [6,7,9]. We call one the *tube* bond as it closely resembles that present in closed, cylindrical microtubules. The other one we called the *sheet* bond, corresponding to that newly observed by Wang and Nogales between PF pairs.

As suggested by our cryo-EM analysis [9], the main sequence regions involved in lateral interactions between PFs in microtubules are the M-loop (Residues 274-286: PVISAEKAYHEQL in α-tubulin; PLTSRGSQQYRAL in β-tubulin) and the N-loop (Residues 52-61: FFSETGAGKH in α-tubulin; YYNEAAGNKY in β-tubulin) [14,15], whereas the lateral sheet bond interactions between two PFs involve site 1 (Residues 336-342 (H10-S9 loop): KTKRTIQ in α-tubulin; QNKNSSY in β-tubulin) and site 2 (Residues 158-164 (H4-S5 loop): SVDYGKK in α-tubulin; REEYPDR in β-tubulin) (Fig. 2.S1a). We identified these stretches of residues based on our low-resolution (18Å) cryo-EM reconstructions, and thus as a coarse approximation to the actual physical interface. Interestingly, the residues involved in the sheet bond are more conserved than those in the tube bond (see Fig. 2.S1b) [16]. It is important to mention that two types of lateral bonds are present in nature in the stable structure of the microtubule doublet, where some PFs need to interact laterally with two neighboring ones simultaneously [17]. The recent doublet structure by Sui and Downing shows a non-MT lateral interaction between PFs B10 and A5 (in their notation) [18]. The doublet and the ribbon structures show that the non-MT interactions in both structures are obtained by

rotating one PF relative to another laterally (Fig. 2.S1c). The doublet structure shows even larger rotation angle than the *sheet* bond, possibly further distorted by other binding proteins in this structure [18]. We also noticed that the various structures obtained by Burton and Himes at slightly basic pHs are easily explained by the existence of alternative types of lateral bonds, but molecular details of their structures are lacking [19]. Physically, the existence of two types of lateral bonds means that the potential of mean force between two neighboring tubulin dimers along the lateral rotational angle assumes a double-well shape. This situation is similar to the lateral interactions along the longitudinal direction, where calculations of electrostatic interactions by Sept et al. show a double-well shaped potential, corresponding to the A- and B-typed microtubules [20].

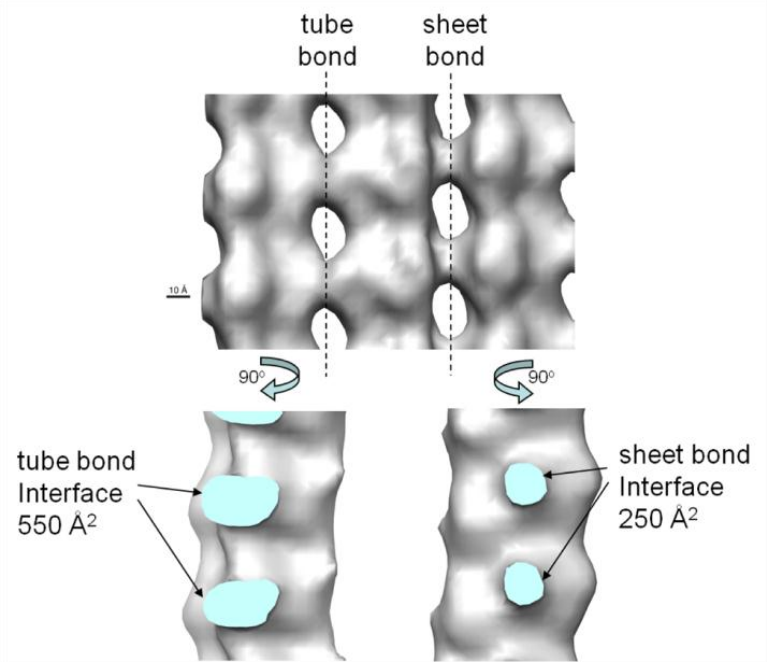

Figure 2.3. Course inspection of the electron density map of the ribbon structure. It reveals a clearly larger buried interface for the tube bond than for the sheet bond.

One additional, reasonable assumption is that the formation of the *sheet* bond is dynamically faster than that of the *tube* bond. When two protein molecules (or complexes) encounter each other to form a larger complex, it is unlikely that all the mutual interactions between the two surfaces form all at once. Mostly likely the two protein surfaces form some partial contacts, then gradually adjust to a favorable matching conformation for their mutual interaction, and during the process some residues may need to reorganize slightly. The cryo-EM reconstruction of the low-temperature stabilized ribbons revealed a larger contact surface for the tube bond than for the sheet bond (see Fig. 2.3). While a larger contact surface may lead to stronger interaction, it may be slower to form. Consequently, a *tube* bond might be slower to form than a *sheet* bond does. However, all these discussions are only suggestive, and further experimental studies are needed. As discussed later, a faster *sheet* bond formation rate is *not* a necessary assumption in our model, but it increases the percentage of transient ribbon structures, and facilitates formation of the sheet structures.

We further propose that the two types of lateral bonds can interconvert (Fig. 2.2b, process 3). Furthermore, two neighboring lateral bonds can mutually affect each other's stability and the inter-conversion rates. This assumption is necessary to reproduce the observed low temperature sheet structure. Physically, it is likely that two consecutive lateral bonds affect each other via allosteric changes in the intervening tubulin molecule. Allosteric effects on the tubulin monomers/dimers have already been proposed to play an important role during the microtubule assembly process, although details are unclear

[5,9,21]. For simplicity, in our modeling studies we assume the mutual interaction energy between two *sheet* bonds $\Delta G_{ShSh} > 0$, and other types of interactions $\Delta G_{ShTu} \sim \Delta G_{TuTu} \sim 0$, with *Sh* and *Tu* referring to the *sheet* and *tube* bond, respectively. We will discuss alternative choices later. Below we will show that with these choices one can reproduce the observed low temperature ribbon structure. For a lateral bond conversion reaction, a tubulin dimer needs to rotate about 60 degrees around the longitudinal axis of the neighboring PF [9]. In our simulations of the assembly kinetics and thermodynamic analysis, we do not consider the case in which tubulins within one PF form different types of lateral bonds with their lateral neighbors. Such defects (that tubulins within one PF form different types of lateral bonds with their neighbors) would disrupt the longitudinal and lateral interaction network within the structure, thus be energetically unfavorable, and exist only transiently. This resembles a large class of Ising-type models. For example, protein folding kinetics can often be described by two states without referring to the intermediate transition step. Consequently, our simulation assumes that the tubulin molecules within a PF would rotate collectively and cooperatively. As a consequence, the longer the PF, the harder the rotation is. Also, when a tubulin dimer adds to a PF longitudinally in our kinetic model, it engages in the same lateral bond as the rest of the precedent subunits in the same PF. This approximation greatly simplifies the simulation.

Wang et al. observed the temperature-driven ribbon-microtubule conversion using the GTP analogue GMPCPP [9,11]. Therefore GTP hydrolysis is not a requirement for ribbon/sheet conversion into a microtubule, and thus we did not

consider the GTP hydrolysis reaction in this study. We enforce the detailed balance condition by relating the rate constants to the corresponding standard free energy change (ΔG^0). For example, the on rate constant $k_{(+)}$ and off rate constant $k_{(-)}$ for a tubulin addition reaction, is given by [22]

$$\frac{k_{(+)}}{k_{(-)}} = \exp(-\frac{\Delta G^0}{k_B T}), \tag{1}$$

where k_B is Boltzmann's constant, T is the absolute temperature. Following Erickson and others [2,23,24], we divide the standard free energy ΔG^0 into two terms, an entropic energy $\Delta G_{Entropy}$ accounting for the subunit translational and rotational entropic loss due to bond formation—not the overall entropy contribution, and the remaining free energy change ΔG_i. The separation allows proper inclusion of $\Delta G_{Entropy}$ while multiple bonds form simultaneously. For instance, the longitudinal binding/dissociation reaction from the plus (upper) end in Fig. 2.2a gives

$$\Delta G^0 = \Delta G^0_{long} + \Delta G^0_{Sh} + \Delta G^0_{Tu} - 2\Delta G_{Entropy}, \tag{2}$$

where ΔG^0_{long} is standard free energy for longitudinal association, ΔG^0_{Sh} the standard free energy change of forming a *sheet* bond, ΔG^0_{Tu} the standard free energy change of forming a *tube* bond, and the term $-2\Delta G_{Entropy}$ compensates for overcounting of the entropic free energy loss. Detailed description of the rate constant and entropic term calculations can be found in the Supporting Text S1 A and B.

2. Simulation details

The assembly process was stochastically simulated with the Gillespie algorithm [25]. At each step, we recorded all the species in the system and their numbers. A reaction was randomly selected from a list of all the possible reactions of all the species in the system. We only simulated the early stage of the microtubule assembly process starting from tubulin dimers. All the simulation parameters were provided in Table 1 and figure captions. There are four energy terms in the model. In our simulations, the binding energy for the longitudinal bond ΔG_{Long} , and that of the *tube* lateral bond ΔG_{Tu} , were assigned values -19 k_BT and -15.5 k_BT, respectively, close to what used in the literature after taking into account the entropy term $\Delta G_{entropy}$ [2,20,26] (see Supporting Text S1 B). Currently there is no direct experimental information to determine the values of the other two terms, the sheet-type lateral bond energy $\Delta G_{Sh,}$ and the allosteric energy term ΔG_{ShSh}. Instead in this work we will examine how the assembly dynamics is affected by changing the values of these terms. Future experimental results may suggest possible parameter value ranges by comparing with our simulations. All the results reported here were averaged over 60 independent simulations.

In most calculations we used constant free tubulin dimer concentrations. That is, we started the simulations with tubulin dimers only and kept free tubulin dimer concentration at a fixed value throughout the simulations. Experimentally the total tubulin concentration is fixed. However, here we only examine the very early assembly stage where the percentage of tubulins forming assembly clusters is negligible, so the free tubulin concentration is approximately the same as the total tubulin concentration.

Using a constant free tubulin concentration provided us the advantage to increase the simulation efficiency with a limited computational resource. It also allowed us to examine the effect of free tubulin concentrations on the assembly process more easily. Exceptions are Fig. 2.4f, where the total number of tubulin dimers was kept constant, and the results were averaged over 2000 independent simulations. In this case we kept the system in a small size so we could run simulations for a prolonged time until the system reached equilibrium.

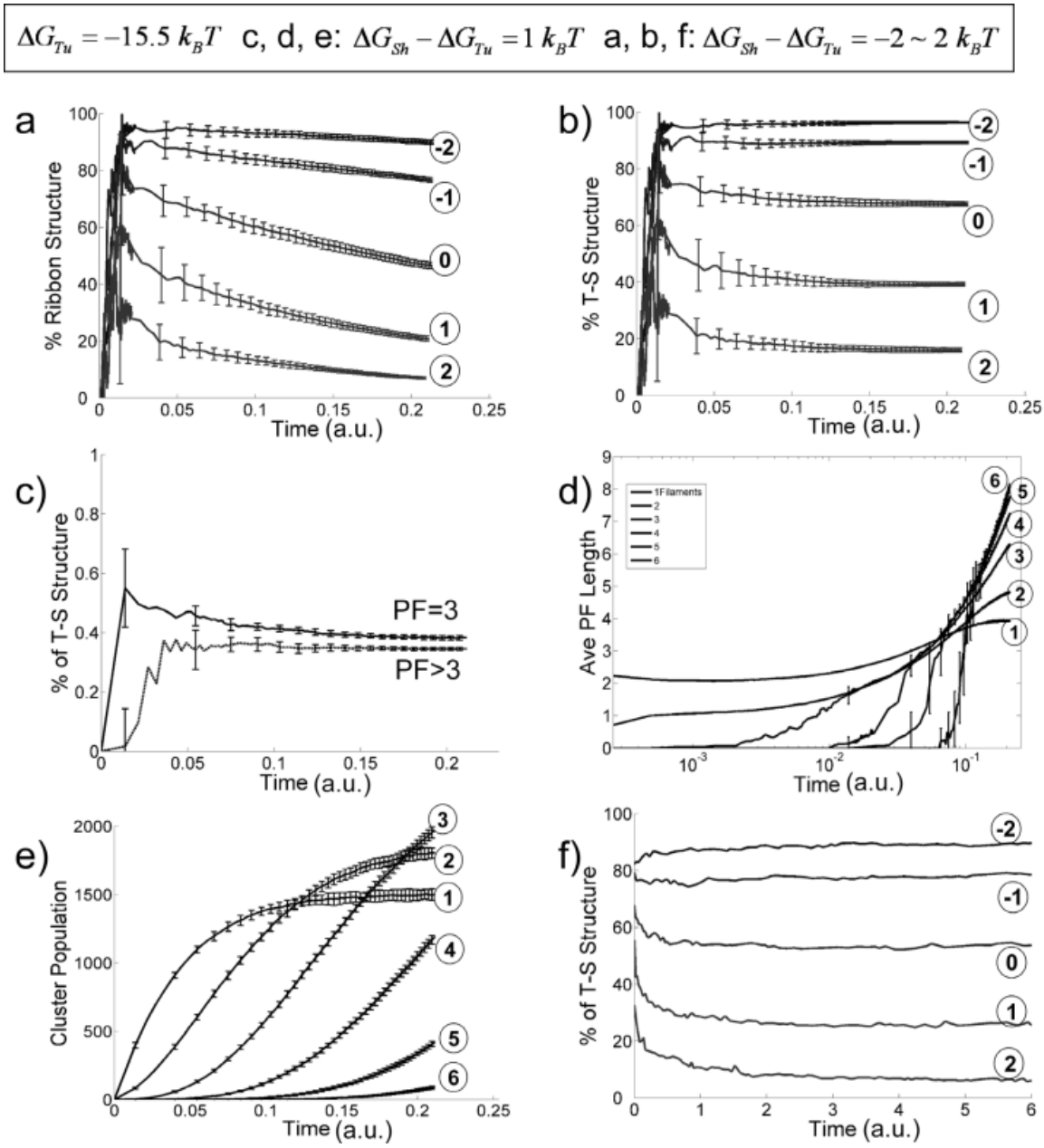

Figure 2.4. Effect of variable $\Delta G_{Sh} - \Delta G_{Tu}$ (with fixed values of $\Delta G_{Tu} = -15.5\ k_BT$ and $\Delta G_{ShSh} = 6\ k_BT$) on the assembly process. (a)-(e) plot the simulation results with constant free dimer concentration and (f) plots the results with constant total dimers. (a) Percentage of ribbon structures v.s. time for different values of $\Delta G_{Sh} - \Delta G_{Tu}$ ($-2,\ -1,\ 0,\ 1,\ 2\ k_BT$ as labeled in the figure with corresponding circled numbers). (b) Probability of finding neighboring *tube-sheet* (T-

S) structures as a function of time ($\Delta G_{Sh} - \Delta G_{Tu} = -2,\ -1,\ 0,\ 1,\ 2\ k_B T$ as labeled in the figure with circled number). (c) Percentage of T-S structures v.s. time for structures with 3 PFs (solid line) and structures with 4 or more PFs (dashed line). (d) Average PF lengths of assembly structures v.s. time with number of PF =1, 2, 3, 4, 5, and 6, respectively (for $\Delta G_{Sh} - \Delta G_{Tu} = 1\ k_B T$). (e) Occurrence of different size clusters v.s. time with numbers of PF = 1, 2, 3, 4, 5 and 6, respectively ($\Delta G_{Sh} - \Delta G_{Tu} = 1\ k_B T$ for all). (f) Percentage of T-S structures v.s. time for variable $\Delta G_{Sh} - \Delta G_{Tu}$ $(-2,\ -1,\ 0,\ 1,\ 2\ k_B T$, as labeled in the figure with corresponding circled numbers) with a constant number of total tubulin dimers of 100.

At each sampling step, we took a snapshot of the tubulin assembly clusters. Different clusters have different shape, length and width. To characterize the structural properties of each cluster, we examined the following joint probabilities (or percentages): 1) P(Tu-Tu)-- both of the two neighboring lateral bonds lying between three neighboring PFs being *tube* type; 2) P(Tu-Sh)—one tube type, and one sheet type; 3) P(Sh-Sh)-- both being *sheet* type, with P(Tu-Tu) + P(Tu-Sh) + P(Sh-Sh) = 1. We call the local structure formed by three tubulin dimers in lateral contact as a Tu-Tu, Tu-Sh, or Sh-Sh 3-mer structure. The percentage of Tu-Sh structures in the system is calculated as the ratio between the total number of Tu-Sh structures and the total number of 3-dimer structures in all clusters with three or more PFs. A cluster is defined as a ribbon cluster only if P(Tu-Sh) = 1 (Fig. 2.2c). Therefore a higher value of P(Tu-Sh) means that the cluster is closer to a ribbon structure. A ribbon cluster must have 3 or more PFs by definition. The percentage of ribbon structures in the system is calculated as the ratio

between the total number of Tu-Sh structures in the ribbon clusters and the total number of 3-dimer structures in all clusters with three or more PFs. To calculate the population of clusters with certain number (*N*) of PFs, we simply count the total numbers of those *N*-PF clusters at certain steps. The average PF length of an *N*-PF cluster is calculated as the total number of dimers in the cluster divided by *N*.

Currently there is no quantitative experimental data available on the assembly rates at the initial stage we studied here. Therefore all the results are reported with a relative time unit, which can be easily scaled to the experimental rates once available.

d. Results

1. Effect on tubulin assembly of a difference in binding energy between *sheet*- and *tube*- lateral bonds

Fig. 2.4 gives the dependence of the assembly process on the value of the $\Delta G_{Sh} - \Delta G_{Tu}$ (binding energy difference between the *sheet*- and *tube*-type lateral bonds), with fixed values of $\Delta G_{Tu} = -15.5\ k_BT$ and $\Delta G_{Sh} = 6\ k_BT$. The percentage of Sh-Sh structures is negligible for all simulations (data not shown). The percentage of ribbon structures and that of Tu-Sh structure decreases on increasing ΔG_{Sh} (see Fig. 2.4a & b). For $\Delta G_{Sh} - \Delta G_{Tu} < 0$ (the *sheet* bond stronger than the *tube* bond, simulating the low-temperature condition) the percentage of ribbon structures stays at a high plateau (top curves in Fig. 2.4a). For $\Delta G_{Sh} - \Delta G_{Tu} > 0$ (the *tube* bond is stronger than the *sheet* bond, simulating the high-temperature condition) the percentage of ribbon structures starts with a relative high value, then decreases with time. This observation indicates that initially formed

sheet bonds transform into *tube* bonds at a later time. Fig. 2.4c supports this idea by showing that (for $\Delta G_{Sh} - \Delta G_{Tu} = 1\ k_B T$) the percentage of Tu-Sh structures in 3-PF clusters is higher than that of later formed larger clusters. Fig. 2.4d gives (also for $\Delta G_{Sh} - \Delta G_{Tu} = 1\ k_B T$) the average PF lengths (as number of dimers) for different cluster sizes. Small clusters with one or two PFs quickly reach steady-state with average longitudinal length of about 4 tubulin dimers. Experimentally, a large amount of small single- and double-PF clusters with length 4-5 tubulin dimers are observed at the initial stage of the assembly process [11]. The longitudinal length of larger clusters increases continuously within the simulation time. From a thermodynamic point of view the explanation for this result is that the lateral bonds within larger clusters stabilize the clusters, but the single and double-PF clusters lack sufficient lateral bonds and cannot grow long [2]. We performed a simulation with the lateral bond addition turned off so only one PF structures can be formed. The observed average single PF structure length quickly reaches a plateau at a slightly larger value (about 10 dimers, data not shown). From a kinetic point of view, the smaller clusters may disappear also by growing in width and thus transforming into larger clusters before growing long. Similarly shown in Fig. 2.4e, the populations of single- and double-PF clusters reach a plateau, while the numbers of larger clusters increase continuously within the time of simulation.

In Fig. 2.4b we examined how the percentage of Tu-Sh structures evolves with time. The results show that all the curves reach a plateau. It is unclear whether the system reaches equilibrium or a dynamic steady-state. The latter would mean that newly formed *sheet* bonds compensate the loss of the Tu -Sh structure population due

to Sh→Tu conversion, so the percentage of Tu -Sh structures remains unchanged. If this is the case, the apparent percentage of Sh → Tu conversion should be less than the real value. Therefore, we performed additional simulations with constant total number of tubulin dimers. This time, we used a smaller size system (100 dimers), which allowed us to perform sufficiently long simulations for the system to reach true thermodynamic equilibrium. Fig. 2.4f shows the evolution of the percentage of Tu-Sh structures with different values of $\Delta G_{Sh} - \Delta G_{Tu}$. In the case of $\Delta G_{Sh} - \Delta G_{Tu} > 0$, thus when the *tube* bond is thermodynamically more stable, the Tu-Sh structures start at relatively high percentage, then convert after the first few thousand steps. This result is due to the faster formation of *sheet* bonds versus *tube* bonds, with the former being transiently trapped as the PFs grow longer. The *sheet* bonds eventually convert to the thermodynamically more stable *tube* bonds and the system reaches equilibrium. Compared to Fig. 2.4b, we did observe larger percentage of Sh → Tu transition in Fig. 2.4f, indicating that the curve plateaus in Fig. 2.4b are due to a dynamic steady-state. In the case of $\Delta G_{Sh} - \Delta G_{Tu} < 0$, where a *sheet* bond is more stable than a *tube* bond, in addition to the effect of the positive ΔG_{SS}, the Tu -Sh structures are more stable thermodynamically (the top lines of Fig. 2.4f).

2. Effect on tubulin assembly of mutual allosteric interaction between two adjacent *sheet* bonds

If formation of a new lateral bond is not affected by the existing PFs ($\Delta G_{ShSh} = 0$), one would expect randomly distributed lateral bond types between PFs. The allosteric term ΔG_{ShSh} is necessary for reproducing the dominating ribbon structures

experimentally observed at low temperature ($\Delta G_{Sh} - \Delta G_{Tu} < 0$). Fig. 2.5 shows that, for $\Delta G_{Sh} - \Delta G_{Tu} = -1.5\ k_B T$, the percentage of ribbon structures and that of T-S structures is sensitive to the value of ΔG_{ShSh}. As ΔG_{ShSh} increases from 0 to 6 $k_B T$, the percentage of ribbon structure increases from 20% to around 90% (Fig. 2.5a). The percentage

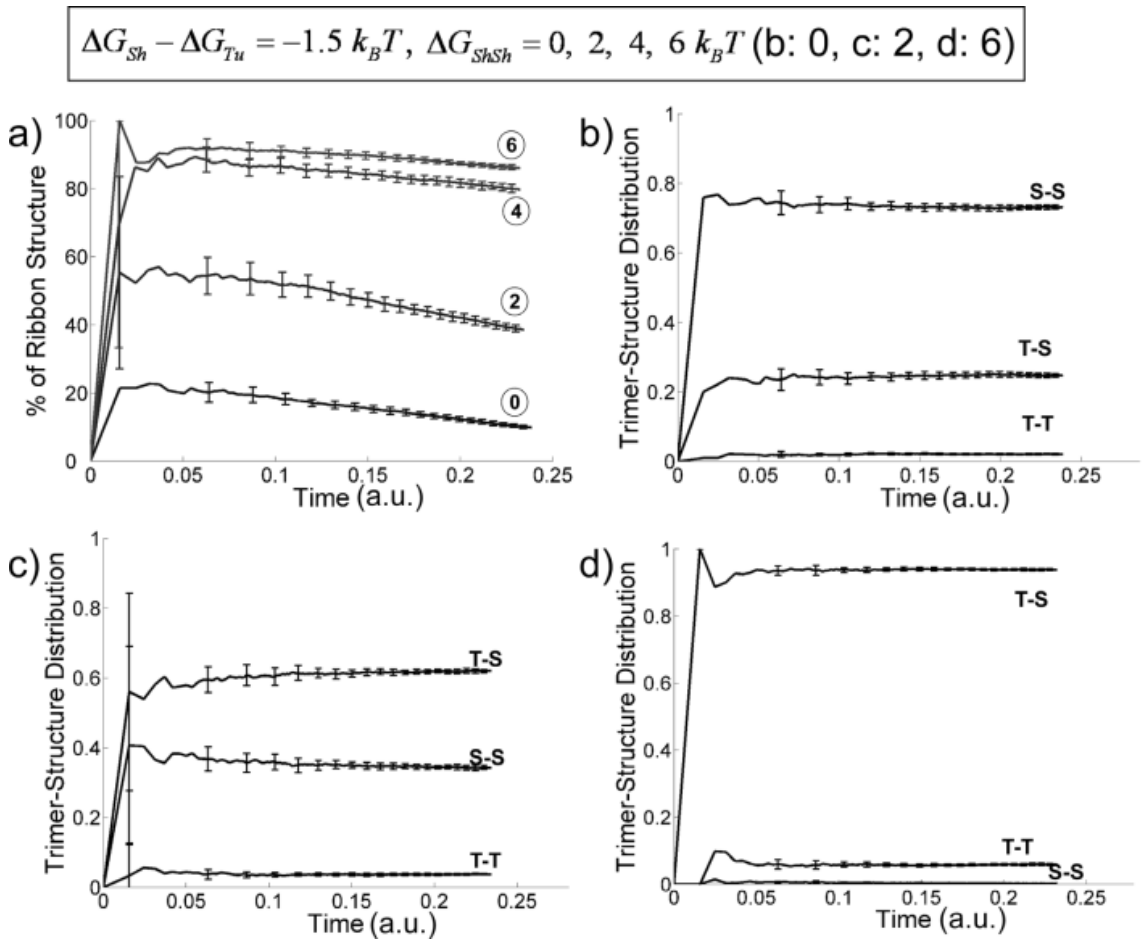

Figure 2.5. Effect of variable ΔG_{ShSh} on the assembly structures for fixed $\Delta G_{Sh} = -17\ k_B T$ and $\Delta G_{Tu} = -15.5\ k_B T$ ($\Delta G_{Sh} - \Delta G_{Tu} = -1.5\ k_B T < 0$). (a) Percentage of ribbon structures as a function of time (ΔG_{ShSh} = 0, 2, 4 and 6 as indicated by circled numbers). (b) Trimer-structure distribution v.s. simulation step for $\Delta G_{ShSh} = 0$. The three possible trimer structures, T-T (*tube-*

tube), T-S (*tube*-sheet) and S-S (sheet-sheet), are indicated in the figure. (c) Trimer structure distribution v.s. simulation step with $\Delta G_{ShSh} = 2\ k_B T$. (d) Trimer-structure distribution v.s. simulation step with $\Delta G_{ShSh} = 6\ k_B T$.

drops slightly as time evolves. This is because some newly formed small ribbon structures grows to hybrid forms upon adding more PFs. Fig. 2.5b-d show the 3-mer structure distribution. For $\Delta G_{ShSh} = 0$, Fig. 2.5b shows that the S-S structure is dominating, reflecting the fact that the *sheet* bond is stronger than the *tube* bond. While there are still about 20% Tu-Sh structures, the Tu-Tu structures are negligible. On increasing ΔG_{ShSh} to 2 $k_B T$ (Fig. 2.5c), the free energy difference between a *sheet* and a *tube* bond (-1.5 $k_B T$) cannot compensate the unfavorable term ΔG_{ShSh}, and more Tu-Sh structures than the Sh-Sh structures are formed. As we further increase ΔG_{ShSh} to $6\ k_B T$ (Fig. 2.5d), T-S structures become dominating, while the other two structures are negligible. In the case where $\Delta G_{Sh} - \Delta G_{Tu} > 0$, a positive value of ΔG_{ShSh} maintains its effect on producing higher percentage of newly formed Tu-Sh arrangement, with the ribbon structures dominating the population, but these gradually transform into the more stable microtubule structures (see Fig. 2.S2).

3. The effect of free tubulin concentration on the assembly process

The free tubulin concentration is another factor affecting the assembly kinetics. Fig. 2.6a and b examine the effect of free tubulin concentration on the assembly process in the case where $\Delta G_{Sh} - \Delta G_{Tu} > 0$ (high temperature scenario in which tubulin

polymerizes into microtubules). On increasing the free tubulin dimer concentration from 5, to 25, to 125 μM, both the ribbon and T-S structures increase. At higher dimer concentration the population of the ribbon structure forms starts at a high percentage, then drops quickly to the similar level as that at lower dimer concentrations. A possible explanation for this phenomenon is that some of the ribbon structures transform into larger hybrid structures upon PF addition. This is supported by the persistence of the high percentage of Tu-Sh structures at high tubulin concentration (Fig. 2.6b). The steady-state average length of

$$\Delta G_{Sh} - \Delta G_{Tu} = 1.5\ k_B T \qquad c = 5,\ 25,\ 125\ \mu M$$

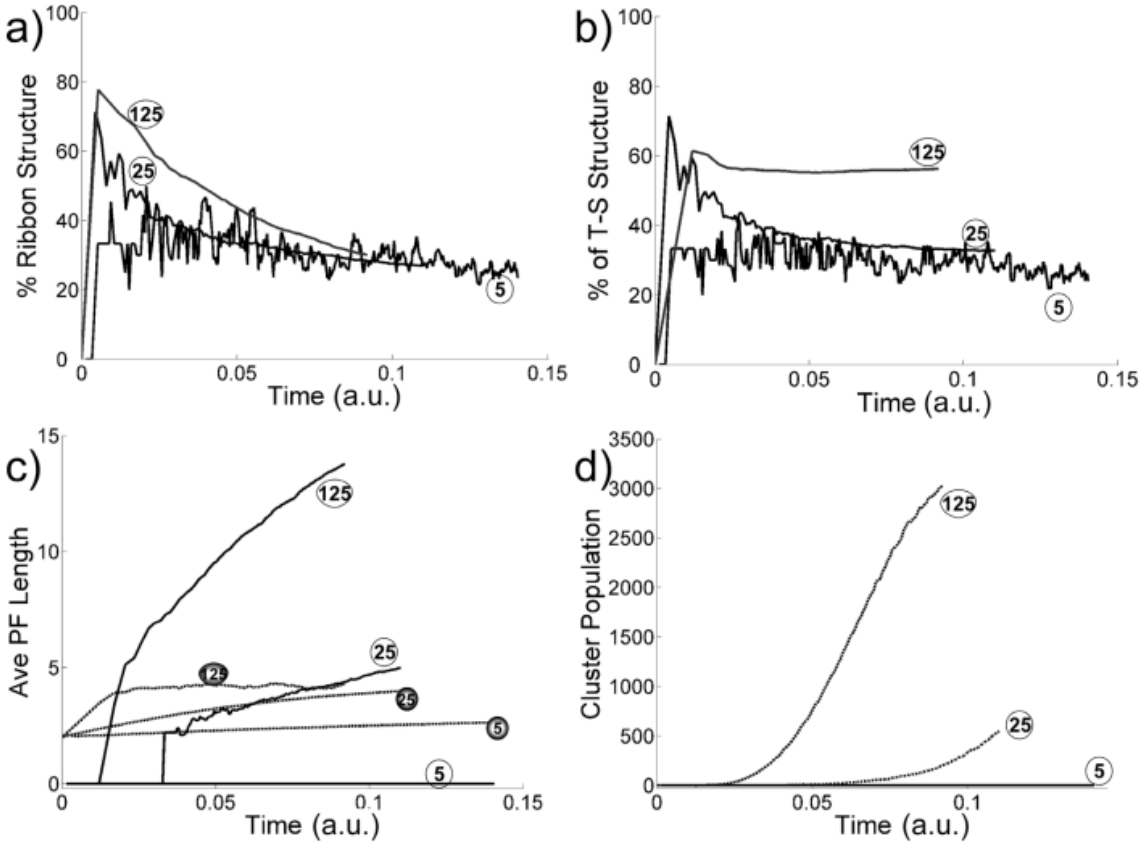

Figure 2.6. Effects of tubulin dimer concentrations on the assembly process (for $\Delta G_{SS} = 6\ k_B T$, $\Delta G_{Sh} = -14\ k_B T$, $\Delta G_{Tu} = -15.5\ k_B T$, i.e., $\Delta G_{Sh} - \Delta G_{Tu} = 1.5\ k_B T$) (dimer concentration c = 125, 25, 5 μM, as labeled in the figure with corresponding circled numbers). (a) Percentage of ribbon structures as a function of time. (b) Probability of finding neighboring T-S structures as a function of time. (c) Average PF lengths of structures with 1 PF (dashed lines with grey circled numbers indicating concentrations) and 5 PFs (solid lines with open circled numbers indicating concentrations) v.s. time. (d) Occurrence of clusters with 5 PFs v.s. time for different tubulin concentration as labeled.

the single-PF clusters increases as the tubulin concentration goes up (Fig. 2.6c, curves marked with grey circles), reflecting the fact that increasing the tubulin concentration favors bond formation both thermodynamically and kinetically. The lateral bond formation is apparently favored by high dimer concentrations due to a higher assembly rate, so the multi-PF clusters grow even faster at higher dimer concentration (Fig. 2.6c, curves marked with open circles). The population of larger clusters (5-PF in the case shown) also increases faster at higher dimer concentrations (Fig. 2.6d). Overall, our simulations suggest that the sheet intermediates are more likely to be observed at high free tubulin concentrations. This agrees well with the experimental result that larger and more abundant sheet structures are observed during the initial, exponential phase of tubulin of polymerization when free tubulin concentrations are high (>100 μM) [7,27]. Physically, increasing the free dimer concentration increases the cluster growth rates, which effectively allows less time for the internal Sh→Tu transition, and thus increases the percentage of ribbon and Tu-Sh structure, as shown in Fig. 2.6a & b.

e. Discussion

Erickson and Pantaloni performed thermodynamic analysis on the initial stages of polymer assembly [24], with the assumption that only one type of lateral bond exists. In their model, the sheet is not structurally different from the microtubule structure. In the present study, and while incorporating recent structural information, we are trying to simulate the very early stages of tubulin polymerization at both low and high (physiological) temperature, making a minimal number of assumptions that will reproduce existing experimental observations. The main conclusions from this exercise follow.

Thermodynamic analysis: Let's consider a structure with 2*m* PFs of length *n dimers*. At low temperatures (less than 15 ˚C), the *sheet* bond is more stable than the *tube* bond ($\Delta G_{Sh} - \Delta G_{Tu} < 0$). Therefore, the thermodynamically most stable structure tends to form as many *sheet* bonds as possible. However, the term ΔG_{ShSh} disfavors a sheet structure with all *sheet* bonds. One can show that, instead, the most stable structure is the one with alternating lateral bonds, provided $\Delta G_{ShSh} > \left|\Delta G_{Sh} - \Delta G_{Tu}\right|$. The free energy difference between the structure with neighboring *sheet* bonds and the one with alternating lateral bonds is $n(2m-1)(\Delta G_{ShSh} - \Delta G_{Tu} + \Delta G_{Sh})$. The difference between a *sheet* bond-only structure and an unclosed *tube* bond-only structure is $n(2m-1)(\Delta G_{Sh} - \Delta G_{Tu})$. When *n* and/or *m* are large, a small difference in the bond energy leads to a large difference in the Boltzmann weight. The structure with alternating lateral bonds is thus the dominating form. Above a certain temperature, the *tube* bond becomes more stable

than the *sheet* bond ($\Delta G_{Sh} - \Delta G_{Tu} > 0$), and the microtubule becomes the most stable polymer form. These thermodynamic considerations explain the results in Fig. 2.4 and Fig. 2.5. There are several possible origins on the temperature dependence of $\Delta G_{Sh} - \Delta G_{Tu}$. We discussed them in Supporting Text S1 C.

For the allosteric effect represented by the term ΔG_{ShSh}, we suggest two possible mechanisms. First lateral interactions have been proposed to straighten a tubulin dimer (this is referred to as the lattice effect) [9,28,29]. Consequently, the lateral interaction surface is in general coupled to straightening, and the allosteric effect proposed here and the lattice effect are closely related and coupled. This effect may exist even if each tubulin monomer is treated as a rigid body. While this is the mechanism we favor, a second alternative scenario is that, as tubulin molecules are flexible, lateral interactions on one side could affect the lateral surface on the other side of the protein.

A sheet structure is a common morphology for biological molecule self-assembly [30,31,32]. Tubulin assembly shares some common features. For example, the ribbon structures are helical, and the tubulins are arranged in a microtubule in a helical manner [9]. Therefore, due to asymmetric off-axis interactions between tubulins these structures are chiral [32]. The general theory discussed by Aggeli et al. may be applied to a more detailed analysis of the tubulin assembly model.

How is the *sheet* bond kinetically trapped during the assembly process? At physiological temperatures, where $\Delta G_{Sh} - \Delta G_{Tu} > 0$, the microtubule is thermodynamically at the most stable polymer form. However, Fig. 2.5 shows that a

large population of structures with the *sheet* bonds can still be observed transiently at the initial assembly stage. The steady state population of ribbons will depend on the actual value of $\Delta G_{Sh} - \Delta G_{Tu}$. Fig. 2.7a schematically illustrates some possible reaction pathways that would lead to a kinetic trap (Fig. 2.7b). During the early stages of microtubule assembly (which we modeled here), short clusters of a few PFs are assembled. When a dimer adds on to a cluster laterally, it forms a *sheet* bond with a higher probability (1→2) than a *tube* bond (1→3). Thermodynamically the *sheet* bond has the tendency to convert into a *tube* bond, since the *tube* bond has lower free energy (2→3, Fig. 2.7b, left panel). However, before the slow lateral bond type conversion takes place, another dimer may add on longitudinally at the end of a PF with a higher rate (2→4). Lengthening of the PF further increases the difficulty of lateral bond conversion by increasing the conversion barrier height (4→5, Fig. 2.7b, right panel). Consequently, the lateral *sheet* bonds are transiently trapped.

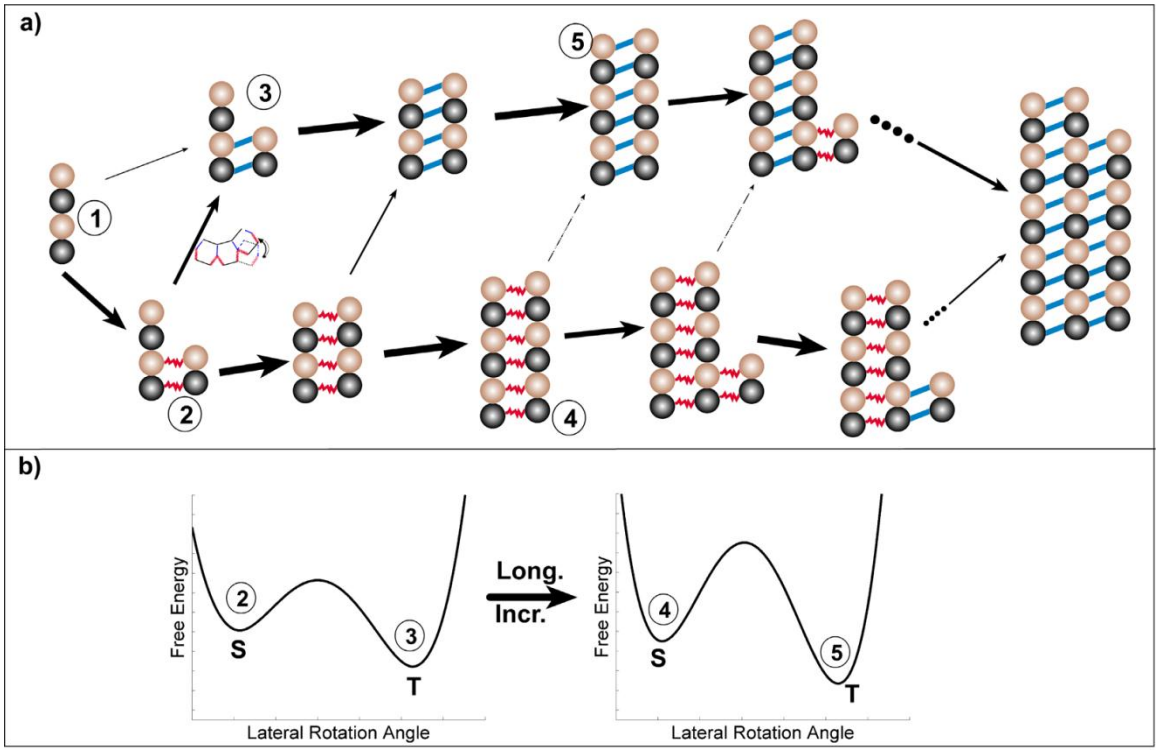

Figure 2.7. Schematic illustration of how two PFs could form sheet bonds fast and then be kinetically trapped. (a) Illustrative pathways of the assembly process showing a kinetic trap. (b) Schematic illustration that formation of additional sheet bonds increases the transition barrier to the thermodynamically more stable *tube* bonds.

The main idea in our proposed mechanism is that there are three major classes of competing processes with different characteristic time scales: longitudinal elongation, lateral association to form a *tube*- or *sheet*- type bond, and Sh→Tu conversion. Only the first two processes depend on the tubulin concentrations. As long as the first two processes (especially longitudinal elongation) are much faster than the conversion rate, kinetically trapped structures containing the *sheet* bonds are observable. In our simulations we used a lateral association rate for the *sheet* bond larger than that for the

tube bond. From a structural point of view, the GTP-tubulin in solution might have a conformation favoring the formation of lateral *sheet* bond over that of the *tube* bond. The oligomerized tubulin may undergo an induced-fit conformational change during the conversion from the *sheet* bond to the *tube* bond, forming more stable lateral interactions. Keeping all other parameters unchanged (e.g., ΔG_{ShSh}) but using the same value of the lateral association rates for the two lateral bond types, our simulations (data not shown) show that the ribbon and other hybrid structures are still observed, but constitute a smaller fraction of the total population. It is important to emphasize that our conclusions are quite insensitive to the model parameters used in this work.

Our model also predicts the existence of some hybrid structures between the sheet and the MT forms, where the lateral bond pattern is not so regular (e.g, some of the structures in Fig. 2.2d and 2e). The cryo-EM images of Chretien et al. revealed a distribution of the sheet bending angles [7] , which may correspond to different sheet structures with different ratios of *sheet* versus *tube* bonds. It is tempting to speculate that at the tip of the growing structure Sh-Tu alternating bonds predominate (see Fig. 2.4), but as the structure gets closer to the growing microtubule, more and more *sheet* bonds have converted to *tube* bonds, until eventually all lateral contacts are *tube* contacts (an alternative explanation is that at any given point along the length of the sheet, all lateral bonds are the same, but that they change in synchrony along the length, asymptotically reaching that of the *tube* bond when the structure finally closes into a tube). The process of conversion was not covered in the present study, where we focused on the very early stage of the assembly process. In this case the formed structures all have small sizes and therefore the conversion process itself is very fast.

Instead, it is the initiation of the conversion that is rate-limiting. To mathematically model the conversion process and the sheet curvatures explicitly at the growing tip of a preformed microtubule, one needs to include more details of the mechano-chemical properties of the system. This is an ongoing effort in our labs.

In our model we choose $\Delta G_{ShTu} \sim \Delta G_{TuTu} \sim 0$, and $\Delta G_{ShSh} > 0$. These are roughly based on steric constraints imposed by the competing strains of two distinct curvatures-- the longitudinal curvature along the length of a protofilament, and the curvature of the lateral interactions that give rise to a close structure for the microtubule. Our model also assumes that the value of $\Delta G_{Sh} - \Delta G_{Tu}$ vary with temperature (Fig. 2.S3a). It is important to point out that this scheme (Scheme 1) is not the only one that can reproduce the observed low and high temperature structures (ribbons and microtubules, respectively, at steady state). For example, an alternative scheme (Scheme 2) could be that $\Delta G_{Sh} - \Delta G_{Tu} > 0$ (so the *tube* bond is always stronger than the *sheet* bond), $\Delta G_{ShTu} \sim \Delta G_{ShSh} \sim 0$ (which are unnecessary but for simplicity), but $\Delta G_{TuTu} > 0$, which decreases with temperature (Fig. 2.S3b). Also see Supporting Text S1 C, which provides some theoretical analysis with a reaction path Hamiltonian [33] on a possible origin for a hypothetical temperature dependence of ΔG_{TuTu}. Our stochastic simulations confirm that this scheme can reproduce the low temperature ribbon structures and the high temperature transient sheet structures (see Fig. 2.S4 and Supporting Text S1 C for details). Compared to Scheme 1, which is the focus of this work, and where the Sh-Sh structure is negligible (with $\Delta G_{ShSh} > 0$), Scheme 2 suggests that a larger percentage of

Sh-Sh structures should be observable if one chooses $\Delta G_{ShSh} \sim 0$. A specific way to distinguish the two schemes would be to examine the population difference of 2-PF clusters with *sheet* bond and *tube* bond. Fig. 2.S5 shows that, in Scheme 1, the *sheet*-type 2-PF clusters are dominant at low temperature and the *tube*-type 2-PF clusters become more at high temperature; in Scheme 2, the *tube*-type 2-PF clusters are always dominant at both high and low temperature. Experimentally determining the 2-PF cluster structures at both low and high temperatures would allow us to estimate the value of ΔG_{ShSh}. This will also help on evaluating the two schemes discussed here and the proposal by Chrétien as well. However, no matter which scheme is correct, our main conclusion remains: the existence of the sheet tubulin structures is due to thermodynamics at low temperatures, but kinetics at higher (physiological) temperatures.

Fygenson et al. carried out variability-based alignment of α- and β- tubulin sequences [16]. More conserved residues usually have functional importance. In Fig. 2.S1 we reproduced their result, and indicated the above-mentioned residues involved in lateral interactions. It is clear that those residues (especially several charged ones) involved in the *sheet* bond formation are generally more conserved than those for the *tube* bond. In addition, there are a smaller number of residues involved in the interface of the former, which can be visualized in a simple fashion by examination of the ribbon electron density map showing a smaller contact surface for the *sheet* bond than for the *tube* bond (see Fig. 2.3). These observations may explain why the *sheet* bond would be faster to form than the *tube* bond. The former involves less residues but strong electrostatic interactions, which can guide the approaching tubulins to interact. On the

other hand, to form a *tube* bond more residues need to align (and reorganize) properly with each other, which may result in a high barrier for the reaction. Is it possible that tubulin evolved a *sheet*→ *tube*, two-step processes to increase the tubulin lateral assembly rate: a free tubulin dimer would first be captured by the fast-forming *sheet* bond, and this would serve as a primer to guide the complex to form the more stable but slower-to-form *tube* bond. In a direct *tube*-bond formation mechanism, the interaction between the loosely formed contact pairs may be too weak to hold the newly added tubulin dimer for sufficiently long time before necessary conformational reorganization takes place to form the stable *tube* bond, which would result in very low lateral association rate.

How biologically relevant is the proposed *sheet* bond? The ribbon structure obtained by Wang and Nogales shows two types of lateral bonds. In our model, we assume that the same types of lateral bonds exist during the assembly process of both GMPCPP and GTP tubulins at physiological conditions. One may argue that the observed ribbon structure is not physiological, as it is obtained at low temperature and high magnesium ion concentrations. High magnesium ions are typically used for the stabilization of all forms of tubulin assembly, and are hypothesized to shield the acidic C-terminal tails of tubulin (E-hooks), perhaps in a manner similar to that proposed for classical MAPS. These MAPs are highly basic, poorly structured, and generally have also a stabilizing effect on different tubulin assembly forms (e.g. they stabilized both microtubules, and tubulin rings). Cold temperature, on the other hand, is known to have a destabilizing effect on microtubules (interestingly, the addition of certain +TIPS –proteins that in the cell bind to the growing end of microtubules– to microtubules in vitro renders the

polymers cold-stable, just like the anticancer drug taxol does (K. Patel, R. Heald, and E. Nogales, unpublished results). The formation of the ribbon structure, in the presence of GMPCCP, at low temperatures, was therefore a surprise. A working hypothesis to explain the assembly of the ribbons, in conditions where GTP tubulin would not be able to assemble into microtubules, is that temperature slows down tubulin interactions, with less of an effect on the rate of hydrolysis once a tubulin-tubulin contact has formed. Thus, under low temperature conditions little assembly occurs, and when it does hydrolysis quickly follows, before tubulin has a chance to make a microtubule closure and store the energy as lattice strain. When the hydrolysis step is eliminated, the slow polymerization of GTP tubulin (GMPCPP) can continue without the conformational change, and the destabilization effect that hydrolysis brings on tubulin. Under this simple assumption, we propose that the ribbon assembly conditions shed information on the process of microtubule assembly taking place before microtubule closure. This idea is supported by the structure of the ribbon itself, which shows alternating lateral contacts between protofilaments, that otherwise preserve the precise stagger between protofilaments seen in the microtubule. This suggests that the ribbons would be able to convert directly into microtubules, as it was experimentally confirmed [9]. Concerning the rotation of the lateral *sheet* bond, it is important to mention that this type of arrangement, or at least one involving alternative lateral contacts without longitudinal displacements between protofilaments, could have been deduced directly from the extended sheets observed by Chretien and colleagues growing at the end of microtubules, unless extreme deformability is otherwise hypothesize for the tubulin subunit, which is beyond reason.

An alternative model for the experimentally observed sheet structures at the end of growning microtubules is that they involved tubulin interactions are not different from those observed in a MT. A sheet structure is simply an incomplete protruding MT structure. However, the stochastic modeling results of VanBuren show that with this model it is very unlikely to form long incomplete structures at a MT growing end. The structures are energetically unfavorable, and are precursors for disassembly rather than assembly [4]. They didn't examine dependence of the sheet length on the tubulin concentrations. One would expect weak or inverse dependence, since low tubulin concentrations would favor disassembly. This is contrary to the observation that the sheet structures are observed under growth conditions, and become longer (up to several hundred nanometers) upon increasing tubulin concentrations [7].

In conclusion, although there is yet no direct evidence of the presence of the sheet-type lateral bond described here under physiological conditions (the transient character preventing structural characterization, but see discussions on the doublet below), there is very compelling evidence that alternative lateral interactions do exist in a transient intermediate, the sheets at the end of fast growing microtubules. All our analyses indicate that the ribbon structure is the best candidate in existence to describe such intermediates. A somehow similar, and stable structure has been observed in the doublet form, which demonstrates that the alternative lateral bonds do exist *in vivo*. As discussed below, the unusual high conservation of the residues proposed to participate the *sheet* bond formation strongly suggest the functional importance of these residues. We put forward the proposal that existence of (at least) two types of lateral bond

naturally explains the sheet and microtubule forms observed *in vitro*, and the interconversion between them.

The situation *in vivo* is more complex, where various microtubule-associated-proteins (MAPs) may modify the microtubule assembly/disassembly process. While more *in vivo* studies are necessary to address the functional relevance of the sheet structure observed *in vitro*, it will also be very informative to study the microtubule assembly process in the presence of purified microtubule-binding proteins. It is important to notice that all structural studies of microtubules with binding partners have been carried out by adding the partners to preassembled (usually taxol-stabilized) microtubules. The effect on the assembly process of +TIPs, for example, should come a lot closer to reproduce what goes on inside the cells, than the analyses carried out to date with purified tubulin alone.

We also suggest that the existence of alternative lateral bond types may have functional importance. Nogales and Wang proposed that the ribbon structure (and the sheet structure in general) could provide a novel surface for microtubule-binding proteins that could recognize surfaces unique to the *sheet* bond to track microtubule growing ends [5]. It has also been proposed that the sheet structure could constitute a structural cap at the end of growing microtubules [7] of essential importance in dynamic instability (notice that both functions would most likely be linked). Additionally, if the MT lateral bond is indeed stronger than the *sheet* lateral bonds, free energy would be stored in the lateral bonds of the sheet structure, released upon closure, which could

result in mechanical force generation. We provided a more detailed discussion of this idea in the Supporting Text S1.

The nature of lateral interactions also affects the microtubule mechanical properties. Even if only one type of tubulin lateral interactions exists under normal conditions, microtubules in a cell are constantly under mechanical stress due to protein motors and other microtubule associated proteins [34]. There is a certain probability that some of the lateral bonds within a microtubule may convert to another type of interactions under extreme conditions (e.g. buckling under large mechanical force), as implied by recent atomic force microscope studies [35,36]. The new type of lateral bond provides a way of releasing local mechanical stress without breaking the MT. We expect that the mechanical property of a MT with and without this new type of lateral interaction would be dramatically different, and can be tested experimentally. It remains to be examined if these conditions are biologically relevant.

What could be the function of the sheet intermediate? In addition to the artificially generated ribbon structure of Wang and Nogales, cryo-EM studies have more directly shown the presence of sheet intermediates during microtubule growth, both *in vitro [6,7] and in vivo* [8]. Theoretically, the *sheet* structures and the conversion into microtubules could play several important functional roles. Nogales and Wang proposed that the ribbon structure (and the sheet structure in general) could provide a novel surface for microtubule-binding proteins that could recognize surfaces unique to the *sheet* bond to track microtubule growing ends [5]. It has also been proposed that the sheet structure

could constitute a structural cap at the end of growing microtubules [7] of essential importance in dynamic instability (notice that both functions would most likely be linked) .

The *sheet* bond involves fewer residues but strong electrostatic interactions, which can guide the approaching tubulins to interact. On the other hand, to form a *tube* bond more residues need to align (and reorganize) properly with each other, which may result in a high barrier for the reaction. Is it possible that tubulin evolved a sheet → tube, two-step processes to increase the tubulin lateral assembly rate: a free tubulin dimer would first be captured by the fast-forming sheet bond, and this would give the formed cluster longer time to adjust to the more stable but slower-to-form tube bond. In a direct tube-bond formation mechanism, the interaction between the loosely formed contact pairs may be too weak to hold the newly added tubulin dimer for sufficiently long time before necessary conformational reorganization takes place to form the stable tube bond, which would result in very low lateral association rate.

We would like to propose here that there could be also a mechanical function for a preformed sheet that eventually closes into microtubule structure. Terrell Hill first proposed that assembly and disassembly of cytoskeletal filaments could generate mechanical force [37]. Subsequent theoretical studies and experimental measurements confirmed this idea [38,39,40,41]. Oster and coworkers proposed a ratchet mechanism and its variations to explain how elongating polymers like microtubules can generate force and push an object forward (see Fig. 2.8a) [42,43]. Thermal motions of the object and the polymer can produce space between them sufficiently large for a building unit (a tubulin dimer in this case) to add to the polymer's end. Addition of the new unit prevents

the object from moving back. Therefore, the random thermal motion of the object is ratcheted into directional motion at the expense of free energy released from unit addition. Most published work uses the ratchet model to explain force measurements during microtubule assembly [39,44]. With the sheet intermediate, the ratchet effect can generate force at the growing tip or at the zipping front, depending on the location of the load. Interestingly, it could also provide another active force generating mechanism in addition to the passive ratchet model. If the MT lateral bond is indeed stronger than the *sheet* lateral bonds, free energy would be stored in the lateral bonds of the sheet structure. Transformation to the MT structure is a cooperative process. When many lateral bonds transform together, they would release free energy much larger than that stored in a single lateral bond, thus enable them to push against larger loads. (Fig. 2.8b) In this way the energy accumulation step (tubulin bond formation) and the work-performing step (*tube* closure) are temporally and spatially separated. A similar mechanism of performing mechanical work using prestored energy has been proposed for the extension of the Limulus polyphemus sperm actin bundle [45] . Which mechanism dominates would depend on where the contact point between the MT and the load is and on the free energy difference between two types of lateral bonds.

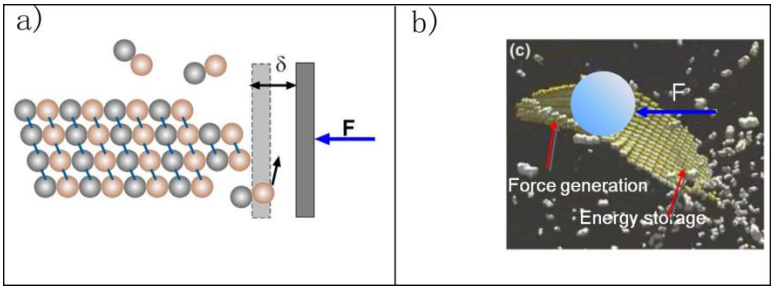

Figure 2.8. Schematic illustration of force generation models. (a) the ratchet model based on the dimer direct-addition model and (b) the possible force generation mechanisms for the new model.

f. Conclusion

In this study, using the single assumption that there are nearest-neighbor interactions between two consecutive PFs, together with existing structural information, we were able to generate a simple model to explain a large number of observations concerning the mechanism of microtubule assembly. We suggest that the sheet structure observed during microtubule growth may be a kinetically trapped intermediate, and that it is related to the ribbon structure stabilized at low temperature. Our model predicts that the sheet structures are more likely to be observed at high free tubulin concentrations. Structural studies of 2-PF clusters during the assembly process could provide information to discriminate among several possible mechanistic schemes.

Our current analysis has focused only on the initial stage of *in vitro* microtubule assembly. A future study should provide a more detailed description of the assembly process, especially the interface between the sheet bonds and the tube bonds along the longitudinal direction within the growing end of a microtubule. Our current treatment that all the lateral bonds within a pair of PFs are identical is clearly only an approximation. In this work we focused on the assembly dynamics of GMPCPP tubulins. We didn't include GTP hydrolysis dynamics and the resulting tubulin dimer conformational changes. We assume that the structural information extracted from the GMPCPP sheet structure can

be extrapolated to the normal assembly process. While supported by several other independent experimental evidences, this assumption requires further scrutiny. Especially we propose that at physiological conditions tubulins can form alternative lateral bond type other than that observed in microtubules, as evidenced in the doublet structure. If being confirmed, it would greatly modify our understanding on the mechanical properties of microtubules, and possible mechanisms of interactions between microtubules and microtubule association proteins (MAP) [2,34,46].

Our current model is essentially a two-dimensional model. The current simple model already provides many new insights on the very initial stage of the assembly process with only small cluster structures formed. Both the sheet and the MT forms are actually three-dimensional manifolds. More structural details are needed to fully account for the helical shape of the sheet and the microtubule structure. In the future a three-dimensional mechano-chemistry model parallel to what have been developed for the direct dimer-addition model would be needed [3,4].

g. Acknowledgements

We thank Drs Haixin Sui and Ken Downing for providing the doublet structure, and Dr Jian Liu for reading the manuscript and providing helpful comments.

h. References

1. Alberts B, Johnson A, Lewis J, Raff M, Roberts K, et al. (2002) Molecular Biology of the Cell. New York: Garland.

2. Howard J (2001) Mechanics of Motor Proteins and the Cytoskeleton. Sunderland, MA: Sinauer.

3. Molodtsov MI, Ermakova EA, Shnol EE, Grishchuk EL, McIntosh JR, et al. (2005) A molecular-mechanical model of the microtubule. Biophys J 88: 3167-3179.

4. VanBuren V, Cassimeris L, Odde DJ (2005) Mechanochemical Model of Microtubule Structure and Self-Assembly Kinetics. Biophys J 89: 2911-2926.

5. Nogales E, Wang HW (2006) Structural intermediates in microtubule assembly and disassembly: how and why? Curr Op Cell Biol 18: 179-184.

6. Erickson HP (1974) Microtubule surface lattice amd subunit structure and observations on reassembly. J Cell Biol 60: 153-167.

7. Chretien D, Fuller SD, Karsenti E (1995) Structure of Growing Microtubule Ends - 2-Dimensional Sheets Close into Tubes at Variable Rates. J Cell Biol 129: 1311-1328.

8. McIntosh JR, Grishchuk EL, Morphew MK, Efremov AK, Zhudenkov K, et al. (2008) Fibrils Connect Microtubule Tips with Kinetochores: A Mechanism to Couple Tubulin Dynamics to Chromosome Motion. Cell 135: 322-333.

9. Wang H-W, Nogales E (2005) Nucleotide-dependent bending flexibility of tubulin regulates microtubule assembly. Nature 435: 911-915.

10. Müller-Reichert T, Chrétien D, Severin F, Hyman AA (1998) Structural changes at microtubule ends accompanying GTP hydrolysis: Information from a slowly hydrolyzable analogue of GTP, guanylyl (α,β)methylenediphosphonate. Proc Natl Acad Sci U S A 95: 3661-3666.

11. Wang HW, Long S, Finley KR, Nogales E (2005) Assembly of GMPCPP-bound tubulin into helical ribbons and tubes and effect of colchicine. Cell Cycle 4: 1157-1160.

12. Summers K, Kirschner MW (1979) Characteristics of the polar assembly and disassembly of microtubules observed in vitro by darkfield light microscopy. J Cell Biol 83: 205-217.

13. Bergen LG, Borisy GG (1980) Head-to-tail polymerization of microtubules in vitro. Electron microscope analysis of seeded assembly. J Cell Biol 84: 141-150.

14. Nogales E, Whittaker M, Milligan RA, Downing KH (1999) High-Resolution Model of the Microtubule. Cell 96: 79-88.

15. Li H, DeRosier DJ, Nicholson WV, Nogales E, Downing KH (2002) Microtubule Structure at 8 Å Resolution. Structure 10: 1317-1328.

16. Fygensonm D, Needleman D, Sneppen K (2004) Variability-based sequence alignment identifies residues responsible for functional differences in α and β tubulin. Protein Sci 13: 25-31.

17. Amos L, Klug A (1974) Arrangement of subunits in flagellar microtubules. J Cell Sci 14: 523-549.

18. Sui H, Downing KH (2006) Molecular architecture of axonemal microtubule doublets revealed by cryo-electron tomography. Nature 442: 475-478.

19. Burton PR, Himes RH (1978) Electron microscope studies of pH effects on assembly of tubulin free of associated proteins. Delineation of substructure by tannic acid staining. J Cell Biol 77: 120-133.

20. Sept D, Baker NA, McCammon JA (2003) The physical basis of microtubule structure and stability. Pro Sci 12: 2257.

21. Rice LM, Montabana EA, Agard DA (2008) The lattice as allosteric effector: structural studies of alphabeta- and gamma-tubulin clarify the role of GTP in microtubule assembly. Proc Natl Acad Sci U S A 105: 5378-5383.

22. Hill TL (1985) Theoretical problems related to the attachment of microtubules to kinetochores. Proc Natl Acad Sci U S A 82: 4404-4408.

23. Erickson HP (1989) Co-operativity in protein-protein association : The structure and stability of the actin filament. J Mol Biol 206: 465-474.

24. Erickson HP, Pantaloni D (1981) The role of subunit entropy in cooperative assembly. Nucleation of microtubules and other two-dimensional polymers. Biophys J 34: 293-309.

25. Gillespie DT (1977) Exact Stochastic Simulation of Coupled Chemical Reactions. The Journal of Physical Chemistry 61: 2340.

26. VanBuren V, Odde DJ, Cassimeris L (2002) Estimates of lateral and longitudinal bond energies within the microtubule lattice. Proc Natl Acad Sci U S A 99: 6035-6040.

27. Vitre B, Coquelle FM, Heichette C, Garnier C, Chretien D, et al. (2008) EB1 regulates microtubule dynamics and tubulin sheet closure in vitro. Nat Cell Biol 10: 415-421.

28. Rice LM, Montabana EA, Agard DA (2008) The lattice as allosteric effector: Structural studies of {alpha}{beta}- and {gamma}-tubulin clarify the role of GTP in microtubule assembly. Proc Natl Acad Sci USA 105: 5378-5383.

29. Buey RM, Calvo E, Barasoain I, Pineda O, Edler MC, et al. (2007) Cyclostreptin binds covalently to microtubule pores and lumenal taxoid binding sites. Nat Chem Biol 3: 117-125.

30. Xu H, Wang J, Han S, Wang J, Yu D, et al. (2009) Hydrophobic-Region-Induced Transitions in Self-Assembled Peptide Nanostructures. Langmuir 25: 4115-4123.

31. O'Brien ET, Falvo MR, Millard D, Eastwood B, Taylor RM, et al. (2008) Ultrathin self-assembled fibrin sheets. Proc Natl Acad Sci U S A 105: 19438-19443.

32. Aggeli A, Nyrkova IA, Bell M, Harding R, Carrick L, et al. (2001) Hierarchical self-assembly of chiral rod-like molecules as a model for peptide beta-sheet tapes, ribbons, fibrils, and fibers. Proc Natl Acad Sci U S A 98: 11857-11862.

33. Miller WH, Handy NC, Adams JE (1980) Reaction path Hamiltonian for polyatomic molecules. J Chem Phys 72: 99-112.

34. Brangwynne CP, MacKintosh FC, Weitz DA (2007) Force fluctuations and polymerization dynamics of intracellular microtubules. Proc Natl Acad Sci USA 104: 16128-16133.

35. Schaap IAT, Carrasco C, de Pablo PJ, MacKintosh FC, Schmidt CF (2006) Elastic Response, Buckling, and Instability of Microtubules under Radial Indentation. 91: 1521-1531.

36. de Pablo PJ, Schaap IAT, MacKintosh FC, Schmidt CF (2003) Deformation and Collapse of Microtubules on the Nanometer Scale. Phys Rev Lett 91: 098101.

37. Hill TL (1981) Microfilament or microtubule assembly or disassembly against a force. Proc Natl Acad Sci U S A 78: 5613-5617.

38. Dogterom M, Yurke B (1997) Measurement of the Force-Velocity Relation for Growing Microtubules. Science 278: 856-860.

39. Schek HT, 3rd, Gardner MK, Cheng J, Odde DJ, Hunt AJ (2007) Microtubule assembly dynamics at the nanoscale. Curr Biol 17: 1445-1455.

40. Molodtsov MI, Grishchuk EL, Efremov AK, McIntosh JR, Ataullakhanov FI (2005) Force production by depolymerizing microtubules: a theoretical study. Proc Natl Acad Sci US A 102: 4353-4358.

41. Kerssemakers JWJ, Laura Munteanu E, Laan L, Noetzel TL, Janson ME, et al. (2006) Assembly dynamics of microtubules at molecular resolution. Nature 442: 709-712.

42. Peskin CS, Odell GM, Oster GF (1993) Cellular motions and thermal fluctuations: the Brownian ratchet. Biophys J 65: 316-324.

43. Mogilner A, Oster G (1999) The polymerization ratchet model explains the force-velocity relation for growing microtubules. Eur Biophys J 28: 235-242.

44. Gardner MK, Odde DJ (2006) Modeling of chromosome motility during mitosis. Curr Opin Cell Biol 18: 639-647.

45. Shin JH, Mahadevan L, Waller GS, Langsetmo K, Matsudaira P (2003) Stored elastic energy powers the 60-{micro}m extension of the Limulus polyphemus sperm actin bundle. J Cell Biol 162: 1183-1188.

46. Odde DJ, Ma L, Briggs AH, DeMarco A, Kirschner MW (1999) Microtubule bending and breaking in living fibroblast cells. J Cell Sci 112 (Pt 19): 3283-3288.

47. Koren R, Hammes GG (1976) A kinetic study of protein-protein interactions. Biochemistry 15: 1165-1171.

48. Northrup SH, Erickson HP (1992) Kinetics of protein-protein association explained by Brownian dynamics computer simulation. Proc Natl Acad Sci U S A 89: 3338-3342.

49. Martin SR, Schilstra MJ, Bayley PM (1993) Dynamic instability of microtubules: Monte Carlo simulation and application to different types of microtubule lattice. Biophys J 65: 578-596.

50. Bayley P, Schilstra M, Martin S (1989) A lateral cap model of microtubule dynamic instability. FEBS Lett 259: 181-184.

Table 2.1. Parameters used in the simulation.

Parameters	Values	References
Longitudinal bond strength extracting part of the entropy term ΔG_{long}	$-19\ k_BT$	[4,26]*
Sheet bond strength extracting part of the entropy term ΔG_{Sh}	Scheme 1: $-13.5 \sim -17.5\ k_BT$, Scheme 2: $-13\ k_BT$	varying parameter
Tube bond strength ΔG_{Tu}	Scheme 1: $-15.5\ k_BT$, Scheme 2: $-16.5\ k_BT$	[4,26]*
Energy barrier ΔG_{lactST}	$-9.5\ k_BT$	estimated
Entropy loss for two dimer assemble $\Delta G_{Entropy}(1 \rightarrow 2)$	$5.5\ k_BT$ †	[2,4]
Mutual interaction energy for sheet-sheet bonds ΔG_{ShSh}	Scheme 1: $0 \sim 6\ k_BT$, Scheme 2: $0\ k_BT$	varying parameter
Mutual interaction energy for *tube-tube* bonds ΔG_{TuTu}	Scheme 1: $0\ k_BT$, Scheme 2: $0 \sim 6\ k_BT$	varying parameter
Rate constant for longitudinal assemble at	$2\times10^6\ \mu\text{Ms}^{-1}$	[4,26,47,48,49,50]

plus end k_{long}		
Rate constant for longitudinal assemble at minus end k_{nLong}	$k_{Long} \times \delta$	[12,13]
Assemble ratio between minus and plus ends δ	$1/3$	[12,13]
Rate constant for lateral assemble with *tube* bond k_{Tu}	$5\times10^{3}\ \mu\mathrm{M}\cdot\mathrm{s}^{-1}$	[4]
Rate constant for lateral assemble with sheet bond k_{Sh}	$1\times10^{5}\ \mu\mathrm{M}\cdot\mathrm{s}^{-1}$	estimated
Rate constant for conversion between sheet and *tube* bonds k_{ST0}	$5\times10^{4}\ \mu\mathrm{Ms}^{-1}$	estimated
Tubulin concentration c	25 M unless specified otherwise	[9]

* Derived quantities, See Supporting Text S1 B for explanation.

†The entropy term for processes other than 1→2 is discussed in Supporting Text S1 B.

i. Supplemental Information

Supporting Text S1

A. Rate constants in the model: As discussed in the main text, three types of basic reactions are considered in our model (Fig. 2.2a). The following formula give the corresponding reaction rates satisfying detailed balance:

1) Longitudinal On/Off: The reaction rate constants for dimer addtion/dissociation from the plus end of a protofilament are given by

$$k_L^{N\to N+1} = k_L^{1\to 2}$$

$$k_{-L}^{N+1\to N} = k_L^{N\to N+1}\exp\left(\left(\Delta G_{long} + i\Delta G_{lat} + \Delta G_{Entropy}(N\to N+1)\right)/\, k_B T\right)$$

where k_{-L} is the disassociating rate, related to the associating rate k_L by the effective binding free energy. We assume that the association rate is independent of the protofilament length. ΔG_{long} is the longitudinal bond binding energy, ΔG_{lat} is the binding energy for a lateral bond, which can be either *tube* bond or sheet bond. The corresponding values are ΔG_{Tu} and ΔG_{Su}. The number *i* refers to the number of lateral bonds formed during the association process, which ranges from 0 to 2. $\Delta G_{Entropy}$ accounts for lose of translational and rotational entropy during the association process, which is defined as positive. $\Delta G_{Entropy}(N\to N+1)$ represents the entropic portion of the energy corresponding to adding one dimer onto the cluster with N dimers. For small N, $\Delta G_{Entropy}(N\to N+1)$ also depends on the cluster shape. Its calculation is discussed below. The term k_B is the Boltzmann constant, and T is the temperature in Kelvin. The

minus end longitudinal reactions are the same as plus end reactions, except for a constant factor δ ~ 0.3 [1]

2) Lateral On/Off: The rate constants for one dimer lateral association or disassociation from the cluster are

$$k_{-Tu} = k_T \exp\left(\Delta G_{Tu} / k_B T + \Delta G_{Entropy}(1 \to 2) / k_B T\right),$$
$$k_{-Sh} = k_S \exp\left(\Delta G_{Sh} / k_B T + \Delta G_{Entropy}(1 \to 2) / k_B T\right),$$

Where subscript *Tu* stands for *tube* binding, and *Sh* stands for sheet binding. Lateral association rates k_{Tu} and k_{Sh} are determined by comparing existing model parameters and proposed mechanism. k_{-Tu} and k_{-Sh} are disassociation rates. Free energies are defined in the same way as for the longitudinal reaction.

3) Switch of lateral bonds: The conversion rate constants between *sheet* bond and *tube* bond are given by

$$k^n_{Tu \to Sh} = k^0 \exp\left(n\left(\Delta G_{Tu} + \varepsilon \Delta G_{TuTu} - \Delta G^+\right)/ k_B T\right),$$

$$k^n_{Sh \to Tu} = k^0 \exp\left(n\left(\Delta G_{Sh} + \zeta \Delta G_{ShSh} - \Delta G^+\right)/ k_B T\right)$$

where the activation energy, $\Delta G^+ > \Delta G_{Tu}, \Delta G_{Sh}$, is the energy barrier between two bond types, k^0 is a constant, ΔG_{ShSh} and ΔG_{TuTu} are the allosteric terms in Scheme 1 and Shceme 2 (see supporting text C and also in main text), respectively. The parameters ε and ζ can assume values 0, 1, or 2, depending on the lateral bond types of neighbor

filament pairs. For instance, $\zeta = 0$ if both neighbor filament pairs have tube bonds. The switching rates decrease quickly with increasing number of lateral bonds.

B. Calculation of the entropic contribution: Erickson discussed the necessity of treating different free energy contributions, especially the translational and rotational entropy, separately [2]. He discussed the situation adding one tubulin dimer to a large growing microtubule. In our case the system starts with dimers, and form larger and larger clusters. Therefore, we will need to generalize the procedure of Erickson, as discussed below.

The entropic term appears in both longitudinal and lateral reactions. In our model, we consider only the rotational and translational entropic energy. To estimate $G_{Entropy}$, we consider the partition function of rotational and translational motion of a cluster with N dimers,

$$Q_N = q_N^t q_N^r;$$

where N is the total number of dimers in the cluster. The subscript t stands for translation and r for rotation. The entropy can then be written as

$$S_1 = k_B \log Q_1 + k_B T \frac{\partial}{\partial T} Q_1$$
$$S_N = k_B \log Q_N + k_B T \frac{\partial}{\partial T} Q_N$$

where S_1 and Q_1 are the entropy and the partition function for one dimer, respectively. We approximate a dimer as a rectangular cuboid with dimensions $h_{height} \times d \times w$. A cluster

has a structure (approximately) of a cuboid of dimensions $H \times D \times W$, with $H = \langle n_h \rangle \cdot h_{height}$, $D = d$, and $W = n_w \cdot w$. $\langle n_h \rangle$ is the average number of dimers along the longitudinal direction. n_w is the number of filaments.

Therefore, the partition function can be written as:

$$q_N^t = \left(\frac{2\pi n_w n_h m k_B T}{h^2} \right)^{3/2} V$$

$$q_N^r = \pi^{1/2} \left(\frac{8\pi^2 k_B T}{h^2} \right)^{3/2} \left(I_{hN} I_{wN} I_{dN} \right)^{1/2},$$

where *V* is the volume, and *h* is the Planck's constant. The principal moments of inertia for a cuboid structure are

$$I_{hN} = \frac{1}{12} m n_w n_h \left(n_w^2 w^2 + d^2 \right);$$
$$I_{wN} = \frac{1}{12} m n_w n_h \left(n_h^2 h_{height}^2 + d^2 \right);$$
$$I_{dN} = \frac{1}{12} m n_w n_h \left(n_w^2 w^2 + n_h^2 h_{height}^2 \right).$$

Combining all the equations above, we have

$$\Delta G_{Entropy}(N \to N+1) = -T \Delta S_{N,1 \to N+1} = -T(S_{N+1} - S_N - S_1) = F(n_w, \langle n_h \rangle) \Delta G_{Entropy}(1 \to 2)$$

where $F(n_w, n_h)$ is in general a function of $N = n_w n_h$ (derived from the partition functions given above) that represents the entropic energy ratio of adding one dimer to the cluster with *N* dimers versus adding one dimer to another dimer. Erickson pointed out that

calculating $\Delta G_{Entropy}(N \to N+1)$ directly from the corresponding partition function result in overestimation [2,3]. Instead the above relation allows us to link $\Delta G_{Entropy}(N \to N+1)$ to $\Delta G_{Entropy}(1 \to 2)$. The value of $\Delta G_{Entropy}(1 \to 2)$ is obtained by requiring that when *N* is large, $\Delta G_{Entropy}(N \to N+1)$ tends to a constant value of $\sim 10\ k_B T$, as suggested by Erickson and by Howard [2,3]. The value of the overall binding free energies (~ – 9 $k_B T$ for longitudinal, and ~ – 5.5 $k_B T$ for lateral tube binding interactions) are close to what used in other model studies [4].

We want to point out that the detailed treatment of the binding energy, especially the entropic term, is not essential for the conclusion made in the main text. However, it makes the model more consistent, since the dependence of entropic change on the cluster size can affect the rates by orders of magnitude [3].

C. Physical origins of the temperature dependence of the free energy terms:

1) For Scheme 1, we focus on the temperature dependence of $(\Delta G_{Sh} - \Delta G_{Tu})$. Physically the potential near a stable protein conformation can be approximated as a set of harmonic potentials,

$$V = V_0 + \frac{1}{2}\sum_i \kappa_i x_i^2$$

where $\{\kappa\}$ are spring constants. The harmonic approximation makes the following analysis easy, but is unnecessary for reaching our final conclusion. The corresponding

classical partition function (we neglect quantum effects which don't change the result qualitatively here) is

$$Q = \int e^{-\frac{1}{k_B T}\left(V_0 + \sum_i \frac{1}{2}\kappa_i x_i^2\right)} dx_1 dx_2 ... dx_N = e^{-\frac{1}{k_B T}V_0} \prod_i \left(\frac{2\pi k_B T}{\kappa_i}\right)^{1/2}$$

The free energy is

$$\begin{aligned} G &= -k_B T \ln Q \\ &= -\frac{1}{2} k_B N T \ln T + k_B T \ln\left(\prod_i \left(\frac{\kappa_i}{2\pi k_B}\right)^{1/2}\right) + V_0 \\ &= -\alpha T \ln T + \beta(\kappa) T + V_0 \end{aligned}$$

and the free energy difference $\Delta G_{Sh} - \Delta G_{Tu} = (V_{S0} - V_{M0}) + (\beta_{Sh} - \beta_{Tu})T$, where α and $\beta(\kappa)$ are positive. Therefore it is possible that $(\Delta G_{Sh} - \Delta G_{Tu})$ changes sign on increasing temperature, as shown schematically in Fig. 2.S3a.

The sign change of $(\Delta G_{Sh} - \Delta G_{Tu})$ upon increasing temperature implies the entropy change $(\Delta S_{Sh} - \Delta S_{Tu} < 0)$. Another possible source of entropy change is through liberation of water molecules initially bound to protein surfaces. When two protein surfaces interact, some water molecules initially constrained to the surfaces are released to the solution. This can be a huge contribution to entropy increase. Our cryo-EM images reveal more extensive contact surface for the tube bond than for the sheet bond (see Fig. 2.3). Therefore one might expect more water molecules released upon the tube bond formation than the sheet bond formation, which contributes the relation

$(\Delta S_{Sh} - \Delta S_{Tu} < 0)$. Structures at higher resolution will aid in evaluating this hypothesis. With current information, we cannot provide further quantitative analysis.

2) In Scheme 2 we assume that some conformational change (the allosteric effect) accompanies formation of two neighboring lateral bonds. Let's denote the reaction coordinate linking the initial and final conformations *s*. The potential part of the reaction path Hamiltonian [5] along *s* can be written in the classical form

$$V(s) = V_0(s) + \sum_i \frac{1}{2}\kappa_i(s)x_i^2$$

The classical partition function for the potential of mean force is given by

$$Q(\bar{s}) = \int e^{-\frac{1}{k_B T}V(s)}\delta(s-\bar{s})\prod_i dx_i ds = \exp\left(-\frac{1}{k_B T}V_0(s)\right)\prod_i\left(\frac{2\pi k_B T}{\kappa_i(\bar{s})}\right)^{1/2}$$

Therefore the free energy change due to the allosteric effect induced conformational change $\Delta G \equiv G(s_b) - G(s_0) = -k_B T(\ln Q_b - \ln Q_0)$ is in the form $\Delta G = V_0(s_b) - V_0(s_0) + (\beta(s_b) - \beta(s_0))T$. The term β is defined similarly to what in part 1, except here β is dependent on conformational coordinate *s*. If $\beta_{s_b} < \beta_{s_0}$, the allosteric effect ΔG_{TuTu} decreases as temperature increase (see Fig. 2.S3b). For simplicity we assume that only the allosteric interaction between two consecutive lateral *tube* bonds is appreciable, although the model can be easily generalized. The simulation results based on this scheme are shown in Fig. 2.S4. The figure shows the percentage of ribbon structures at different values of ΔG_{TuTu}. As discussed above, the different values

of ΔG_{TuTu} correspond to different temperatures. The figure shows that smaller ΔG_{TuTu} values (higher temperature) give lower percentage of ribbon structures than larger ΔG_{TuTu} values do. For $\Delta G_{TuTu} = 6k_BT$, the clusters contain over 90% ribbon structures, compared to the 10% for $\Delta G_{TuTu} = 0k_BT$. The results indicate that Scheme 2 is a good alternative explanation to the existing experimental data. To discriminate between Schemes 1 and 2, more data, especially the structures with 2 PFs, would be needed.

We want to point out that entropy is the primary driving force for many biological processes, e.g., hydrophobic interactions. It is physically reasonable that the entropy term leads ($\Delta G_{Sh} - \Delta G_{Tu}$) to change its sign upon temperature change, especially if ΔG_{Sh} and ΔG_{Tu} are very close, as what we used in this work. Experimentally we found that at physiological magnesium concentration, GMPCPP tubulins form normal microtubule structure at 37^{o}C, but only short single PF structures at lower temperature. These observations are consistent with our assumption that entropy has large contribution to the lateral bond energies. Increasing the temperature stablizes both types of the lateral bonds, which, esp. the sheet bond, can be further stabilized by increasing the magnesium concentration. Alternatively, one may suggest a kinetic explanation for the lacking of larger structures at lower temperature: the lateral bond formation rates are too slow. However, no larger structure is observed at longer time (in hours). This observation doesn't support the kinetic explanation.

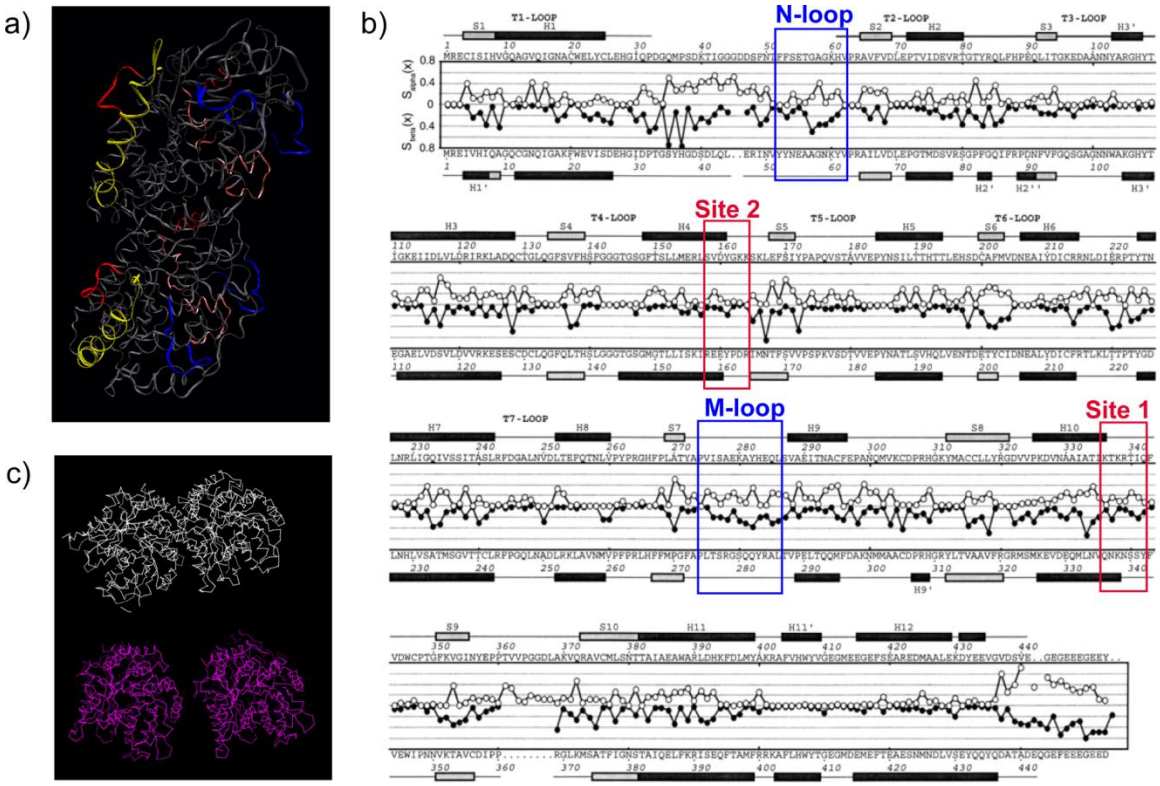

Figure 2.S1. Structural basis for the two types of lateral bonds. (a) Structure of the $\alpha\beta$-tubulin dimer with residues involved in lateral interactions indicated. Blue: residues engaged in lateral *tube* bonds (274-286, 52-61). Red: residues engaged in lateral *sheet* bond (336-342, 158-164) (these residues have been identified by docking the high-resolution tubulin structure into the 18 Å reconstruction of the ribbon [6], and therefore are correct within the constraints of the limited resolution). Pink and yellow: possible surface residues (108-130, 209-225, 300-311) along the *tube*-sheet conversion pathway. (b) Variability-based sequence alignment of $\alpha-$ and $\beta-$ tubulin performed by Fygenson et al. [7]. The blue and red boxes indicate the residues involved in the *tube* and *sheet* bond formation given in (a), respectively. The figure is adapted from Fig. 2.2 of Fygenson et al. [7] with permission. (c) Comparison of the non-MT lateral interactions observed in the microtubule doublet of axonemes (top) [8] (PDB file provided by Sui and Downing) and the ribbon structures (bottom) [6].

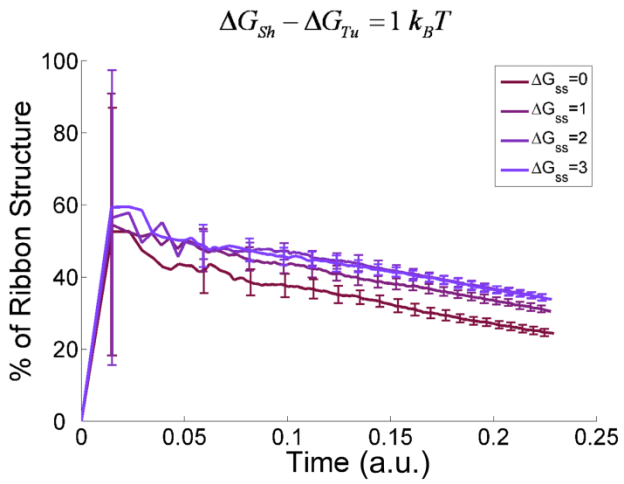

Figure 2.S2. Effect of variable ΔG_{ShSh} on the assembled structures with $\Delta G_{Sh} = -14.5\ k_B T$ and $\Delta G_{Tu} = -15.5\ k_B T$ ($\Delta G_{Sh} - \Delta G_{Tu} = 1\ k_B T > 0$). The figure shows the percentage of ribbon structures as a function of the time for ΔG_{ShSh} = 0, 1, 2 and 3 $k_B T$, as indicated.

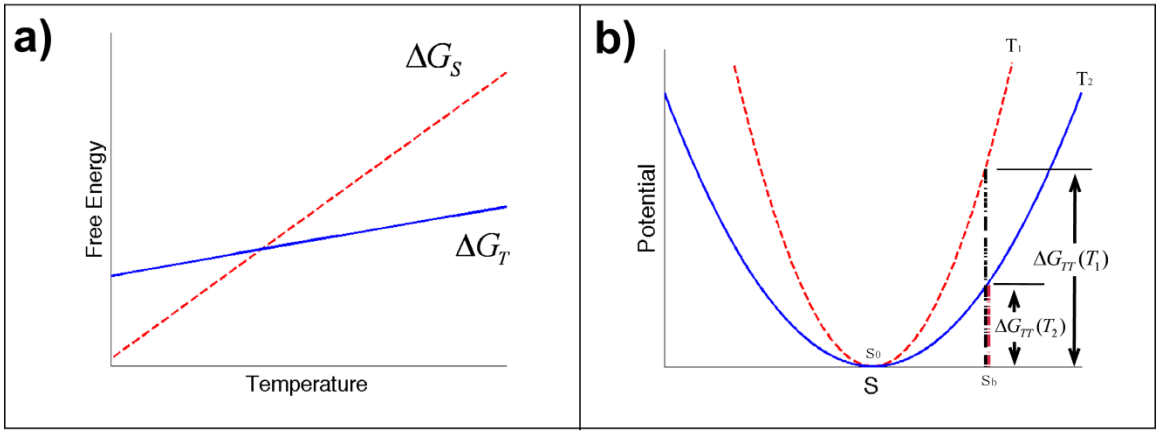

Figure 2.S3. Schematic Illustration of the physical origins of the temperature dependence of the free energy terms. (a) ΔG_{Sh} and ΔG_{Tu} have different temperature dependence and their

difference changes sign over *T*. (b) The dependence of ΔG_{TuTu} on the conformational coordinate describing the necessary collective conformational change upon forming two neighboring lateral *tube* bonds varies with temperature.

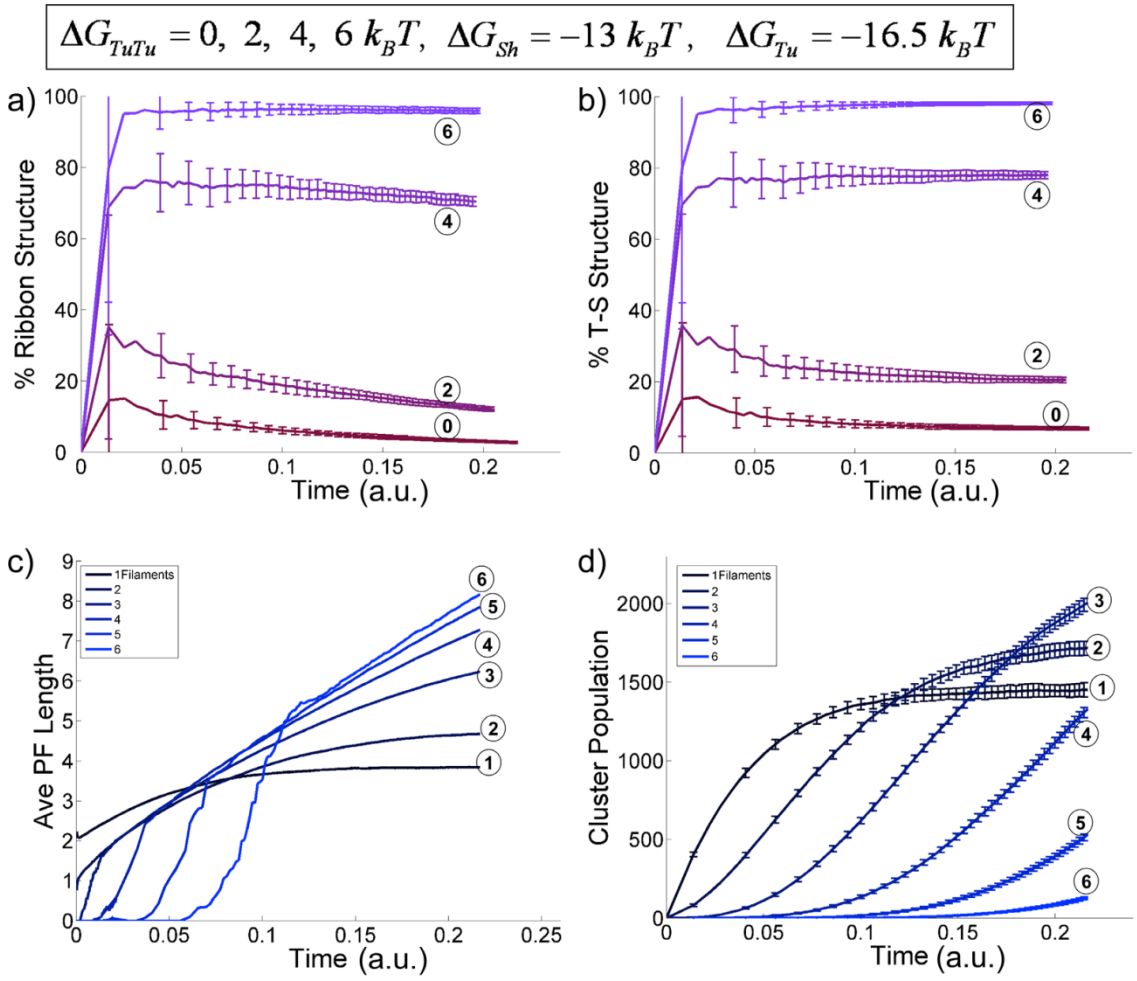

Figure 2.S4. Effects of variable ΔG_{TuTu} on the assembly structures using the Scheme 2 described in Fig. 2.S3b. (0, 2, 4, and 6 k_BT, as indicated by corresponding circled numbers). Different ΔG_{TuTu} correspond to different temperatures as showed in Fig. 2.S3b and supporting text C. $\Delta G_{Sh} = -13\ k_BT$ and $\Delta G_{Tu} = -16.5\ k_BT$ were used for all simulations. Other parameters

are the same as in the Scheme 1 described in detail in the main text. The final results are averaged over 60 independent simulations. (a) Percentage of ribbon structure v.s. simulation step. (b) Percentage of T-S structure. (c) Average PF length for clusters of different size (1 to 6 PFs as indicated by circled numbers), with $\Delta G_{TuTu} = 2\ k_B T$. (d) Cluster population for clusters of different size (1 to 6 PFs as indicated by circled numbers), with $\Delta G_{TuTu} = 2\ k_B T$.

`

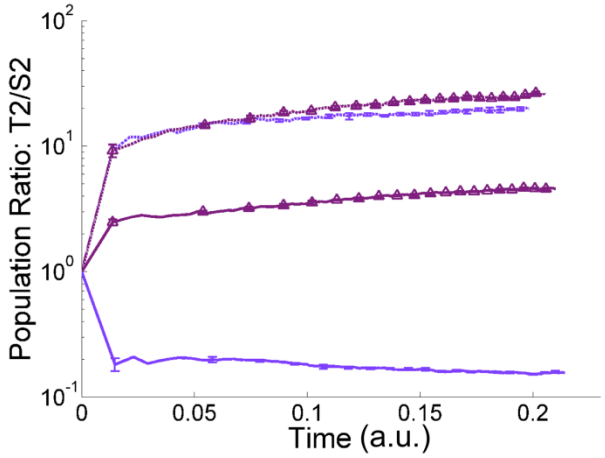

Figure 2.S5. Population ratio of *tube*-cluster versus *sheet*-cluster for 2-PF structures as a function of time. Solid and dashed lines with triangles correspond, respectively, to Scheme 1 ($\Delta G_{ShSh} > 0$, $\Delta G_{TuTu} \sim 0$, $\Delta G_{Sh} - \Delta G_{Tu} = 1.5\ k_B T$, $\Delta G_{ShSh} = 6\ k_B T$) and to Scheme 2 ($\Delta G_{TuTu} > 0$, $\Delta G_{ShSh} \sim 0$, $\Delta G_{Sh} - \Delta G_{Tu} = 3.5\ k_B T$, $\Delta G_{TuTu} = 2\ k_B T$), both at high temperature . The lines without triangles are for Scheme 1 (solid line, $\Delta G_{Sh} - \Delta G_{Tu} = -1.5\ k_B T$. $\Delta G_{ShSh} = 6\ k_B T$) and Scheme 2 (dashed line, $\Delta G_{Sh} - \Delta G_{Tu} = 3.5\ k_B T$ $\Delta G_{TuTu} = 6\ k_B T$) at low temperature.

Supporting References

1. Summers K, Kirschner MW (1979) Characteristics of the polar assembly and disassembly of microtubules observed in vitro by darkfield light microscopy. J Cell Biol 83: 205-217.

2. Erickson HP (1989) Co-operativity in protein-protein association : The structure and stability of the actin filament. J Mol Biol 206: 465-474.

3. Howard J (2001) Mechanics of Motor Proteins and the Cytoskeleton. Sunderland, MA: Sinauer.

4. VanBuren V, Cassimeris L, Odde DJ (2005) Mechanochemical Model of Microtubule Structure and Self-Assembly Kinetics. Biophys J 89: 2911-2926.

5. Miller WH, Handy NC, Adams JE (1980) Reaction path Hamiltonian for polyatomic molecules. J Chem Phys 72: 99-112.

6. Wang H-W, Nogales E (2005) Nucleotide-dependent bending flexibility of tubulin regulates microtubule assembly. Nature 435: 911-915.

7. Fygensonm D, Needleman D, Sneppen K (2004) Variability-based sequence alignment identifies residues responsible for functional differences in α and β tubulin. Protein Sci 13: 25-31.

8. Sui H, Downing KH (2006) Molecular architecture of axonemal microtubule doublets revealed by cryo-electron tomography. Nature 442: 475-478.

Chapter 3

Alternative tubulin lateral interactions with functional roles in microtubule mechanics and assembly dynamics

Zhanghan Wu[1], Eva Nogales[2,3], Jianhua Xing[1]

[1]Department of Biological Sciences, Virginia Polytechnic Institute and State University, Blacksburg, VA 24061

[2]Lawrence Berkeley National Laboratory Berkeley, CA 94720

[3] Howard Hughes Medical Institute, and Department of Molecular Cell Biology, University of California, Berkeley, CA 94720

a. Abstract

The dynamic assembly and disassembly of microtubules and the mechanical properties of these polymers are essential for many key cellular processes. Mathematical and computational modeling, especially coupled mechano-chemical modeling, has contributed significantly to our understanding of microtubule dynamics. However, critical discrepancies exist between experimental observations and modeling results that need to be resolved before further progress towards a complete model can be made. Open sheet structures ranging in size from several hundred nanometers to one micron long have often been observed at the growing ends of microtubules in *in vitro* studies. Existing modeling studies predict these sheet structures to be short and rare intermediates of microtubule disassembly rather than important components of the *assembly* process. Atomic force microscopy (AFM) studies also reveal interesting step-like gaps of the force-indentation curve that cannot yet be explained by existing theoretical models. We carried out computational studies to compare the mechanical properties of two alternative models, one corresponding to the existing, conventional model, with the other considering an additional type of tubulin lateral interaction described in a cryo-EM structure of a proposed trapped intermediate in the microtubule assembly process. Our analysis shows that only the second model can reproduce the AFM results over a broad parameter range. We suggest additional studies using AFM tips with different sizes can further distinguish the validity of the two models.

b. Introduction

Microtubules (MTs) are long hollow cylindrical polymers consisting of about 13 parallel protofilaments (PF) formed by the head-to-tail assembly of $\alpha\beta$ -tubulin heterodimers. The outer and inner diameters of MTs are about 25 nm and 15nm, respectively, whereas the length can vary from tens of nanometers to tens or even hundreds of micrometers, frequently spanning the whole cell. MTs serve as one of the three major cytoskeletal components in eukaryotic cells, acting as mechanical support for cells and as both the stage and a player in many eukaryotic cellular processes, including intracellular transport, cell motility, mitosis and meiosis [1-3]. MT dynamic instability is known to be a key property for MT function. Various proteins interact with MTs for their precise cell regulation and function [4, 5]. The regulation of MT dynamics has been shown to be both of great biological significance during cell division, and of outstanding pharmaceutical value. Many popular diseases are found to be strongly related to the malfunctioning of MT assembly. Huntington's disease (HD) is an autosomal dominant inherited neuro-degenerative disease presenting progressive involuntary movements and cognitive changes. Its gene product has been shown to interact with polymerized MTs [6]. Depolymerization of MTs by toxins such as rotenone disrupts vesicular transport and is found to be related to neurodegenerative diseases such as Parkinson's and Alzheimer's disease [7-10]. Down syndrome, one kind of severe genetic disease, is known to be caused by chromosome missegregation which may be due to mitotic spindle MT defects or defects in MT-chromosome binding. Therefore, MTs and their associated proteins are often serve as therapy targets [11].

For instance, Taxol® is one broadly used anticancer drug targeting MTs. It disrupts the fastly dividing cancer cells by altering MT dynamics. MT-stablizing drugs are also used in Alzheimer's disease treatment [12, 13]. Bending resistance and local deformation are also essential for many MT functions. MTs form the mitotic spindle that engages, aligns and segregates chromosomes during cell division. Many unicellular eukaryotic organisms and also many cells of higher eukaryotes (such as sperm cells or lung epithelial cells) possess cilia or flagella, specialized MT-base structures, to propel themselves or to pump fluid. MTs also form the core of neuronal axons. There have been extensive studies investigating the responses of MTs to mechanical stress [14-35]. The non-linear response of MTs bending, especially buckling, is not fully understood. Moreover, the linear mechanical properties of MTs under various conditions (different binding proteins, different assembly conditions, etc.) are still under debate. For instance, different labs have reached different conclusions on whether a pure MT or Taxol treated MT has higher Young's modulus [14, 28-32]. Even for the same type of MTs, variation from different experiments is as much as 2 orders of magnitude (see Table 3.S1 which summarizes some published results).

Understanding the nano-mechanical properties and assembly/disassembly dynamics of MTs is a fundamental problem and an active research topic in molecular cell biology and in material science [28, 36-49]. Currently, the canonical model assumes that MT assembly is a simple process in which individual $\alpha\beta$ -tubulin hetero-dimers add one by one onto the growing end of a MT [50, 51]. Mathematical modeling with this model (which we will refer to as L1) has had significant success on explaining a number of experimental observations. However, there are a number of experimental indications

that alternative, non-microtubular interactions exist during the microtubule polymerization process in the form of an assembly intermediate. They come from the visualization by EM of open sheet structures at the growing end of microtubules [52] [53-55] [56], and from the cryo-EM structure of a tubulin polymer that has been proposed to mimic such growth sheets, to which we refer to as “ribbon”, that was obtained in the presence of GMPCPP and high magnesium, at low temperatures [21, 57] [58]. This ribbon structure, which converts directly into MTs upon raising the temperature, is formed by two types of alternating lateral interactions between PFs: one type of interaction is indistinguishable from that in MTs, which we call the tube bond (we refer to a noncovalent contact as a bond in order to follow the convention in the field [59]), and the other is a new type of interaction, which we call the sheet bond [58, 60]. Because the ribbon structure was obtained under distinct conditions from those normally used for the in vitro assembly of microtubules, most significantly at low temperatures, there has been some skepticism about whether the observed new lateral contact is an artifact without physiological significance. However, as we have previously noticed, there is an in vivo precedent of alternative lateral interactions between microtubules [58, 61]: the doublet MT arrangement present in axonemes . In a doublet one particular PF interacts with two PFs simultaneously, with one interaction resembling the tube bond and the other structurally resembling the sheet bond [58, 61]. Interestingly, we also noticed that bioinformatics studies indicate that the residues proposed to participate in the sheet bonds are evolutionarily more conserved than those forming the tube bonds[58, 62], a fact that suggests that these residues are functionally essential.

We have previously formulated a computational model (which we will refer to as L2) that considers the two types of lateral interactions during early tubulin assembly states [58]. We believe that recent experimental studies further suggest that a systematic analysis on this alternative bond type is timely and needed. There are still unresolved contradictions between experimental observations and computational modeling results based on the L1 model. Following the observation that the fast growth of MTs occurs via the elongation of an outwardly curved sheet-like structure, Chretien and coworkers performed theoretical studies on the sheet structure using a continuum elastic model and assuming only one type of lateral bond [41, 56]. These studies explained the sheet structures with different curvatures as incomplete MTs with different number of PFs. However, one should treat the conclusions from this continuum model studies with some caution. In particular, that work did not address how and whether the *a priori* assumed sheet structure can form within in the first place the canonical L1 model. Systematic stochastic modeling studies by VanBuren et al. show that, based on the L1 model, long incomplete structures at an MT growing end are very unlikely to form. Such structures appeared both energetically and kinetically unfavorable and are precursors for disassembly rather than assembly [48]. These authors did not examine dependence of sheet length on tubulin concentration. One would expect in their model weak or inverse dependence, since low tubulin concentrations favor disassembly and, thus, sheet formation according to VanBuren et al. [48]. This is in contradiction to the observation that the sheet structures are observed under growth conditions and become longer upon increasing tubulin concentrations [56].

We propose that the existence of the sheet bond affects MT assembly dynamics and its regulation mechanism. A large number of proteins regulate MT assembly and disassembly dynamics *in vivo* through interaction with tubulin, most especially at the plus end of a growing MT [4, 5]. The sheet bond would provide an alternative binding surface for those proteins to discriminate between the body and the tip of a microtubule [60].

Finally, the existence of the sheet bond would have a significant effect on the mechanical properties of MTs. Although the body of the MT should not contain sheet bonds under normal conditions, mechanical stress may transform some of the lateral bonds to sheet bonds locally as it distorts MTs. MTs *in vivo* are constantly under large mechanical tension [17, 25, 63]. Without breaking the MT, the mechanism of converting lateral bonds to sheet bonds may release some of the mechanical stress. Consequently, sheet bonds could serve as temporary alternative interaction between protofilaments that maintain some stability in the distorted MT. The above hypothesis is consistent with recent structural studies of Sui and Downing[64], and the AFM studies of Schaap and coworkers [65, 66]. Schaap et al. pushed onto a MT using an AFM tip and measured the indentation distance as a function of the force applied. They observed backward steps (sudden drops in the force needed to induce further indentation) and suggested that the tube-to-sheet transition was one possible explanation for this observation. Interestingly, the process was reversible. Upon removing the AFM tip, the original MT structure was recovered.

Our objective was to determine if a sheet bond is required to explain the mechanical data by analyzing models with one or two types of lateral bonds against

experimental data. Given the uncertainty of some key parameters, our strategy here has been to first develop a mathematical framework capable of describing both types of models, and then examine their predictions within the physically relevant parameter space. We have focused on the mechanical studies of Schaap et al, and will report analysis concerning MT assembly dynamics in a future study.

c. Methods

The model: The size of the system that we are trying to study together with the lack of high resolution structural information make molecular dynamics simulations at the atomistic level impractical and unreliable. Instead we have used a coarse-grained modeling framework that treats an assembly of α and β tubulins as rigid bodies connected by elastic springs. For better comparison with previous studies, we choose the mathematical structure of our models to resemble the work of VanBuren et al. on the canonical L1 model (48) as much as possible (See Figure 3.1). VanBuren et al. modeled tubulin dimers as connected vectors. We expand the representation in two major aspects. First, we treat each monomer as a rigid body, and allow both intra- and inter-dimer bending motion, to be consistent with experimental observations. Second, each dimer has spatially distributed lateral interaction sites, similar to the model of Molodtsov et al.(67), but with extra binding sites corresponding to the sheet bonds for the L2 model. There are more degrees of freedom than those existing models, which are necessary to fully describe the heterogeneous tubulin lateral interactions. Figure 3.1a-c illustrate the basic modes of three-dimensional motion related to both longitudinal and lateral tubulin-tubulin interactions, and the composite sheet-tube bond conversion central to the L2 model.

Figure 3.1d & e summarize the mathematical details of the L1 and L2 models. For each PF, with the assumption that neighboring tubulins are head-to-tail connected, the degrees of freedom for each monomer is reduced to four, with (*L, θ, φ, ψ*) defining the relative position and orientation of a monomer relative to the previous one on the same PF. Exception is the first α-tubulin in each PF, which requires three additional coordinates to define the starting spatial position of the PF relative to the laboratory frame. To facilitate the description, we also define several auxiliary variables using the four basic coordinates. Following VanBuren et al., we define Φ as the angle between the preferred and the actual orientation of the vector representing a monomer. Each monomer has an internal coordinate frame, with the x-axis along the connection between the center of mass (COM) and the middle of the two lateral interaction sites on one site, the z axis along the connection between the COM of the α tubulin and the longitudinal interaction site of the two intra-dimer tubulins, and the y axis perpendicular to the x-z plane. Then we define Φ_s and γ_r to describe the lateral shift and rotation relative to the COM (see Figure 3.1e and Figure 3.S1).

With the above mathematical representation, we introduce individual free energy terms to define the longitudinal and lateral interactions between monomers. Longitudinally there are stretching (changing of *L* relative to its equilibrium value), bending (changing of θ and ϕ), and torsion terms (changing of ψ) (Figure 3.1a & c). Laterally there are stretching (changing of *d*), shifting (changing of Φ_s), and rotation terms (changing of γ_r) (Figure 3.1b & e, Figure 3.S1). Each energy term is represented by a truncated harmonic potential in the form $E=\frac{1}{2}k(x-x_e)^2+E_0$ within a cutoff x_c, and zero otherwise

(Figure 3.1f). For simplicity we neglect possible cross terms. The sheet and tube bonds have different equilibrium values of *d,* Φ_s , and γ_r , respectively. Two monomers can switch between the sheet and tube bonds (see Figure 3.1c&g), with a double-well shaped composite potential along the switching coordinate (as a combination of Φ_s and γ_r , see Figure 3.1i). To obtain the L1 model, one simply sets the sheet bond related spring constants and E_0 to be zero, resulting in a single-well shaped potential (Figure 3.1h&i). Figure 3.1i shows two such potentials corresponding to a stiff and a sloppy tube bond, respectively. The total energy (potential of mean force to be more precise) of the structure is then summed over all the potential function terms.

Numerical methods: All model parameters are listed in Table 1, unless otherwise mentioned. Some of the parameters are estimated from available experimental data, and inherited from the model of VanBuren et al. For parameters lacking experimental data, we vary the values over physically feasible ranges and analyze the model behavior. We obtain the stable conformations by minimizing the total energy of the structure using the Quasi-Newton method and the simplex approach (68). The local minimization algorithms allow us to obtain metastable structures. To simulate AFM experiments, we first constructed a stable MT form, and then exerted a sphere shaped AFM tip to the MT wall. At each step, the AFM tip moves a small step (0.2 nm in our simulations) down to the MT wall, and then the stable conformation is obtained by minimizing the total energy including the hard-sphere interactions between tubulin monomers (modeled as spheres with diameter 4 nm) and the AFM tip. We calculated the force exerted by the tip by equating the MT lattice energy change to the work (force $\times$ displacement step) done by the tip.

Further details of the model can be found in the online supplemental information.

d. Results

The L2 but not L1 model can reproduce the AFM studies on MT wall deformability by force

Figure 3.2a schematically describes the AFM experiments of Schaap et al. [27, 65, 66]. The AFM tip pushes onto the surface of a Taxol stabilized MT that has been immobilized on a glass slide. The experiment measures the force-indentation (F-I) curve, that is, the force exerted on the MT wall versus the indentation that the AFM tip causes on the MT wall. A typical experimental curve is reproduced in Figure 3.2b. The curve can be divided into 5 regions: region 0 corresponds to an indentation < 0 while the AFM tip has not yet touched the MT wall; region 1 corresponds to indentations from 0 to the value indicated by the red dashed line shown in Figure 3.2b, where the mechanical response is linear, and the slope of $0.074 \pm 17\%\ \mathrm{N/m}$ reflects the effective spring constant of the MT wall; often there is a step-like "gap" ~0.6 nm wide that follows region 1, and which we label region 2; in region 3, the mechanical response is again quasi-linear; finally, in region 4 the response is non-linear, implying that the MT can no longer hold its integral structure.

We performed computer simulations using the L1 and L2 models and mimicking the experimental conditions closely. Figure 3.2c-d and an online supporting movie (Mov 1 of the supplementary material) show that the L2 model can reproduce the gap (region 2 in the curve). As the AFM tip compresses the MT, the tubulin dimers around the contact region are under mechanical stress (step 1 in Figure 3.2c-d), and give the first linear

response region of the F-I curve. The stress eventually builds up, until the convertion of some sheet bonds into tube bonds releases some of the stress, and results in the gap (step 2). Further compression leads to a quasi-linear response again. Our model predicts that during the process additional sheet-to-tube bond conversion may take place, which results in new gaps (step 3).

We can consider these results of the simulation in the context of the double-well shaped potential between two neighboring tubulin dimers shown in Figure 3.1f. For the tubulins in direct contact with the AFM tip and their near neighbors, the F-I experiment corresponds to first pushing uphill within the tube potential well (labeled 1 in the upper panel of Figure 3.1f), which contributes to region 2 of the F-I curve, then crossing the barrier and falling to the sheet bond well (labeled 2 in the figure), which results in the gap, and pushing uphill again within the sheet bond well (labeled 3 in the figure), which contributes to region 3 of the curve (together with major contributions from other tube bonds). Eventually some tubulins break their lateral bonds completely (labeled 4 in the figure), leading to messy nonlinear responses (step 4). For those tubulins opposite to the tubulin-AFM tip contact site, the F-I experiment corresponds to first pushing uphill within the tube potential well along the 1' direction, and breaking the bond eventually (labeled 4' in the figure).

Given the uncertainties of model parameters, we performed sensitivity analysis for those parameters lacking precise experimental constraints. The upper panel of Figure 3.3a gives the dependence of the linear response slope of the F-I curve, k, on various parameters. The biggest changes of k of ± 25% occur when the two tube bond related parameters k_{st} or k_{rt} vary from half to 2 fold of the base values. The torsional energy and

sheet bond related spring constants have negligible effects on k. The results indicate that most of the contribution to the linear response comes from the tube bonds, which are the majority in the structure. On the other hand, the lower panel of Figure 3.3a shows that the gap position depends strongly on the tube shear constant k_{st} as well as on the sheet bond parameters k_{ss} and k_{rs}. We believe these results reflect the fact that in the L2 model the gap is due to tube-to-sheet bond conversion, and involves large relative lateral rotations between neighboring tubulins. The two-parameter analyses in Figure 3.3b-d further show that these parameters affect the MT mechanical properties cooperatively. Accurate experimental measurements may help constraining these parameters. Figure 3.3d shows the region of k_{st} and k_{rt} consistent with the observed gap position and the linear response slope.

Figure 3.4 shows comparison of the L1 and L2 models with varying AFM tip size. Consistent with the above results, the L2 model reproduces the gap of the F-I curve under a broad range of experimental conditions. Interestingly, the L1 model also gives recognizable gap under certain conditions (see Figure 3.4b&c). However, in this case only a short and barely recognizable quasi-linear region follows the gap before the structure-less nonlinear region. According to the L1 model, at the gap the PF pressed by the AFM tip breaks some lateral bonds with neighboring PFs without breaking any longitudinal bond (Figure 3.4d). This is a mechanism suggested by Schaap et al to explain the gap in their experimental curves. The process corresponds to pushing the single-well shaped potentials in the lower panel of Figure 3.1f up first (labeled 1 and 1' in the figure), then breaking the bonds (labeled 2 and 2' in the figure). However, this unzipping mechanism usually initializes breaking of additional lateral bonds, and the F-I

curve quickly enters the nonlinear region after a very short quasi-linear region. Figure 3.4e&f show that one can further distinguish the two models through measuring the F-I curves using AFM tips with different sizes. With the tip size increasing from 10 to 30 nm, the L1 model predicts that the gap position increases from ~ 4 nm to > 6 nm, while the L2 model predicts roughly unchanged gap position. With large sized tips (30-60 nm), the L2, but not the L1 model predicts noticeable gap width. Figure 3.4g shows that both models predict a nearly linear dependence of κ on the AFM tip size.

Suggested experiments to further constrain model parameters

As shown in Figure 3.3, accurate measurement of mechanical properties can be used to define MT model parameters. We present additional modeling studies using the L2 model that could be explored experimentally in the future. Figure 3.5a shows the energy state for a typical long MT with the AFM tip pressing on the middle of the MT wall. The non-zero energy changes on the MT wall are about ± 40 nm in distance from the tip center point at an indentation of 7.4 nm (which is just before the MT breaks). This indicates that the deformation of the MT can only propagate about 40 nm along one direction. This conclusion can also be drawn from Figure 3.5b. The F-I curves overlapped in the linear region for MT lengths > 80 nm, for both small and large AFM tips. More detailed analysis (Figure 3.5c) shows that the shorter the MT, the less resistance the response to the pressing AFM tip. For different AFM tip radius, the critical lengths at which boundary effects vanish are all around 80 nm. The AFM tip radius changes the response strength of the MT wall (Figure 3.5c&d). The larger the AFM tip,

the higher the effective spring constant κ. This effect is due to larger tips having a larger contact surface on MT wall and thus leading to more tubulin monomers being involved. Note that the change of κ (~0.04-0.09 N/m, Figure 3.5d) is small despite large R variation (2-60 nm). This result is consistent with experimental observations [66]. Figure 3.5e shows that the gap position Γ increases with the tip radius, but decreases with the MT length, and it plateaus at around 50 nm. Again, since a larger tip has a larger contact surface on MT wall, the force is resisted by more tubulin monomers. Therefore, the monomers tend to have smaller deformations per unit of indentation distance because of smaller force exerted on them. This effectively delays the transition from tube bond to sheet bond and therefore the gap positions Γ. Similarly, a shorter MT is less resistance, and its lateral bond transition takes longer.

Another set of simulations that could be tested experimentally is to change the position of the AFM tip by moving the tips across the MT (from protofilament to protofilament) (Fig. 3.S3) or along the MT longitudinal direction (along a single protofilament, Fig. 3.S3). MTs are polymers of α- and β-tubulin dimers polymerized head to tail into protofilaments, thirteen of which associate laterally making the cylinder. Therefore, the MT wall is not smooth but bumpy, both along the longitudinal (z) and lateral directions (x). We find that the “bumps” along the protofilaments do not make observable difference on both linear and quasi-linear responses, but the ones formed between protofilaments do have effects on both kinds of mechanical responses. The online supporting text provides detailed discussions.

The L2 model predicts metastable hybrid sheet structures with different curvatures during microtubule assembly

Figure 3.6a-d show several examples of structures obtained by minimizing the free energy of the L2 model. There are two structures available experimentally at medium resolution (12-8 Å): the ribbon polymer and the MT. We constrain the parameters of our L2 model by requiring it to reproduce the two structures. The ribbon structure shown in Figure 3.6a contains the correct alternative sheet and tube bonds between protofilaments. The sheet bond tends to bend out of plane, and the tube bond tends to bend into the plane, and the bending is not perpendicular to the PF axis. The overall structure is thus helical in nature (ribbon-like). The bending angle between monomers along each protofilament is ~3.5 degrees, consistent with the experimental value of of 3.2 ± 0.5 degrees [57]. The MT structure shown in Figure 3.6d is energetically the most stable structure. The F2 model also gives a number of additional structures (as that shown in Figure 3.6b), which we call “hybrid” because they are neither pure MT structure nor pure ribbon structure but a combination of some sheet bonds and some tube bonds. Such structures correspond to local minima of the free energy function. Increasing the content of tube bonds has a straightening effect in the structure. Therefore the presence of hybrid polymers could in principle explain the observed sheet intermediates during assembly, with the variable curvatures reflecting the amount of initial sheet bonds already converted to the tube bonds. To support this proposal, Figure 3.6c shows a polymer with one end closed into a tube, and another end still having the open structure with remnant sheet bonds. The results shown in Figure 3.6 indicate that the L2 model is consistent with the available structural information from cryo-EM of growing MTs. This is an initial and necessary test prior to further comparison with the previously described L1 model.

e. Discussions and Conclusions

To resolve still remaining issues concerning the dynamics of MT , and apparent discrepancies between experimental and model observations, we have performed coarse-grained modeling studies on the mechanical properties of two classes of competing models that assume either one or two types of lateral bonds between neighboring tubulins. The previously reported L1 model [48, 67] can explain a significant body of experimental observations. The L2 model analyzed in this work is an extension of the L1 model. Therefore it not only inherits most of the properties of the L1 model, but also can further reproduce additional experimental results not explainable by the latter.

Schaap et al. used AFM tip to press a microtubule laying on a glass slip. They measured the microtubule indentation as a function of the force exterted, and observed a gap in the F-I curve. The L2 model gives the observed gap over a broad range of parameter space and experimental conditions. In this model the gap arises from the tube-to-sheet bond conversion of a small number of tubulins being pushed by the AFM tip. The model also predicts that early assembled tubulin clusters can assume not only the MT and the ribbon polymer structure obtained by Wang and Nogales (REF), but a number of hybrid structures with various contents of the two types of lateral bonds. The latter may correspond to the sheet structures with variable curvatures and lengths observed by Chretien et al. [56]. On the other hand, the L1 model reproduces the gap only under a narrow range of experimental conditions. Furthermore, large structure ruptures usually follow the gap, in contradiction with the observed quasi-linear response region of the F-I curve following the gap. We made several additional experimentally

testable predictions on the MT mechanical properties. Our analysis indicates that one could further distinguish between the two models by measuring the F-I curves using different AFM tip sizes. The AFM experiment is closely related to the nonequilibrium single molecule pulling experiments widely used to study macromolecule properties {Liphardt, 2001 #965}. With more quantitative data, one can reconstruct the free energy profile and extract the exact value of free energy difference between the two types of lateral bonds using some reconstruction technique [69].

We want to emphasize that it is important to evaluate competing models against multiple but not single experiments. For an acceptable model, one should reproduce multiple experiments with a single set of parameters. For example, in a doublet structure present in axonemes at least one protofilament must interact with two other protofilaments simultaneously [61]. We suggest the doublet structure as an evidence for the existence of two types of lateral bonds *in vivo*. One might alternatively suggest that lateral tubulin interactions are flexible, as illustrated by the flat single-well potential in Figure 3.1f. Consequently, even with the L1 model one PF might accommodate two interacting PFs. However, the elastic mechanical property of a MT, as quantified in the AFM experiments as the slope of the linear response region, sets the limit to how flexible the interactions within a single potential well can be. The estimated flexibility makes the above mentioned alternative explanation to the doublet structure unfavorable. It is worth pointing out that, theoretically, the gap of the F-I curve may be also due to taxol dissociation induced by the AFM tip. We did not analyze this possibility here. One may evaluate this proposal by measuring the F-I curves with GMPCPP MTs.

In summary, while the existing experimental evidence is not conclusive, and thus some direct evidence is still necessary, our computational studies suggests that further analysis of the proposed L2 model is warranted. In this work we focused on the effect of the proposed new type of lateral bond on microtubule mechanical properties, and made several experimentally testable predictions. Many plus end tracking proteins preferentially bind to the growing plus end of a MT. For example, evidence shows that the EB1 protein can regulate the closure behavior from sheet to tube during the MT assembly process [70]. An alternative type of lateral interactions between protofilaments in growing MT ends would offer a landing pad for microtubule-interacting proteins distinct from the canonical lateral interactions in the body of the microtubules, which could be used for the distinct localization of these factors and as a powerful regulatory tool of microtubule dynamics. By understanding the properties of sheet bond, one can start a new direction of MT related drug design.

f. Acknowledgement

ZW and JX are supported by the Thomas F. Jeffress and Kate Miller Jeffress Memorial Trust.

g. References

1. Alberts, B., et al., *Molecular Biology of the Cell*. 4d ed2002, New York: Garland.
2. Howard, J., *Mechanics of Motor Proteins and the Cytoskeleton*. 1st ed2001, Sunderland, MA: Sinauer.
3. Desai, A. and T.J. Mitchison, *Microtubule polymerization dynamics.* Annu.Rev. Cell Dev. Biol., 1997. **13**: p. 83-117.
4. Akhmanova, A. and M.O. Steinmetz, *Tracking the ends: a dynamic protein network controls the fate of microtubule tips.* Nat Rev Mol Cell Biol, 2008. **9**(4): p. 309-322.
5. Etienne-Manneville, S., *From signaling pathways to microtubule dynamics: the key players.* Current Opinion in Cell Biology, 2010. **22**(1): p. 104-111.
6. Tukamoto, T., et al., *Huntington's disease gene product, huntingtin, associates with microtubules in vitro.* Mol. Brain Res., 1997. **51**(1-2): p. 8-14.
7. Drewes, G., A. Ebneth, and E.-M. Mandelkow, *MAPs, MARKs and microtubule dynamics.* Trends in Biochemical Sciences, 1998. **23**(8): p. 307-311.
8. Iqbal, K., et al., *Defective brain microtubule assembly in Alzheimer's disease.* The Lancet, 1986. **328**(8504): p. 421-426.
9. Forno, L.S., *Neuropathology of Parkinson's Disease.* J. Neuropathol Exp Neurol, 1996. **55**(4): p. 259-272.
10. Dauer, W. and S. Przedborski, *Parkinson's Disease: Mechanisms and Models.* Neuron, 2003. **39**(6): p. 889-909.
11. Fojo, T., ed. *The role of microtubules in cell biology, neurobiology, and oncology*. Cancer drug discovery and development, ed. B.A. Teicher2008, Humana Press. 587.

12. Ballatore, C., V.M.Y. Lee, and J.Q. Trojanowski, *Tau-mediated neurodegeneration in Alzheimer's disease and related disorders.* Nat Rev Neurosci, 2007. **8**(9): p. 663-672.
13. Skovronsky, D.M., V.M.Y. Lee, and J.Q. Trojanowski, *Neurodegenerative diseases: New concepts of pathogenesis and their therapeutic implications.* Annu Rev Pathol Mech Dis, 2006. **1**(1): p. 151-170.
14. Kurachi, M., M. Hoshi, and H. Tashiro, *Buckling of a single microtubule by optical trapping forces: Direct measurement of microtubule rigidity.* Cell Motility and the Cytoskeleton, 1995. **30**(3): p. 221-228.
15. Kurz, J.C. and R.C. Williams, Jr., *Microtubule-associated proteins and the flexibility of microtubules.* Biochemistry, 1995. **34**(41): p. 13374-80.
16. Chretien, D., H. Flyvbjerg, and S.D. Fuller, *Limited flexibility of the inter-protofilament bonds in microtubules assembled from pure tubulin.* Eur Biophys J, 1998. **27**(5): p. 490-500.
17. Odde, D.J., et al., *Microtubule bending and breaking in living fibroblast cells.* J Cell Sci, 1999. **112 (Pt 19)**: p. 3283-8.
18. Janosi, I.M., D. Chretien, and H. Flyvbjerg, *Structural microtubule cap: stability, catastrophe, rescue, and third state.* Biophys J, 2002. **83**(3): p. 1317-30.
19. Janson, M.E. and M. Dogterom, *A bending mode analysis for growing microtubules: evidence for a velocity-dependent rigidity.* Biophys J, 2004. **87**(4): p. 2723-36.
20. Needleman, D.J., et al., *Radial compression of microtubules and the mechanism of action of taxol and associated proteins.* Biophys J, 2005. **89**(5): p. 3410-23.
21. Wang, H.W. and E. Nogales, *Nucleotide-dependent bending flexibility of tubulin regulates microtubule assembly.* Nature, 2005. **435**(7044): p. 911-5.
22. Bathe, M., et al., *Cytoskeletal bundle bending, buckling, and stretching behavior.* arXiv.org, 2006. **arXiv:q-bio/0607040v2**.

23. Li, C., C.Q. Ru, and A. Mioduchowski, *Torsion of the central pair microtubules in eukaryotic flagella due to bending-driven lateral buckling.* Biochemical and Biophysical Research Communications, 2006. **351**(1): p. 159-164.
24. van den Heuvel, M.G., M.P. de Graaff, and C. Dekker, *Molecular sorting by electrical steering of microtubules in kinesin-coated channels.* Science, 2006. **312**(5775): p. 910-4.
25. Brangwynne, C.P., F.C. MacKintosh, and D.A. Weitz, *Force fluctuations and polymerization dynamics of intracellular microtubules.* Proc Natl Acad Sci U S A, 2007. **104**(41): p. 16128-33.
26. Heussinger, C., M. Bathe, and E. Frey, *Statistical mechanics of semiflexible bundles of wormlike polymer chains.* Phys Rev Lett, 2007. **99**(4): p. 048101.
27. Munson, K.M., P.G. Mulugeta, and Z.J. Donhauser, *Enhanced Mechanical Stability of Microtubules Polymerized with a Slowly Hydrolyzable Nucleotide Analogue.* The Journal of Physical Chemistry B, 2007. **111**(19): p. 5053-5057.
28. Sept, D. and F.C. MacKintosh, *Microtubule elasticity: connecting all-atom simulations with continuum mechanics.* Phys Rev Lett, 2010. **104**(1): p. 018101.
29. Kikumoto, M., et al., *Flexural Rigidity of Individual Microtubules Measured by a Buckling Force with Optical Traps.* Biophysical Journal, 2006. **90**(5): p. 1687-1696.
30. Venier, P., et al., *Analysis of microtubule rigidity using hydrodynamic flow and thermal fluctuations [published erratum appears in J Biol Chem 1995 Jul 14;270(28):17056].* Journal of Biological Chemistry, 1994. **269**(18): p. 13353-13360.
31. Felgner, H., R. Frank, and M. Schliwa, *Flexural rigidity of microtubules measured with the use of optical tweezers.* Journal of Cell Science, 1996. **109**(2): p. 509-516.

32. Mickey, B. and J. Howard, *Rigidity of microtubules is increased by stabilizing agents.* The Journal of Cell Biology, 1995. **130**(4): p. 909-917.
33. Cassimeris, L., et al., *XMAP215 is a long thin molecule that does not increase microtubule stiffness.* Journal of Cell Science, 2001. **114**(16): p. 3025-3033.
34. Pampaloni, F., et al., *Thermal fluctuations of grafted microtubules provide evidence of a length-dependent persistence length.* Proc Natl Acad Sci U S A, 2006. **103**(27): p. 10248-53.
35. Van den Heuvel, M.G., M.P. de Graaff, and C. Dekker, *Microtubule curvatures under perpendicular electric forces reveal a low persistence length.* Proc Natl Acad Sci U S A, 2008. **105**(23): p. 7941-6.
36. Bayley, P., M. Schilstra, and S. Martin, *Microtubule dynamic instability: numerical simulation of microtubule transition properties using a Lateral Cap model.* J Cell Sci, 1990. **95**(1): p. 33-48.
37. Buxbaum, R.E. and S.R. Heidemann, *A thermodynamic model for force integration and microtubule assembly during axonal elongation.* J. Theor. Biol., 1988. **134**(3): p. 379-390.
38. Erickson, H.P. and D. Pantaloni, *The role of subunit entropy in cooperative assembly. Nucleation of microtubules and other two-dimensional polymers.* Biophys. J., 1981. **34**(2): p. 293-309.
39. Gardner, M.K., et al., *Microtubule assembly dynamics: new insights at the nanoscale.* Curr. Op. Cell Biol., 2008. **20**(1): p. 64-70.
40. Hill, T.L., *Microfilament or microtubule assembly or disassembly against a force.* Proc Natl Acad Sci U S A, 1981. **78**(9): p. 5613-7.
41. Jánosi, I.M., D. Chrétien, and H. Flyvbjerg, *Modeling elastic properties of microtubule tips and walls.* Eur. Biophys. J, 1998. **27**(5): p. 501-513.
42. Kolomeisky, A.B. and M.E. Fisher, *The growth of microtubules against an external force.* Biophys. J., 2001. **80**(1): p. 514a-514a.

43. Kolomeisky, A.B. and M.E. Fisher, *Force-velocity relation for growing microtubules.* Biophys. J., 2001. **80**(1): p. 149-154.

44. Mogilner, A. and G. Oster, *The polymerization ratchet model explains the force-velocity relation for growing microtubules.* Eur. Biophys. J, 1999. **28**(3): p. 235-242.

45. Sept, D., N.A. Baker, and J.A. McCammon, *The physical basis of microtubule structure and stability.* Protein Sci, 2003. **12**(10): p. 2257-61.

46. van Doorn, G.S., et al., *On the stall force for growing microtubules.* Eur. Biophys. J, 2000. **29**(1): p. 2-6.

47. Zong, C., et al., *Nonequilibrium self-assembly of linear fibers: microscopic treatment of growth, decay, catastrophe and rescue.* Phys. Biol., 2006. **3**(1): p. 83.

48. VanBuren, V., L. Cassimeris, and D.J. Odde, *Mechanochemical model of microtubule structure and self-assembly kinetics.* Biophys J, 2005. **89**(5): p. 2911-26.

49. Molodtsov, M.I., et al., *Force production by depolymerizing microtubules: a theoretical study.* Proc Natl Acad Sci U S A, 2005. **102**(12): p. 4353-8.

50. Summers, K. and M.W. Kirschner, *Characteristics of the polar assembly and disassembly of microtubules observed in vitro by darkfield light microscopy.* J. Cell Biol., 1979. **83**(1): p. 205-217.

51. Bergen, L.G. and G.G. Borisy, *Head-to-tail polymerization of microtubules in vitro. Electron microscope analysis of seeded assembly.* J. Cell Biol., 1980. **84**(1): p. 141-150.

52. Erickson, H.P., *Microtubule surface lattice amd subunit structure and observations on reassembly.* J. Cell Biol., 1974. **60**(1): p. 153-167.

53. Detrich, H.W., et al., *Mechanism of microtubule assembly. Changes in polymer structure and organization during assembly of sea urchin egg tubulin.* J. Biol. Chem., 1985. **260**(16): p. 9479-9490.

54. Simon, J. and E. Salmon, *The structure of microtubule ends during the elongation and shortening phases of dynamic instability examined by negative-stain electron microscopy.* J Cell Sci, 1990. **96**(4): p. 571-582.

55. Kirschner, M.W., L.S. Honig, and R.C. Williams, *Quantitative electron microscopy of microtubule assembly in vitro.* J. Mol. Biol., 1975. **99**(2): p. 263-276.

56. Chretien, D., S.D. Fuller, and E. Karsenti, *Structure of growing microtubule ends: two-dimensional sheets close into tubes at variable rates.* J Cell Biol, 1995. **129**(5): p. 1311-28.

57. Wang, H.W., et al., *Assembly of GMPCPP-bound tubulin into helical ribbons and tubes and effect of colchicine.* Cell Cycle, 2005. **4**(9): p. 1157-60.

58. Wu, Z., et al., *Simulations of Tubulin Sheet Polymers as Possible Structural Intermediates in Microtubule Assembly.* PLoS ONE, 2009. **4**(10): p. e7291.

59. VanBuren, V., D.J. Odde, and L. Cassimeris, *Estimates of lateral and longitudinal bond energies within the microtubule lattice.* Proc Natl Acad Sci U S A, 2002. **99**(9): p. 6035-40.

60. Nogales, E. and H.W. Wang, *Structural intermediates in microtubule assembly and disassembly: how and why?* Curr. Op. Cell Biol., 2006. **18**(2): p. 179-184.

61. Sui, H. and K.H. Downing, *Molecular architecture of axonemal microtubule doublets revealed by cryo-electron tomography.* Nature, 2006. **442**(7101): p. 475-478.

62. Fygenson, D., D. Needleman, and K. Sneppen, *Variability-based sequence alignment identifies residues responsible for functional differences in α and β tubulin.* Protein Sci., 2004. **13**(1): p. 25-31.

63. Waterman-Storer, C.M. and E.D. Salmon, *Actomyosin-based Retrograde Flow of Microtubules in the Lamella of Migrating Epithelial Cells Influences Microtubule Dynamic Instability and Turnover and Is Associated with Microtubule Breakage and Treadmilling.* J. Cell Biol., 1997. **139**(2): p. 417-434.
64. Sui, H. and K.H. Downing, *Structural basis of interprotofilament interaction and lateral deformation of microtubules.* Structure, 2010. **18**(8): p. 1022-31.
65. de Pablo, P.J., et al., *Deformation and collapse of microtubules on the nanometer scale.* Phys Rev Lett, 2003. **91**(9): p. 098101.
66. Schaap, I.A., et al., *Elastic response, buckling, and instability of microtubules under radial indentation.* Biophys J, 2006. **91**(4): p. 1521-31.
67. Molodtsov, M.I., et al., *A molecular-mechanical model of the microtubule.* Biophys J, 2005. **88**(5): p. 3167-79.
68. Press, W.H., *Numerical Recipes in C : The Art of Scientific Computing*. 2nd , rev. ed1997, Cambridge Cambridgeshire ; New York: Cambridge University Press. xxvi, 994.
69. Hummer, G. and A. Szabo, *Free energy reconstruction from nonequilibrium single-molecule pulling experiments.* Proceedings of the National Academy of Sciences of the United States of America, 2001. **98**(7): p. 3658-3661.
70. Vitre, B., et al., *EB1 regulates microtubule dynamics and tubulin sheet closure in vitro.* Nat Cell Biol, 2008. **10**(4): p. 415-421.
71. Caplow, M. and J. Shanks, *Evidence that a single monolayer tubulin-GTP cap is both necessary and sufficient to stabilize microtubules.* Molecular Biology of the Cell, 1996. **7**(4): p. 663-675.
72. Kis, A., et al., *Nanomechanics of Microtubules.* Physical Review Letters, 2002. **89**(24): p. 248101.
73. Kasas, S., et al., *Mechanical Properties of Microtubules Explored Using the Finite Elements Method.* Chemphyschem, 2004. **5**(2): p. 252-257.

parameter	Physical interpretation	Value	Estimation method and reference
k_{long}	Spring constant for longitudinal stretching	1.32 $GPa \cdot nm$	[48] [14, 15, 19, 29-35] [65, 66]
k_{lmd}	Spring const. long. Bending	$34\ k_B T/dimer \cdot rad^2$	[48, 71]
$k_{torsion}$	Spring const. long. Torsion	$10\ k_B T/dimer \cdot rad^2$	Model based
k_{lat}	Spring const. lateral stretching	0.8 $GPa \cdot nm$	[48] [14, 15, 19, 29-35] [65, 66]
k_{st}	Spring const. lateral shearing for tube bond	$116\ k_B T/dimer$	[28] [72, 73]
k_{ss}	Spring const. lat. shearing for sheet bond	$10 k_B T/dimer$	Model based
k_{rt}	Spring const. lat. rotation for tube bond	$50\ k_B T/dimer \cdot rad^2$	Model based
k_{rs}	Spring const. lateral rotation for sheet bond	$10\ k_B T/dimer \cdot rad^2$	Model based
ΔG_{long}^{o}	Standard free energy change for longitudinal interaction (immobilizing free energy not counted)	$-20\ k_B T$	[45, 59]
ΔG_{lat}^{o}	Standard free energy change for lateral interaction	Tube bond: -5 $k_B T$	[45, 58, 59]

		Sheet bond: -3 k_BT	

*. All parameters are base values and the details on how to get the values can be found in online supporting information. The different values used in the model estimations are specified in the main text.

Table 3.1 model parameters

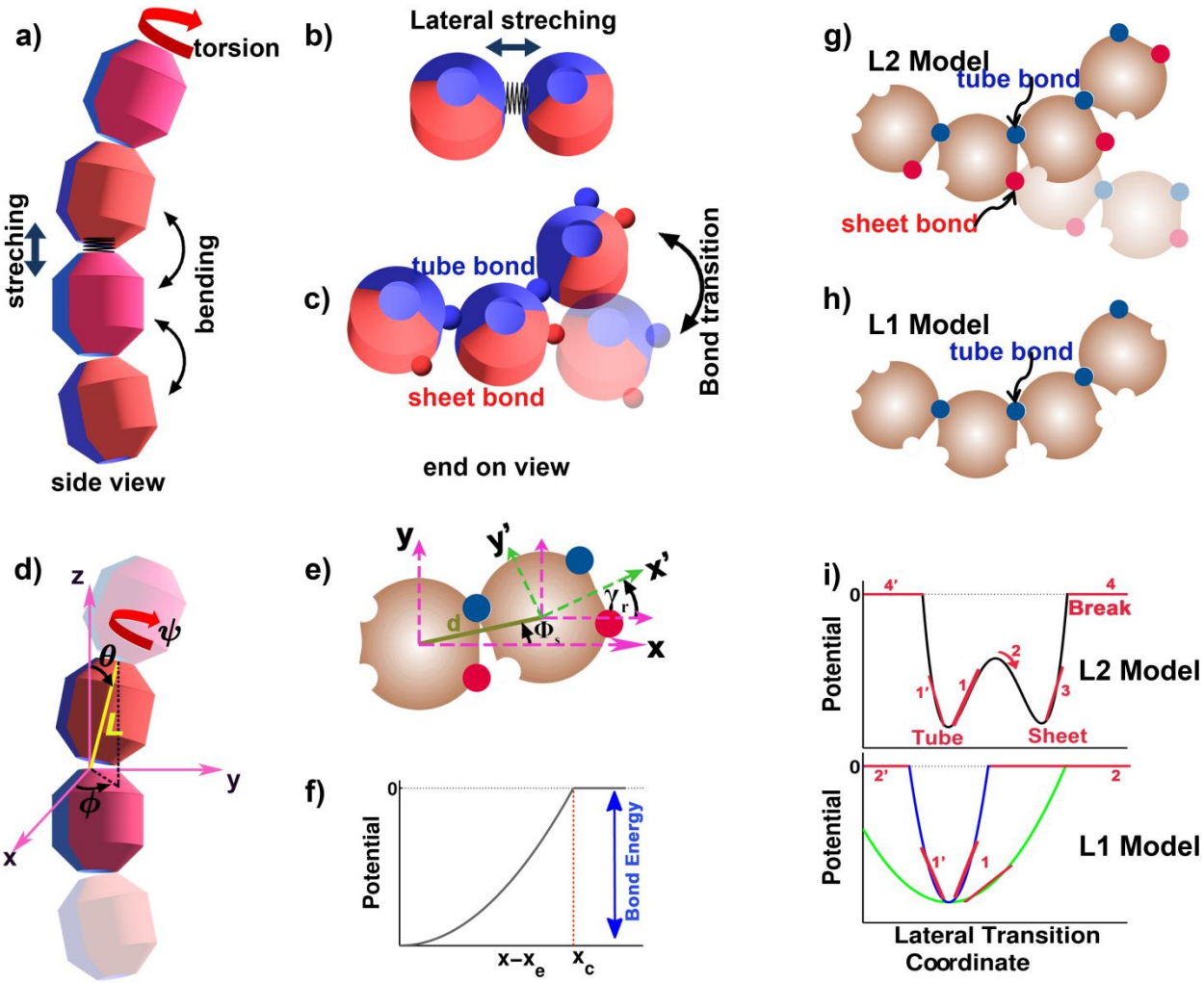

Figure 3.1 Schematic representation of the L1 and L2 models. (a) Basic modes of motion related to longitudinal interactions: inter-dimer stretching, intra- and inter-dimer bending, and inter-dimer torsional motion. (b) Basic modes of motions related to lateral interactions: stretching, translational shift, and torsion. (c) Conversion between two types of lateral bonds resulted from combinations of the lateral modes. (d) Four coordinates (r, θ, ϕ, ψ) describe the relative position and orientation between two neighboring monomers. Each monomer is treated as a rigid body and they are connected head to tail along the longitudinal direction. All energy terms are expressed as functions of these four coordinates. (e) The relative coordinates (d, Φ_s, γ_r), which describe the relative position and orientation between two lateral neighboring

monomers, represent the distance and the translational angle between the centers of mass of two monomers, and the reorientation of the monomer internal coordinate system, respectively. These values are derived from the four coordinates in (b). (f) Schematic illustration of the truncated harmonic potential form used, with x_e stands for the equilibrium value in the corresponding dimension, and x_c the critical value where the interaction becomes zero. (g-h) Schematic comparison between the L2 and L1 models. The former generalizes the latter by adding one more type of lateral interaction (sheet bond in red) besides the traditional tube bond (in blue). (i) Schematic llustration of the composite double-well (for the L2 model) and single well (for the L1 model) potentials along the lateral bond conversion coordinate. The blue and green curves for the L1 model correspond to stiff and soft tube bonds, respectively.

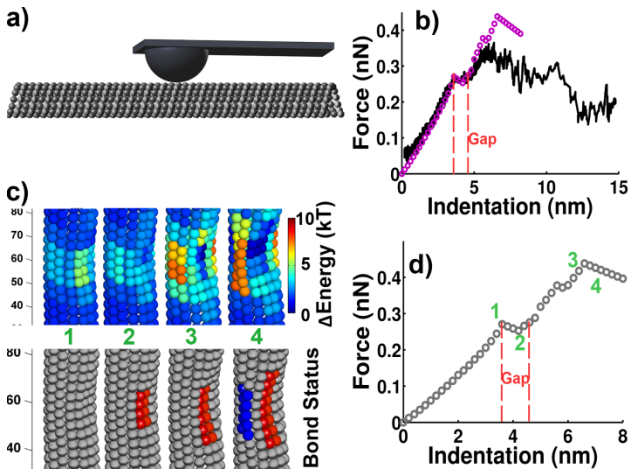

Figure 3.2 - Simulated results for an AFM tip pushing against the microtubule wall using the L2 model. (a) Schematic illustration of the experimental setup with the tip size corresponding to 25 nm. (b) Experimental force-indentation curve (black line) adapted from [66] and the simulated results (puple circles). The black line is averaged over twenty-four indentation curves from five different experiments. The red dashed lines indicate the gap region between two linear segments and well before the non-linear response. (c) Sections of the simulated MT

conformations under the press of the AFM tip shown at different indentation positions (as numbered in (d)). Upper panel shows local energy plots. Lower panel shows bond type plots: tube bond is gray, sheet bond is red, and blue indicates the break of the lateral bond between adjacent tubulins. (d) Simulated F-I curve with a ~120 nm MT and a tip with radius = 25 nm consistent with the experiment. The red dashed lines indicate a gap similar to that shown in (b) Fitting the first linear region gives a slope ~0.07 N/m, as compared to the experimental slope of ~ 0.074 ± 17% N/m. All mechanical and energetic values involved are listed in Table 3.1 unless otherwise indicated.

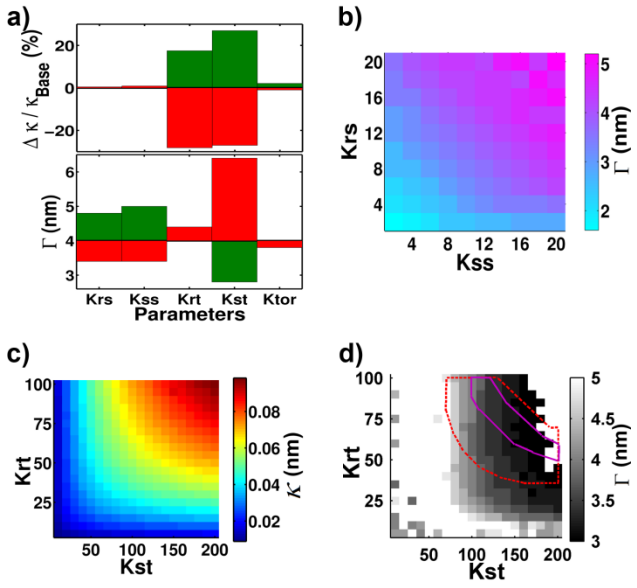

Figure 3.3 - Sensitivity analysis and estimation of the L2 model parameters. (a) Dependence of the slope of the linear force-indentation curve region (κ), and the gap starting position (Γ) on various model parameters , while keeping all others at their base values listed in Table 3.1. For each parameter, the graphs shows relative changes in κ from those for k_{base} to values of $0.5k_{base}$ (red bars) and $2k_{base}$ (green bars). (b) Two-dimensional contour plot of Γ dependence on k_{ss} (in units of k_BT/dimer) and k_{rs} (in units of k_BT/dimer/rad^2), with all other

parameters at base values. (c) Two-dimensional contour plot of κ dependence on k_{st} (in units of k_BT/dimer) and k_{rt} (in units of k_BT/dimer/rad^2). (d) Two-dimensional contour plot of Γ dependence on k_{st} and k_{rt}. The blank area indicates $\Gamma>5$ nm, $\Gamma<3$ nm or no recognizable gap. The region enclosed by dashed lines gives $\kappa=[0.05,0.085]$ N/m, and the region enclosed by the solid line gives $\kappa=[0.07,0.08]$ N/m.

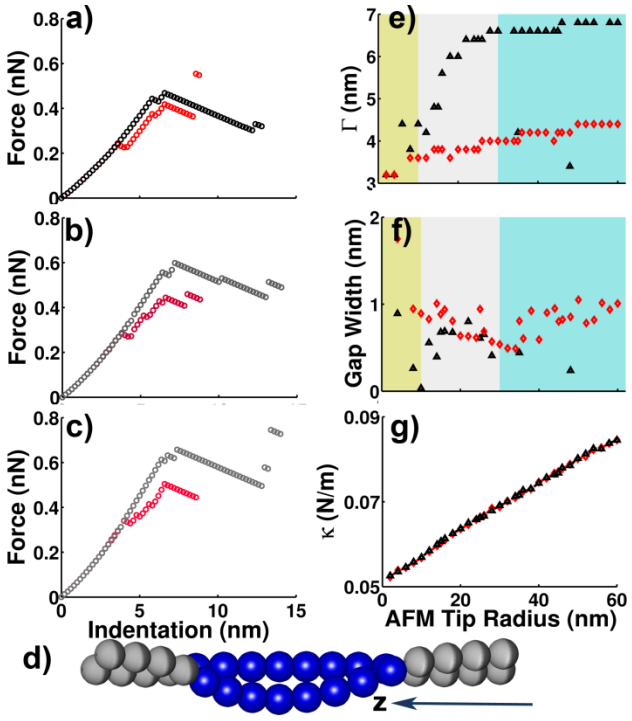

Figure 3.4 - Comparison between the L1 (black triangle) and L2 (red diamond) models. (a-c) The F-I curve with AFM tip Radius = 10, 20 and 30 nm, respectively. (d) The unzipping mechanism for the L1 model to generate the gap. The lateral bonds between blue colored tubulins are broken. (e-f) The gap position Γ and width as a function of the AFM tip radius *R*. Yellow region: *R* = 0 ~ 10 nm; gray region: *R* = 10 ~ 30 nm; blue region: *R* = 30~60 nm. Missing points correspond to no recognizable gap. (g) Calculated slope of the linear region of the F-I

curve κ versus the AFM tip Radius. All simulations are performed with MT Length = ~ 120 nm, and parameters listed in Table 3.1 unless otherwise stated.

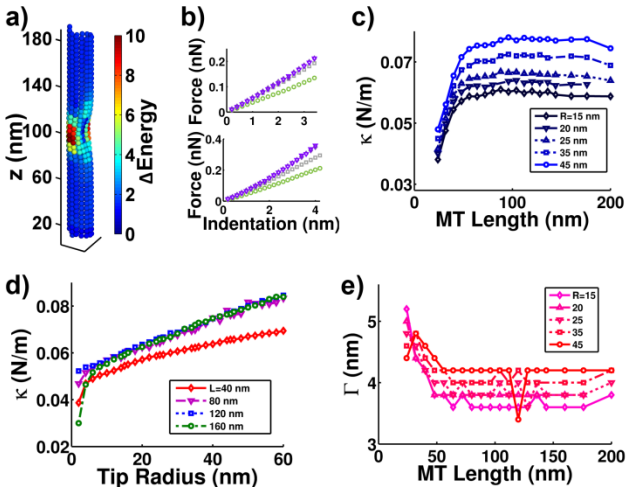

Figure 3.5 Effects of MT length on mechanical properties in the linear region. (a) One conformation of a 200 nm MT with energy plot under AFM tip pressed at indentation distance of 7.4 nm. Both the MT physical deformation and the energy changes indicate that the effects of AFM tip can only be seen between z = 60 ~ 140 nm, which is about 80 nm region of MT. (b) The F-I curve with Tip Radius = 15 nm (upper panel) and 45 nm (lower panel), and MT length ~24 (circle), 40 (square), 80 (diamond) and 160 (triangle) nm, respectively. (c) Calculated κ versus MT length with AFM tip radius R = 15, 20, 25, 35, and 45 nm. (d) Calculated κ versus tip radius R with MT length = ~ 40, 80, 120, and 160 nm. (e) The gap starting position Γ versus MT length at AFM Tip radius R = 15, 20, 25, 35, and 45 nm.

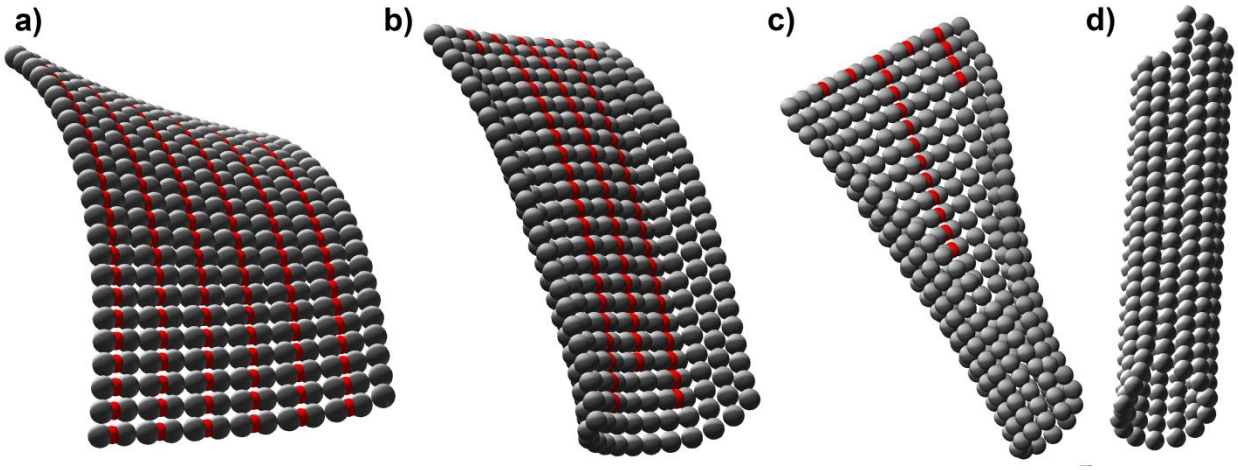

Figure 3.6 - Typical tubulin polymer structures obtained through local free energy minimization of the L2 model. In this figure, a tubulin colored in red indicates that it is forming a sheet bond with its left neighboring tubulin. (a) Ribbon structure with the two types of lateral bonds alternating between neighboring PFs. (b-c) Hybrid structures with less regular distribution of the lateral bonds. (d) Canonical MT structure.

h. Supplemental Text

Supplemental Methods

As discussed in the main text, we use a coarse-grained modeling framework that treats α and β tubulin monomers as rigid bodies (rods) connected by elastic springs. Moreover, we assume that the monomers are chained together along longitudinal direction in each protofilament. This assumption is consistent with the model of VanBuren et al. However, in our case a monomer is represented more than just a vector as in the work of VanBuren et al, but can rotate along the long axis of the rod to account

for heterogeneous lateral interactions between tubulins. To describe the behavior of the microtubules, we first need to define the spatial position and orientation of each monomer. In general a rigid body has 6 degrees of freedom to specify its position and orientation. However, the connected rod model restrains the number of degrees of freedom. For convenience of mathematical formulation of the model, we use two sets of coordinate frame. Each tubulin monomer is treated as a three-dimensional rigid body, and thus has an intrinsic coordinate frame. Therefore one can specify the spatial and orientational coordinates of a monomer by comparing its intrinsic coordinate frame with the laboratory fixed frame, or with the intrinsic frame of the previous monomer on the same protofilament. Below explains the procedure in detail.

For the *j*-th protofilament, one first needs 3 coordinates ($x_{0,j}$, $y_{0,j}$, $z_{0,j}$) in the laboratory frame to specify the spatial coordinate of the minus end of the first α-tubulin relative to the laboratory frame. Then the spatial coordinate of the plus end of the α-tubulin is given by ($x_{1,j}$, $y_{1,j}$, $z_{1,j}$). One also needs another coordinate $\psi^{L}_{1,j}$ to describe the rotation along the long rod axis relative to the laboratory frame. Alternatively, one can use the relative coordinates ($L_{1,j}$, $\theta_{1,j}$, $\varphi_{1,j}$, $\psi_{1,j}$), where $L_{1,j}$ is the modulus of the vector $\boldsymbol{r}_{1,j} = (x_{1,j} - x_{0,j}, y_{1,j} - y_{0,j}, z_{1,j} - z_{0,j})$, and ($\theta_{1,j}$, $\varphi_{1,j}$, $\psi_{1,j}$) are a set of angles defined in Figure 3.1d of the main text to determine the orientation of the monomer respect to the previous monomer—the laboratory frame in this case. The next tubulin monomer, a -tubulin, starts its minus end at ($x_{1,j}$, $y_{1,j}$, $z_{1,j}$), and can be similarly described by a set of relative coordinates ($L_{2,j}$, $\theta_{2,j}$, $\varphi_{2,j}$, $\psi_{2,j}$). The remaining monomers can be described in a similar way. The transformation between the coordinates in the laboratory frame, $(x_{i,j}, y_{i,j}, z_{i,j}, \psi^{L}_{i,j})$, and the relative coordinates ($L_{i,j}$, $\theta_{i,j}$, $\varphi_{i,j}$, $\psi_{i,j}$) is given by

$$
\begin{aligned}
x_{i,j} &= x_{i-1,j} + L_{i,j}\sin\theta_{i,j}\cos\phi_{i,j},\\
y_{i,j} &= y_{i-1,j} + L_{i,j}\sin\theta_{i,j}\sin\phi_{i,j},\\
z_{i,j} &= z_{i-1,j} + L_{i,j}\cos\theta_{i,j},\\
\psi^{L}_{i,j} &= \psi^{L}_{i-1,j} + \psi_{i,j}.
\end{aligned}
\tag{1}
$$

and for the inverse transformation,

$$
\begin{aligned}
L^2_{i,j} &= (x_{i,j} - x_{i-1,j})^2 + (y_{i,j} - y_{i-1,j})^2 + (z_{i,j} - z_{i-1,j})^2\\
\theta_{i,j} &= \arccos((z_{i,j} - z_{i-1,j}) / L_{i,j})\\
\phi_{i,j} &= \begin{cases} \arcsin((y_{i,j} - y_{i-1,j}) / L2), \text{ if } 0 \le x_{i,j} - x_{i-1,j}; \\ \pi - \arcsin((y_{i,j} - y_{i-1,j}) / L2), \text{ if } x_{i,j} - x_{i-1,j} < 0. \end{cases}\\
\psi_{i,j} &= \psi^{L}_{i,j} - \psi^{L}_{i-1,j}.
\end{aligned}
\tag{2}
$$

where $L2^2 = (x_{i,j} - x_{i-1,j})^2 + (y_{i,j} - y_{i-1,j})^2$. The energy terms are functions of the relative coordinates between monomers. Following VanBuren et al. (1), an auxiliary coordinate Φ is also introduced to describe deviation of the bending angle between the (i-1)-th and i-th monomers within the j-th protofilament from the preferred value,

$$
\Phi_{i,j} = \arccos(l_{i-1,j}l_{i,j} + m_{i-1,j}m_{i,j} + n_{i-1,j}n_{i,j}),
\tag{3}
$$

where the terms *l, m,* and *n* are the direction cosines given by

$$
l_{i,j} = \frac{x_{i,j} - x_{i-1,j}}{L_{i,j}}, m_{i,j} = \frac{y_{i,j} - y_{i-1,j}}{L_{i,j}}, n_{i,j} = \frac{z_{i,j} - z_{i-1,j}}{L_{i,j}}.
\tag{4}
$$

Once defining the position of the monomers through longitudinal interactions, one can then derive the quantities which describe the lateral interaction. Two quantities describe the lateral relations between 2 monomer (*i', j-1*) and (*i, j*),: the distance between two monomers d_{ij}, the shift angle between two monomers Φ_s , and the rotational angle γ_r (see Figure 3.1e in the main text). The term *d* is defined as

$$d_{i,j} = \left\| \mathbf{r}_{i,j} - \mathbf{r}_{i',j-1} \right\| \\ = ((x^c_{i,j} - x^c_{i',j-1})^2 + (y^c_{i,j} - y^c_{i',j-1})^2 + (z^c_{i,j} - z^c_{i',j-1})^2)^{1/2}. \quad (5)$$

Where $x^c_{i,j} = \frac{x_{i,j} + x_{i-1,j}}{2}$ and the others have the similar definitions. The shift and rotational angles Φ_s and γ_r are defined also from the global coordinates.

$$\Phi_s^{i,j} = \arccos(l^{lat}{}_{i,j} l^{lat}{}_{i,j-1} + m^{lat}{}_{i,j} m^{lat}{}_{i,j-1} + n^{lat}{}_{i,j} n^{lat}{}_{i,j-1}), \\ \gamma_r^{i,j} = \psi^L_{i,j} - \psi^L_{i,j-1}. \quad (6)$$

where the definitions of l^{lat}, m^{lat}, and n^{lat} are similar to those in (4) except that L_{ij} is replaced by d_{ij}. The details can be understood from Figure 3.1 in the main text and Figure 3.S5. These relative coordinates can be used to define the energy terms.

Energy terms and parameter estimations:

From the Young's Modulus measurements of MT and the second moment of inertia, one can derive the values of k_{long} and k_{lat} (1). The Yong's Modulus can be determined based on the rigidity EI. Table S1 summarizes some of the experimental results (2-11). The measured rigidity of MT has a very wide range, so as for Young's Modulus. Binding of microtubule associated proteins may contribute to the diversity. In our studies we use data from (12, 13) which are measured under similar experimental conditions we are simulating. Furthermore, we find that most of the spring constants are sluggish to the problems we are addressing (see Figure 3.3). Specifically, the Young's Modulus *E* can be derived from

$$
\begin{aligned}
E &= \frac{EI}{I} \\
I &= \frac{\pi}{4}(r_{outer}^4 - r_{inner}^4) \\
r_{inner} &= 8.4 \text{ nm} \\
r_{outter} &= r_{inner} + d_t
\end{aligned}
\tag{7}
$$

Choosing an effective thickness of MT wall d_t =1.54 nm (12), one has

$$
I = \frac{\pi}{4}(r_{outer}^4 - r_{inner}^4) = 8.012 \times 10^{-33} \text{m}^4 \tag{8}
$$

$$
E = \frac{EI}{I} = \begin{cases} \dfrac{1 \sim 2.5 \times 10^{-24} \text{Nm}^2}{3.757 \times 10^{-33} \text{m}^4} \\ \dfrac{3 \sim 9 \times 10^{-24} \text{Nm}^2}{3.757 \times 10^{-33} \text{m}^4} \end{cases} = \begin{cases} 0.266 \sim 0.665 \times 10^9 \text{ N/m}^2 & \text{Taxol MT} \\ 0.799 \sim 2.396 \times 10^9 \text{ N/m}^2 & \text{Pure MT} \end{cases} \tag{9}
$$

In this work the Young's Modulus is chosen to be 0.665GPa (for Taxol MT) to be consistent with most of the experiments especially AFM experiments (12, 13).

The spring constant related to a given Young's Modulus can then be derived from

$$
k = \frac{EA}{L_0}. \tag{10}
$$

where *A* is the cross section area perpendicular to the direction of force, L_0 is the original length along the direction of force. In our case, they are cross section of longitudinal/lateral interaction and length/width of monomer, respectively. The size of monomer is 5.15 nm x 4 nm x 1.54 nm (12). Therefore, one can determine the values of k_{long} and k_{lat},

$$k_{lat} = \frac{0.665\ \text{GPa} \times (4\text{nm} \times 1.54\text{nm})}{5.15\text{nm}} = 0.795417\ \text{GPa} \cdot \text{nm} \tag{11}$$

$$k_{long} = \frac{0.665\ \text{GPa} \times (5.15 \times 1.54)}{4} = 1.31853\ \text{GPa} \cdot \text{nm} \tag{12}$$

or, in the unit of k_BT (at T = 300 K).

$$\begin{aligned} k_{lat} &= 0.795417\ \text{GPa} \cdot \text{nm} \\ &= 96.73 \frac{k_B T}{\text{dimer} \cdot nm^2} \end{aligned} \tag{13}$$

$$\begin{aligned} k_{long} &= 1.31853\ \ \text{GPa} \cdot \text{nm} \\ &= 160.347 \frac{k_B T}{\text{dimer} \cdot nm^2} \end{aligned} \tag{14}$$

The bending spring constant can be determined by this way: the energy stored in the bending dimer is 2.5~3 k_BT (1, 14). One can then use

$$E_{bend} = \frac{1}{2} \kappa_{bend} \Phi^2 \tag{15}$$

to determine the bending constant. The maximum bending angle is ~22^0 (0.384 rad)(15). One then has

$$k_{bend} = \frac{2.5\ \text{k}_\text{B}\text{T/dimer} \times 2}{(0.384\ \text{rad})^2} = 34 \frac{\text{k}_\text{B}\text{T}}{\text{dimer} \cdot\ \text{rad}^2} \tag{16}$$

The shear modulus is estimated to be 48 MPa from (16) (MD) and 1.4+/-0.4MPa from (17, 18) (AFM Exp), while other works give an even larger range of suggestion of shear modulus from 1Kpa to 100Mpa. The shift energy has the form

$$E_{\text{shift}} = \frac{3Lh}{2p} Gx^2 = \frac{3Lh}{2p} Gp^2 \tan^2 \Phi_s = \frac{3Lph}{2} G \tan^2 \Phi_s = \frac{1}{2} k_{shift} \tan^2 \Phi_s \qquad (17)$$

Therefore

$$k_{\text{shift\_tube}} = 3LphG \qquad (18)$$

where *G* is the shear modulus (we use 10 MPa in our simulation), *L* is the length of a monomer (4 nm), *p* is the effective width between lateral monomers (5.15 nm), *h* is the effective thickness of the MT wall (1.54 nm). The value of k_{shift_tube} of tube bond is

$$\begin{aligned} k_{shift\_Tube} &= 3 \times 4nm \times 5.15nm \times 1.54nm \times 0.01GPa \\ &= 115.75 \frac{k_B T}{\text{dimer}} \end{aligned} \qquad (19)$$

For *G* being 1MPa - 50Mpa, the corresponding k_{shift_tube} is 11 ~ 580 k_BT/dimer.

No experimental data exists to estimate the value of k_{shift} for the sheet bond, so we examined the effect of changing the value within the range k_{shift_sheet} = 10 ~ 100 k_BT/dimer (see Figure3 In the main text). For simplicity, we assume the shear properties for each monomer are symmetric through longitudinal and lateral direction.

Experimental information of the torsion energy for longitudinal interactions and rotational energy for lateral interactions is also absent. These energy terms are closely related because rotation of a monomer changes torsion of the PF directly. We also examined values of these terms within a range (see Figure3 in the main text). Based on the data fitting of both AFM experiments and structure information from (19), one set of value of the spring constants for these two energy terms are

$$k_{tor} = 10\frac{\mathrm{k}_B\mathrm{T}}{\mathrm{dimer}\cdot\mathrm{rad}^2} \tag{20}$$

$$\begin{aligned} k_{rot\_sheet} &= 10\frac{\mathrm{k}_B\mathrm{T}}{\mathrm{dimer}\cdot\mathrm{rad}^2} \\ k_{rot\_tube} &= 50\frac{\mathrm{k}_B\mathrm{T}}{\mathrm{dimer}\cdot\mathrm{rad}^2} \end{aligned} \tag{21}$$

Bilinear gap analysis:

The "gap" from force-indentation (F-I) curves can be characterized with two quantities: the kink position Γ and the gap width d_{gap}. The gap separates the quasilinear response into two regions before crashing the microtubule. Figure 3.S2 schematically shows the method to calculate these two quantities. The kink position is defined as the first positions where the stepping behavior happens. The gap width is defined as the width when the second linear region starts to catch up the height of the first linear region.

The F-I curve is generated from simulations as follows. At each step the AFM cantilever position changes from ($z_{AFM} - \Delta z_{AFM}$) to z_{AFM}. Correspondingly the microtubule wall changes its position from ($z_{MT} - \Delta z_{MT}$) to z_{MT}. The definition of z_{AFM} and z_{MT} are defined as the change of position of cantilever and MT wall, respectively. More details can be found from Figure 3.S6. Notice that the AFM cantilever is elastic (with spring constant of 0.03N/m as in (12)), so in general $\Delta z_{AFM} \neq \Delta z_{MT}$. Therefore, the AFM cantilever deformation is given by $z_S = z_{AFM} - z_{MT}$. During each step of AFM tip movement the minimal work done by the AFM is given by the potential energy changes *U* at the MT wall positions z_{MT} and the energy stored in the cantilever deformation (which is treated as a linear spring with spring constant k_s=0.03 N/m). Then one has

$$W = \int_0^{z_{AFM}} F(z_{AFM})\, dz_{AFM} = \frac{1}{2} k_s z_s^2 + (U_{z_{MT}} - U_{z_{MT}=0}) \quad (22)$$

Note that we have $z_S = z_{AFM} - z_{MT}$, at equilibrium status, we may have $F = k_S z_S = \frac{\partial(U(z_{MT}))}{\partial z_{MT}}$. In the discretize form, we have

$$\frac{U(z_{MT}) - U(z_{MT} - \Delta z_{MT})}{\Delta z_{MT}} = k_S (z_{S_{i-1}} + \Delta z_S) \quad (23)$$

Where z_{Si-1} is the cantilever deformation at last step (index i indicates the current step). Note that $-\Delta z_{MT} < \Delta z_S < \frac{F_{\max}}{k_S} - z_{S_{i-1}}$. In the case of $\frac{U(z_{MT}) - U(z_{MT} - \Delta z_{MT})}{\Delta z_{MT}} - k_S z_{S_{i-1}} \geq 0$, we have $\Delta z_S \geq 0$. The force observed is just

$$F(z_{MT}) = \frac{U(z_{MT}) - U(z_{MT} - \Delta z_{MT})}{\Delta z_{MT}} \quad (24)$$

However, if $\frac{U(z_{MT}) - U(z_{MT} - \Delta z_{MT})}{\Delta z_{MT}} - k_S z_{S_{i-1}} < 0$, due to the constrain of cantilever movement at each step $-\Delta z_{MT} < \Delta z_S < \frac{F_{\max}}{k_S} - z_{S_{i-1}}$, the equilibrium status will not be hold and we have

$$F(z_{MT}) = F(z_{MT} - \Delta z_{MT}) + k_S \cdot \max(\Delta z_S, -\Delta z_{MT}) \quad (25)$$

Here we assume the change of MT wall deformation is limited and the AFM tip are always touched with MT wall. Eq. (25) gives the methods to calculate the force at MT wall deformation of z_{MT} when the process is not equilibrium. In fact, in the case of $\Delta z_S \geq 0$, Eq. (25) and (24) are identical. The F-I curves can be ploted based on Eq. (25) and (24).

Supplemental Results:

The effects of moving AFM tip crossing and along the MT PF:

Besides changing the size of AFM tip radius and the MT length, another set of simulations can be tested directly by experiments is to change the position of AFM tip by moving the tip crossing the MT (Fig. 3.S1 and Fig. 3.S3a) or along the MT longitudinal direction (Fig. 3.6e). Microtubules are polymers of α- and β-tubulin dimers. They polymerize end to end in protofilaments and then bundle into hollow cylindrical filaments. Therefore, the wall of microtubules is not smooth as "wall". There are in fact "bumps" along both longitudinal direction (z) and lateral direction (x). We find that the "bumps" along the protofilaments don't make observable difference on both linear and quasi-linear responses, but the ones formed between protofilaments do have effects on both kinds of mechanical responses.

Fig. 3.S3b plots the linear response of MT wall to the AFM tip while the tip starts from different *x* direction (Fig. 3.S3a) and then pushes the wall along negative *y* direction. Starting from the position x = 0 nm, the spring constant κ slightly decreases as the x varies away from zero point. But the decreasing trend stops temporarily at $x \approx$ 3.5 nm and then decrease again at similar rate as the one between x=0~3.5 nm. The decreasing trend stops again at about 4.5 nm position and the slope increases about 0.005 N/m and reaches maximum at 5.5 nm position. After that, the line drops quickly down to 0.01 N/m level. In these simulations, we use AFM tip radius R=15 nm. If we take a closer look of the MT structure (Fig. 3.S1), we found that the contact point of

AFM tip on MT wall is at the center of PF number 1 (see Fig. 3.S1) for x=0. When the tip moves away, the tip center was shifted away from PF 1. This decreases the effective spring constant a little bit, which is as observed in Fig. 3.S3b for x=0~3.5 nm. For x~3.5 nm, the tip contacts PF 2 and moves away from PF 1. That's why the κ increases at that point. The decreasing of κ after that is due to the similar reason as for x between 0 to 3.5 nm. The last increasing before x=5.5 nm is due to the multi-contacting points between tip and PF1, PF2 and even part of PF3 (please note that the tip Radius R=15 nm). That gives a big jump of linear response on tip pressure. For x>5.5 nm, since the tip moves away from the whole MT, the κ eventually decreases to zero if the tip have no contact with the MT wall.

The value of Γ (Fig. 3.S3c), on the other hand, increases from 3.5 to 5 nm when x changes from 0 to 3.8 nm and then stays at 5 nm level for about 4 nm shift. This step scale is at the same level of the monomer size (~4 nm in diameter). The system has this kind of response pattern because there are "bumps" between PFs on MT wall, which have 4 nm step scale on the wall. This changes the kink timing due to the force exerting pattern changes when the tip moves from center to the edge of the wall by crossing the "bumps" periodically.

Fig. 3.S3d-f plot the similar responses for AFM tip at different starting positions along longitudinal direction (z). The linear response is expectable to be stable before the boundary effects kick in and then to drops to zero as the tip moves to the upper edge of the MT and loses contact to the MT wall eventually (Fig. 3.S3e). The kink positions plot has correlated response. When the spring constant decreases, the kink position increases correspondingly. The soft end of the MT wall spread the force to

more monomers and effectively delays the events of bond transitions, which is represented by a kink in force-indentation curve.

The L1 Model fails to predict the gap behavior consistently:

To investigate the possibilities of generating gap behavior using L1 model, we performed large amount of simulations with L1 model. The results suggest that the L1 model fails to predict the gap behavior consistently under various conditions and different adjustable parameters.

As shown in the main text, L1 model fails to give continuous gap behavior when changing the AFM tip radius. The results can differentiate L1 and L2 model efficiently by proposing the experiments. In this section, we further examine the behavior of L1 model to validate our conclusion.

The estimated lateral binding free energy is -3.2~-5.7 k_BT (19). To complete investigate the model, we perform the simulation at different lateral binding free energy. The results show (Fig. 3.S4) that the L1 model can't predict the consistent results of gap behavior under various reasonable lateral free energy values -3 k_BT~-5.5k_BT (19). The gap happens either at very late stages or never happens. This observation further confirms the L1 model is not able to explain the quasi-linear behavior in a self-consistent way while the experimental observations are highly repeatable (12).

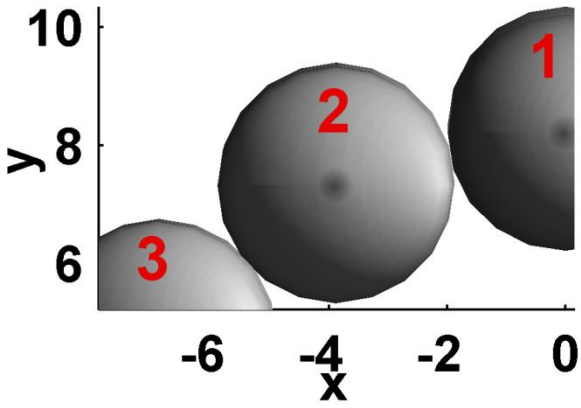

Figure 3.S1. The end on view of part of the MT wall before the AFM tip reaches the wall. The AFM tip is pressed down along the negative y direction. When the starting position of AFM tip moves from x=0 toward negative x direction, the monomer number 1, 2 and 3 contacts the AFM tip sequentially.

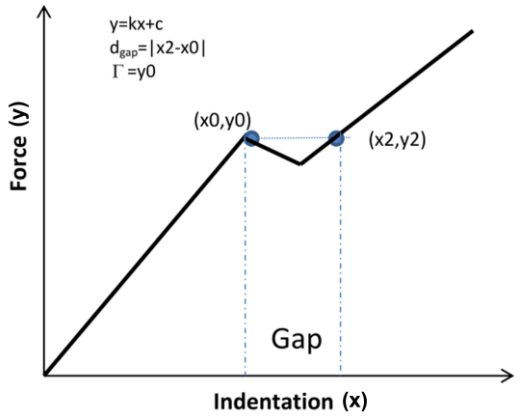

Figure 3.S2. The schematical illustration of calculating the "gap" from force-indentation curve. The gap width d_{gap} and kink position Γ are indicated in the figure.

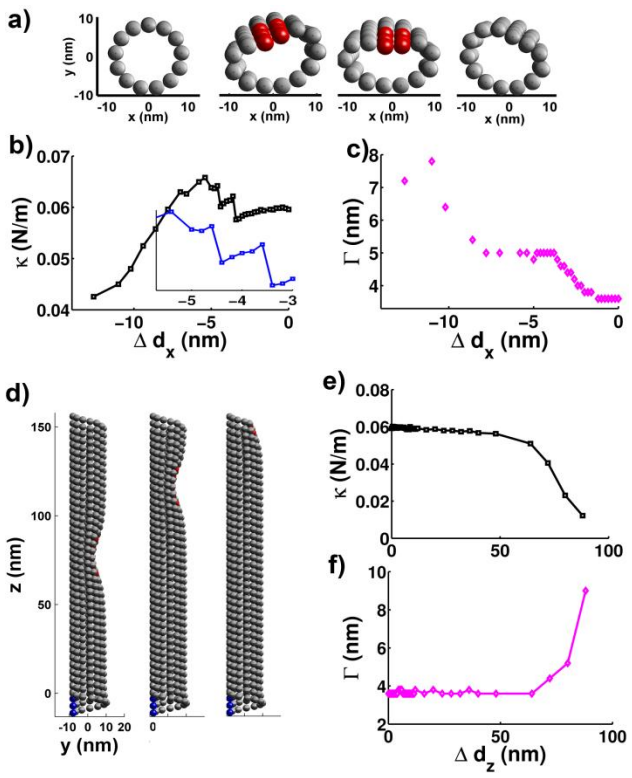

Figure 3.S3 **Effects of AFM tip positions shifting along both x (lateral direction) and z (longitudinal direction)**. (a-c) Shift of AFM tip along Lateral direction (x). (a) Selected MT configurations for tip center at the middle of the MT (z~=half of MT length) and x= -7, 0, and 11 nm. (b) Spring constant κ (Slope of linear region of Force v.s. Indentation curve) v.s. shift distance along x direction of AFM tip (Δd_x). Inset: the zoomed in plot for κ at $-5.5 \le \Delta d_x \le -3$ nm. (c) Γ (The recorded first kink position on Force v.s. Indentation curve) v.s. Δd_x. (d-f) Shift along MT PF (z direction). (d) Several MT conformations at indentation = 7 nm for Tip Position change from central = 0, 40, and 80 nm. (e)) Spring constant κ (Slope of linear region of Force v.s. Indentation curve) v.s. shift distance along z direction of AFM tip from the middle of the MT (Δd_z). (f) Γ (The recorded first kink position on Force v.s. Indentation curve) v.s. Δd_z.

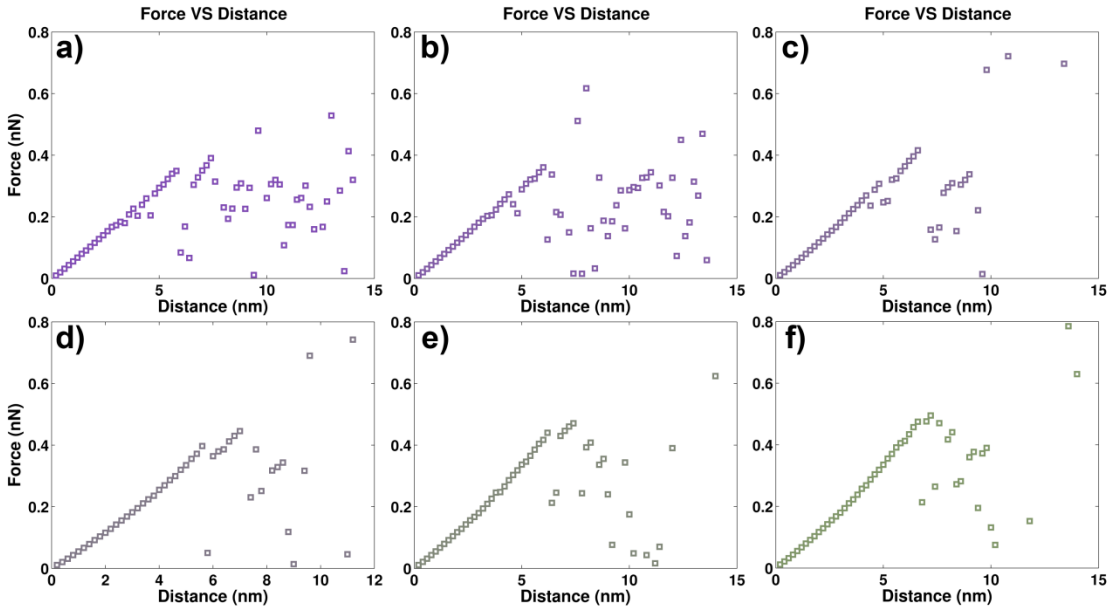

Figure 3.S4 Force V.S. Indentation curves for L1 model (tube only model) at various ΔG_{Lat} based on the literature estimated values (-3.2~-5.7 k_BT (19)). The plots show the curves for (a) -3 k_BT; (b) -3.5 k_BT; (c) -4 k_BT; (d) -4.5 k_BT; (e) -5 k_BT; (f) -5.5 k_BT. The results gives either no observable gap behavior or the gap at high indentation value (>5 nm) and the second linear region is relatively short.

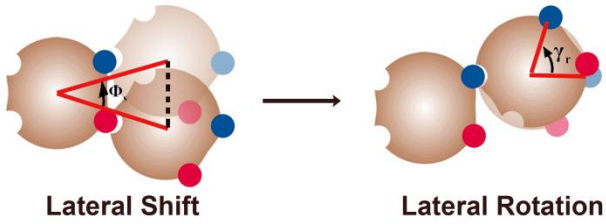

Figure 3.S5 the schematic demonstration of lateral shift and lateral rotation during the bond the transition.

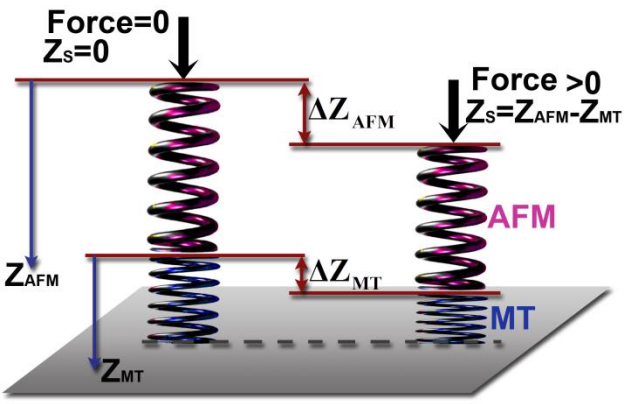

Figure 3.S6 The illustration of couple system of cantilever and MT wall. The cantilever is treated as linear spring and the MT wall is non-linear spring. z_S is defined as the deformation of cantilever spring, z_{AFM} is the upper position of cantilever, z_{MT} is the upper position of MT wall. The lower position of MT wall are immobilized on the glass. The left panel represents the relax status of the system and the right panel represents the status with force exerted on it.

Table 3.S1 Flexural Rigidity Measurements

Microtubules	Methods	Flexural Rigidity (x 10^{-24} Nm^2)	Temperature (^0C)	References
Pure MT	Buckling force	7.9	33	(5)
	Hydrodynamic flow	8.5	37	(11)
	Hydrodynamic flow	35.8	37	(7)
	Relaxation (RELAX)	3.7	22-25	(3)
	Relaxation (WIGGLE)	4.7	22-25	(3)
	Thermal fluctuation	26.0	37	(8)
	Thermal fluctuation	4.6	37	(11)
	Thermal fluctuation	26.5*	37	(7)
	Thermal fluctuation	18.5		(2)
	Thermal fluctuation	13.7-27.0*	23	(4)
Paclitaxel-stabilized	Buckling force	2.0	33	(5)
MT	Buckling force	2.0-22	37	(6)
	Relaxation (RELAX)	1.0	22-25	(3)
	Relaxation (WIGGLE)	1.9	22-25	(3)
	Thermal fluctuation	21.5	25	(3)
	Thermal fluctuation	32.0	37	(8)
	Thermal fluctuation	2.4	37	(11)
	Thermal fluctuation		37	(9)
	Electric force		37	(10)

*These values of EI were derived from measured persistence length l_p with $EI = k_B T \cdot l_p$.

References

1. VanBuren, V., L. Cassimeris, and D. J. Odde. 2005. Mechanochemical model of microtubule structure and self-assembly kinetics. Biophys J 89:2911-2926.
2. Cassimeris, L., D. Gard, P. T. Tran, and H. P. Erickson. 2001. XMAP215 is a long thin molecule that does not increase microtubule stiffness. Journal of Cell Science 114:3025-3033.
3. Felgner, H., R. Frank, and M. Schliwa. 1996. Flexural rigidity of microtubules measured with the use of optical tweezers. Journal of Cell Science 109:509-516.
4. Janson, M. E., and M. Dogterom. 2004. A bending mode analysis for growing microtubules: evidence for a velocity-dependent rigidity. Biophys J 87:2723-2736.
5. Kikumoto, M., M. Kurachi, V. Tosa, and H. Tashiro. 2006. Flexural Rigidity of Individual Microtubules Measured by a Buckling Force with Optical Traps. Biophysical Journal 90:1687-1696.
6. Kurachi, M., M. Hoshi, and H. Tashiro. 1995. Buckling of a single microtubule by optical trapping forces: Direct measurement of microtubule rigidity. Cell Motility and the Cytoskeleton 30:221-228.
7. Kurz, J. C., and R. C. Williams, Jr. 1995. Microtubule-associated proteins and the flexibility of microtubules. Biochemistry 34:13374-13380.
8. Mickey, B., and J. Howard. 1995. Rigidity of microtubules is increased by stabilizing agents. The Journal of Cell Biology 130:909-917.

9. Pampaloni, F., G. Lattanzi, A. Jonas, T. Surrey, E. Frey, and E. L. Florin. 2006. Thermal fluctuations of grafted microtubules provide evidence of a length-dependent persistence length. Proc Natl Acad Sci U S A 103:10248-10253.

10. Van den Heuvel, M. G., M. P. de Graaff, and C. Dekker. 2008. Microtubule curvatures under perpendicular electric forces reveal a low persistence length. Proc Natl Acad Sci U S A 105:7941-7946.

11. Venier, P., A. C. Maggs, M. F. Carlier, and D. Pantaloni. 1994. Analysis of microtubule rigidity using hydrodynamic flow and thermal fluctuations [published erratum appears in J Biol Chem 1995 Jul 14;270(28):17056]. Journal of Biological Chemistry 269:13353-13360.

12. Schaap, I. A., C. Carrasco, P. J. de Pablo, F. C. MacKintosh, and C. F. Schmidt. 2006. Elastic response, buckling, and instability of microtubules under radial indentation. Biophys J 91:1521-1531.

13. de Pablo, P. J., I. A. Schaap, F. C. MacKintosh, and C. F. Schmidt. 2003. Deformation and collapse of microtubules on the nanometer scale. Phys Rev Lett 91:098101.

14. Caplow, M., and J. Shanks. 1996. Evidence that a single monolayer tubulin-GTP cap is both necessary and sufficient to stabilize microtubules. Molecular Biology of the Cell 7:663-675.

15. Sept, D., and F. C. MacKintosh. 2010. Microtubule elasticity: connecting all-atom simulations with continuum mechanics. Phys Rev Lett 104:018101.

16. Kis, A., S. Kasas, B. Babi 膰, A. J. Kulik, W. Beno 頰, G. A. D. Briggs, C. Sch 鰊enberger, S. Catsicas, and L. Forr. 2002. Nanomechanics of Microtubules. Physical Review Letters 89:248101.

17. Kasas, S., A. Kis, B. M. Riederer, L. Forró, G. Dietler, and S. Catsicas. 2004. Mechanical Properties of Microtubules Explored Using the Finite Elements Method. Chemphyschem 5:252-257.

18. Wang, H. W., and E. Nogales. 2005. Nucleotide-dependent bending flexibility of tubulin regulates microtubule assembly. Nature 435:911-915.

19. VanBuren, V., D. J. Odde, and L. Cassimeris. 2002. Estimates of lateral and longitudinal bond energies within the microtubule lattice. Proc Natl Acad Sci U S A 99:6035-6040.

Chapter 4

A mechano-chemical model for microtubule assembly dynamics with sheet lateral bond involved

Zhanghan Wu[1,2], Jianhua Xing[1]

[1]Department of Biological Sciences, Virginia Tech, Blacksburg, VA 24061

[2]Program in Genetics, Bioinformatics and Computational Biology, Virginia Tech, Blacksburg, VA 24061

a. Abstract

The microtubule (MT) assembly and disassembly dynamics are essential to eukaryotic cells. Cell divisions and cell movements are highly dependent on proper behavior of MT dynamics. Thus, it is fundamental to fully understand microtubule assembly dynamics. Based on our previous work, a second bond involved in the lateral interactions between adjacent tubulin subunits, the sheet bond, plays important roles in both MT dynamics and mechanics. The sheet bond exists under physiological conditions and could be used to regulate the dynamics of MTs. In this work, we integrate the available information from both experimental and modeling work, and build a comprehensive model to describe the MT assembly dynamics. We show that the sheet end structures are hybrid structures containing different portions of sheet and tube bonds. The sheet width and length depends on the free tubulin concentration. The modeling predictions are consistent with experimental observations.

b. Introduction

MTs are long polymers made of hetero-tubulin proteins. They serve as one of the three major cytoskeletal components in eukaryotic cells. They play important roles in intracellular transportation, mechanical support of cell structure, cell proliferation, etc. MT malfunction may cause many diseases such as neurodegenerative diseases and several kinds of cancers. However, the structures, the mechanical properties, and assembly mechanisms of MTs are not fully understood yet. Some of them are highly controversial. One of the reasons could be that the experimental methods needed to understand the properties mentioned above are difficult to process. Therefore, mathematical modeling plays a critical role in this field, providing key hypotheses and enhancing the understanding of the mechanical behavior and assembly process of MTs.

Recently, Wang and Nogales observed a new type of tubulin lateral interaction (conventionally called a noncovalent bond in the field) in MTs. They found this interaction can exist stably in low temperature conditions. One natural question is whether this new lateral bond type plays a key role during the assembly process under physiological conditions, and whether it changes the linear and non-linear mechanical responses of the MTs. If so, another question is whether it can reconcile discrepancies between experimental results and existing model predictions which are based on one type of lateral interaction.

Based on experimental evidence and preliminary studies, it is reasonable to hypothesize that tubulins can form this new lateral bond type even under physiological

conditions. This bond type can affect the mechanical properties of MTs under mechanical stress. This bond can also help to form sheet structure as intermediates during the assembly process. The sheet intermediates could have important functions when MTs participated in cellular process. Therefore, it is necessary to include this new lateral interaction into a mathematical model that can simulate assembly processes of MTs under various conditions. In this work, we build such a model, which can consistently explain the available experimental observations and make predictions that could be important in biological system.

c. Methods

The model frame work is essentially the same as in Chapter 3 with some extra features to deal with the assembly dynamics. We use a coarse-grained modeling framework that treats an assembly of α and β tubulins as rigid bodies connected by elastic springs. The details can be found from Fig 3.1. The mechanical parameters are determined by both our previous modeling work and the experimental data. The parameters for dynamics are all adapted from previous work [1-3] and Chapter 3. The entropy of immobilization of a dimer is included in ΔG^*_{long}, the effective standard free energy for longitudinal bond. This is done in the same fashion as in [1].

The simulation always starts from an initial structure with different number of tubulins. There are two types of simulations: 1. Assuming the length of MT is long enough and our simulations only focus on the growing tip. 2. Assuming the polymerization is at very early stage. The assembly starts from free tubulins. Our simulations investigate the early growing behavior.

In each simulation, the Gillespie algorithm [4] is used to choose the reaction events and time elapsed during that reaction. After that, we perform the energy minimization on the structure as in Chapter 3. After the minimization, the cluster reaches its local minimum, and then another Gillespie step is performed until the predetermined maximum simulation step reaches.

d. Results

High tubulin concentration promotes the formation of sheet structure at growing end. Fig. 4.1 shows several typical structures of MT growing ends at different tubulin concentrations. For low tubulin concentration (5 μM), the simulated results show that blunt ends are observed in most case. Some of them have short extensions with 1 or 2 protofilaments. In very rare case, the very short sheet ends (which are in fact portion of incomplete tubes) are observed. As the tubulin concentration becomes higher and higher (up to 100 μM), sheet structures are observed more frequently and the sheet length increases (Fig. 4.1b-c). The sheet end structures are composed with portion of sheet bonds and tube bonds. The shapes are closer to tube with more tube bonds in the structure. We also observed that the split sheet structures are possible (Fig. 4.1 b-c). Two sheet ends are extended from the tube end and when the MT grows, these two sheets tend to merge together and form a complete tube. These observations are consistent with experimental observations [5-9]. The energy analysis shows that the sheet end structures are quite stable, although they are less stable than formed tubes (Fig. 4.1d-f). The simulations show that the sheet structures are intermediates during the MT assembly process. For the assembly of MT at high concentration of free tubulin,

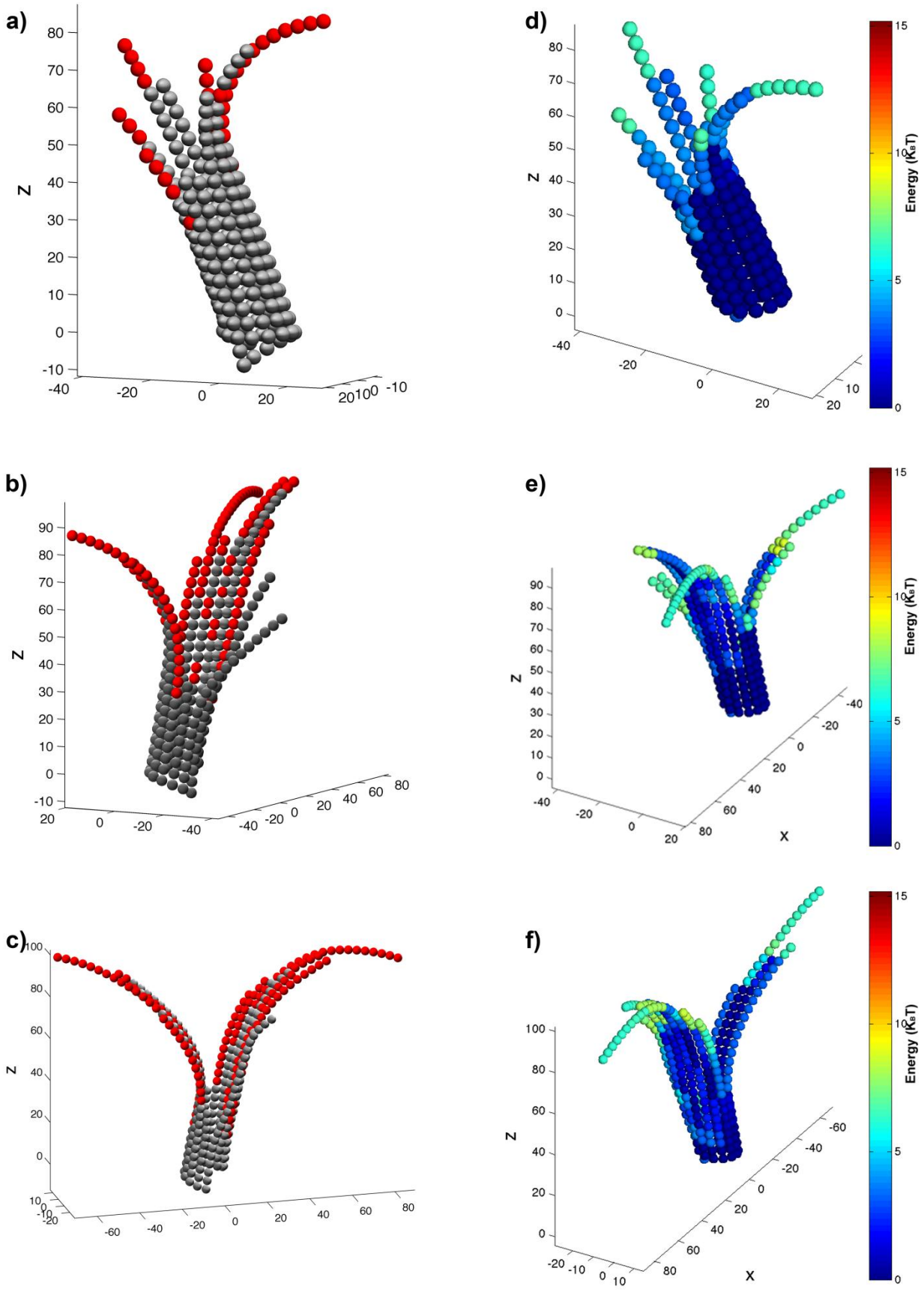
a)
b)
c)
d)
e)
f)
Z
X
Energy (KBT)

Figure 4.1 The typical simulated cluster structure of growing MT and corresponding energy status at different tubulin concentrations. (a-c) The cluster structure snapshot for the growing MT at free tubulin concentration of 5, 40 and 80 μM , respectively. (d-f) the corresponding energy plot for the cases in Fig. 4.1a-c.

the sheet structures are observed at the growing end. The simulations show that the sheet structures keep close to tubes while the new sheet ends are growing at the end. Although at lower free tubulin concentration, the observable sheet ends are rare, it does not mean the sheet bonds have no functional roles at low tubulin concentrations. The sheet-tube transition is faster than tubulin addition at lower concentration, which shortens the sheet end effectively. Fig. 4.2 gives the percentage of different events at various tubulin concentrations. There are more and more tubulin addition events as the tubulin concentration increases. This decreases the portion of sheet-tube transition events. It is called kinetic trap mechanism as discussed in [2]. Also, Fig. 4.3 shows that the MT growing velocity is increasing with tubulin concentration.

Early stages of MT assembly produce both small flat sheets and incomplete tubes. The simulations for very early stages of MT assembly also reveal that the sheet structure tends to form before it converts to tube structure. As shown in Fig. 4.4, there are small pieces of flat sheet structure observed at higher tubulin concentrations and more half tubes at lower concentrations. This is also consistent with experimental observations [10].

The model without sheet bond fails to predict sheet structure consistently. To further validate the 2-bond model, we performed the simulations within the framework of the 1-bond model under the same conditions (concentration, etc.). The results show

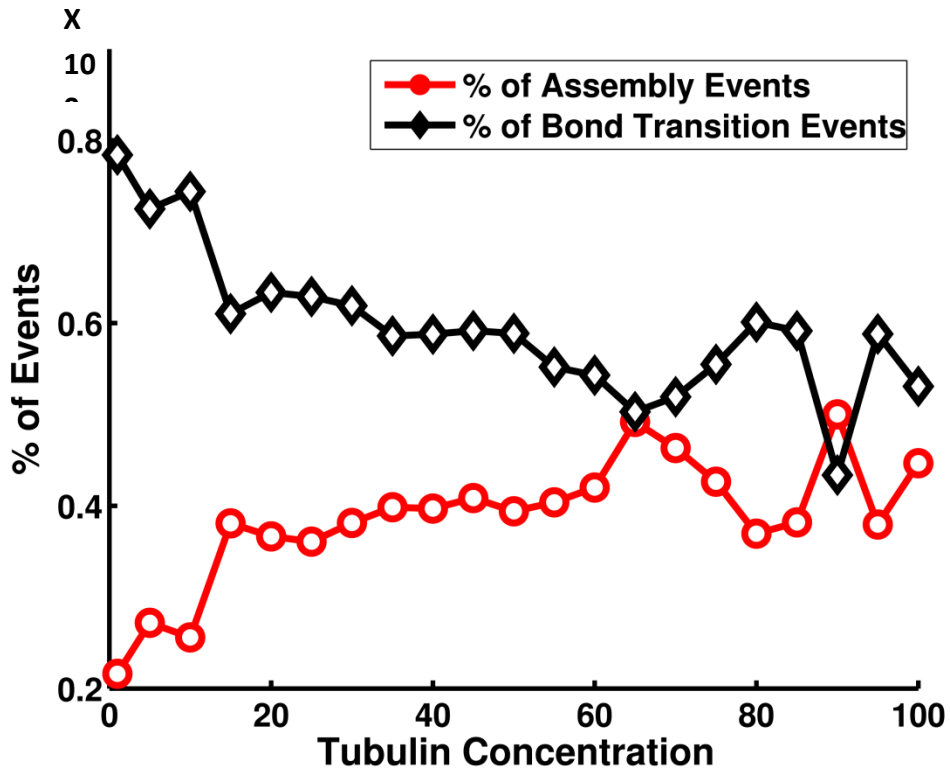

Figure 4.2 The percentage of events versus the tubulin concentration. Red circled line: the percentage of MT assembly events. Black diamond line: the percentage of bond transition events (sheet→ tube/ tube→sheet).

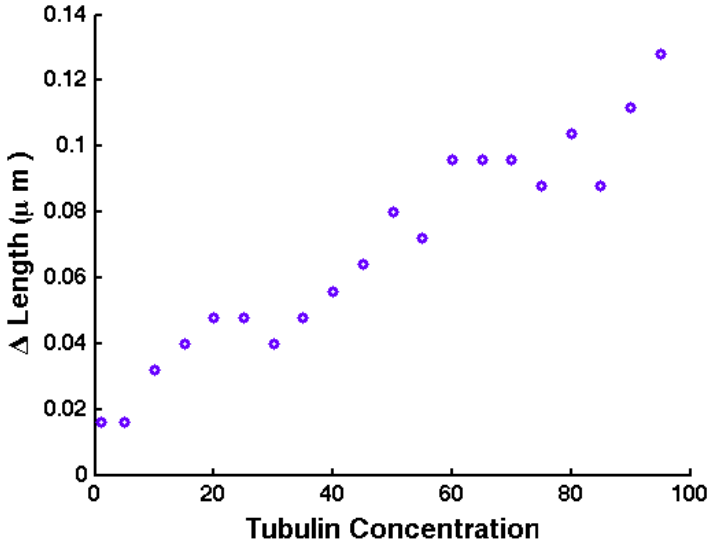

Figure 4.3 The growing length per unit time v.s. the tubulin concentration.

that the model without sheet bond cannot reproduce the sheet end structure regardless of tubulin concentration (Fig. 4.5). In fact, it is hard to tell the difference of the plus end structure at different concentration levels. This result, from another side, confirms that the sheet structure at the growing end of MT is an assembly intermediate and the conversion from sheet end structure to closed tube structure involves the sheet-tube bond transition.

e. Discussions and Conclusions

Whether tubulins can form the sheet bond *under physiological conditions* remains an unaddressed (or largely overlooked) fundamental question so far. We try to address this

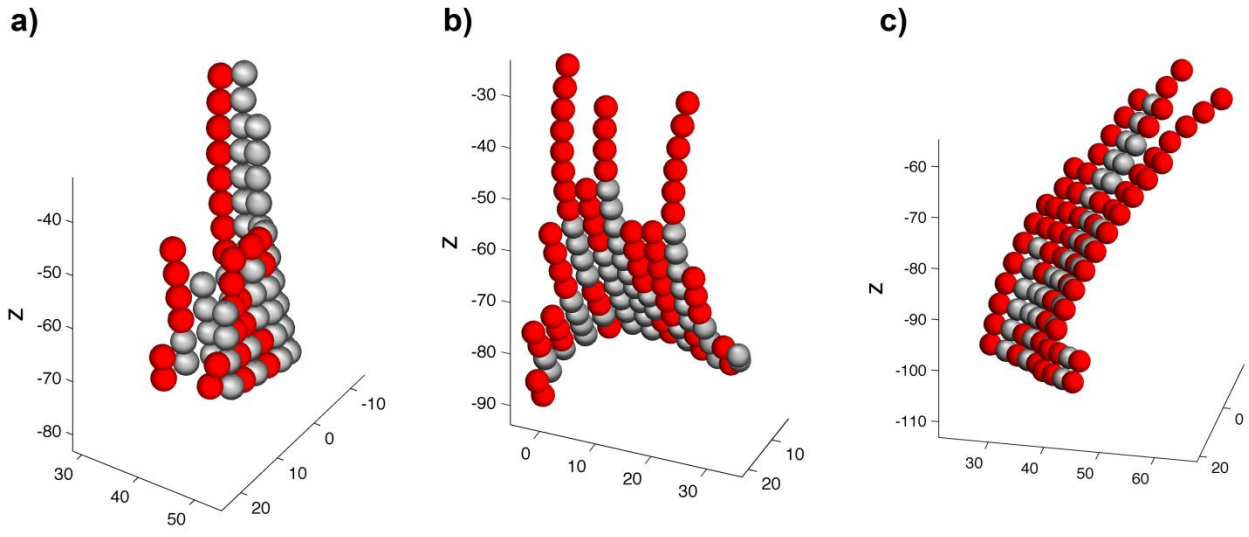

Figure 4.4 The simulated cluster structure of growing MT at very early stage for different tubulin concentrations. (a)-(c) the structure with free tubulin concentration of 5, 25 and 50 μM , respectively.

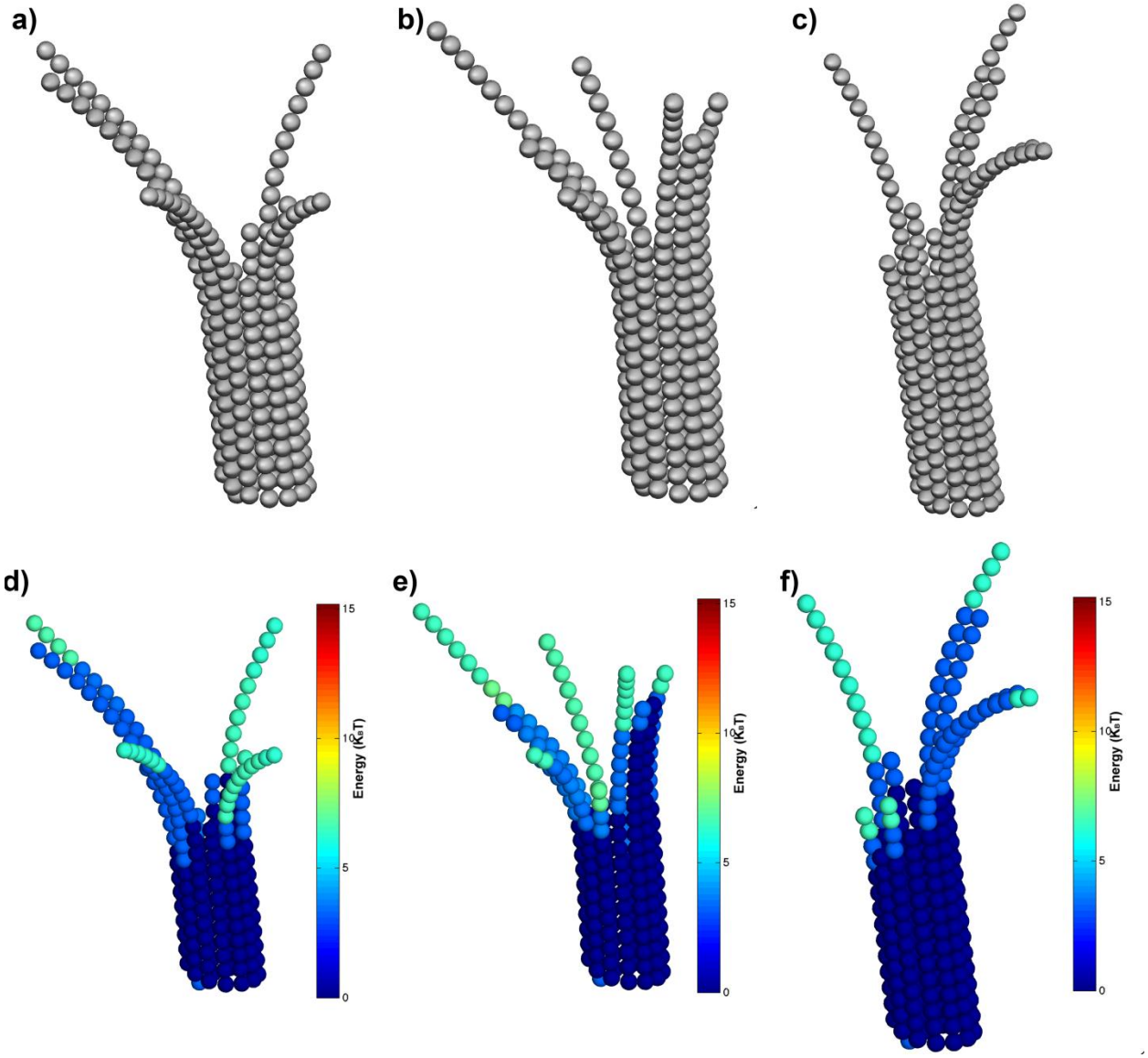

Figure 4.5 The simulated results for tube-only model. All other conditions and parameters are the same as in Fig. 4.1. (a-c) the structure with free tubulin concentration of 5, 40 and 80 μM, respectively. (d-f) the corresponding energy status of the cluster.

problem for the first time via modeling efforts. This is the first effort in the field to build a comprehensive model to identify the sheet bond and analyze the mechanical (Chapter 3) and dynamical properties (Chapter 4) of MTs including this sheet bond.

One may argue that the new bond found by Wang and Nogales might not be relevant under physiological conditions and it would be of no interest to study the new lateral bond. However, this argument is not solid because of the following reasons.

First, existing experimental results are insufficient to rule out the physiological relevance of Wang and Nogales' structure containing sheet lateral bonds. Obtaining the structure under non-physiological conditions does not necessarily lead to the conclusion that the new type of lateral interaction is physiologically irrelevant.

Second, we have noticed that this new type of interaction closely resembles what is observed in the *in vivo* doublet MT structures [2, 11]. It provides strong evidence that this sheet bond exists under physiological conditions. The axoneme "forms the core of eukaryotic flagella and cilia and is one of the largest macromolecular machines" [11]. The doublet MT arrangement present in axonemes can be viewed as two fused MTs. In the newly obtained doublet structure of Sui and Downing, one PF interacts with two PFs simultaneously. One interaction resembles the tube bond and the other structurally resembles the sheet bond [2, 11]. It is, thus, justified to say that tubulins can form the sheet bond *in vivo*. We also noticed that comparative bioinformatics studies reveal that the residues participating in the sheet bonds are evolutionarily more conserved than those forming the tube bonds [2, 12]. This trend is not likely to be accidental but suggests that these residues are functionally essential.

Third, there are still unresolved contradictions between experimental observations and computational modeling results based on the conventional (MT only) model. Chrétien et al. observed sheet structures at the growing end of a MT as long as a micron [13] (Figure 2). They performed extensive theoretical studies on the sheet structure with a continuum elastic model, assuming only one type of lateral bond [13, 14]. However, one should treat the conclusions from the continuum model studies with caution. The work does not address how and whether the *a priori* assumed sheet structure can form within the conventional model in the first place. Systematic stochastic modeling studies by VanBuren et al. show that, based on the conventional L1 model (only one bond type considered in lateral interaction), it is very unlikely to form long incomplete structures at an MT growing end. The structures are energetically unfavorable and are precursors for disassembly rather than assembly [15]. The authors did not examine dependence of sheet length on tubulin concentration. One would expect weak or inverse dependence, since low tubulin concentrations favor disassembly and, thus, sheet formation according to VanBuren et al. [15]. This is in contradiction to the observation that the sheet structures are observed under growth conditions and become longer upon increasing tubulin concentrations [13]. The conventional L1 model also has difficulty explaining the long and helical shape revealed by low-resolution cryo-EM images.

Based on the experimental evidence and our modeling work, we believe that this new type of tubulin-tubulin bond (sheet bond) has to be explicitly considered to analyze both the mechanical and dynamical behavior of MTs. This new type of lateral interaction may play important functional roles that are different from those of the normal lateral

interaction (called a *tube bond*). Sheet bonds, together with the tube bonds, lead to the sheet structure, which is thought to be a kinetically trapped intermediate during MT assembly and contribute to the mechanical properties of MTs.

f. Acknowledgement

ZW and JX are supported by the Thomas F. Jeffress and Kate Miller Jeffress Memorial Trust.

g. References

1. VanBuren, V., L. Cassimeris, and D.J. Odde, *Mechanochemical model of microtubule structure and self-assembly kinetics.* Biophys J, 2005. **89**(5): p. 2911-26.
2. Wu, Z., et al., *Simulations of Tubulin Sheet Polymers as Possible Structural Intermediates in Microtubule Assembly.* PLoS ONE, 2009. **4**(10): p. e7291.
3. Molodtsov, M.I., et al., *A molecular-mechanical model of the microtubule.* Biophys J, 2005. **88**(5): p. 3167-79.
4. Gillespie, D.T., *Exact stochastic simulation of coupled chemical reactions.* J. Phys. Chem., 1977. **81**(25): p. 2340-2361.
5. Chretien, D., S.D. Fuller, and E. Karsenti, *Structure of growing microtubule ends: two-dimensional sheets close into tubes at variable rates.* J Cell Biol, 1995. **129**(5): p. 1311-28.
6. Vitre, B., et al., *EB1 regulates microtubule dynamics and tubulin sheet closure in vitro.* Nat Cell Biol, 2008. **10**(4): p. 415-421.

7. Arnal, I., E. Karsenti, and A.A. Hyman, *Structural Transitions at Microtubule Ends Correlate with Their Dynamic Properties in Xenopus Egg Extracts.* The Journal of Cell Biology, 2000. **149**(4): p. 767-774.

8. Erickson, H.P., *Microtubule surface lattice amd subunit structure and observations on reassembly.* J. Cell Biol., 1974. **60**(1): p. 153-167.

9. Arnal, I., et al., *CLIP-170/Tubulin-Curved Oligomers Coassemble at Microtubule Ends and Promote Rescues.* Current Biology, 2004. **14**(23): p. 2086-2095.

10. Mozziconacci, J., et al., *Tubulin Dimers Oligomerize before Their Incorporation into Microtubules.* PLoS ONE, 2008. **3**(11): p. e3821.

11. Sui, H. and K.H. Downing, *Molecular architecture of axonemal microtubule doublets revealed by cryo-electron tomography.* Nature, 2006. **442**(7101): p. 475-478.

12. Fygensonm, D., D. Needleman, and K. Sneppen, *Variability-based sequence alignment identifies residues responsible for functional differences in α and β tubulin.* Protein Sci., 2004. **13**(1): p. 25-31.

13. Chretien, D., S.D. Fuller, and E. Karsenti, *Structure of growing microtubule ends - 2-dimensional sheets close into tubes at variable rates.* J. Cell. Biol., 1995. **129**(5): p. 1311-1328.

14. Jánosi, I.M., D. Chrétien, and H. Flyvbjerg, *Modeling elastic properties of microtubule tips and walls.* Eur. Biophys. J, 1998. **27**(5): p. 501-513.

15. VanBuren, V., L. Cassimeris, and D.J. Odde, *Mechanochemical Model of Microtubule Structure and Self-Assembly Kinetics.* Biophys. J., 2005. **89**(5): p. 2911-2926.

Chapter 5

Functional roles of slow enzyme conformational changes in network dynamics

Zhanghan Wu[1], Jianhua Xing[11]

[1]Department of Biological Sciences, Virginia Polytechnic Institute and State University, Blacksburg, VA 24060

a. Abstract

Extensive studies from different fields reveal that many macromolecules, especially enzymes show slow transitions among different conformations. The phenomenon is named as dynamic disorder, heterogeneity, hysteretic and mnemonic enzymes in different fields, and is directly demonstrated by single molecule enzymology and NMR studies. We analyzed enzyme slow conformational changes in the context of regulatory networks. A single enzymatic reaction with slow conformational changes can be noise buffer filtering upstream fluctuations, shows resonance and adaptation, and thus serves as a basic functional motif with properties normally discussed with larger networks in the field of systems biology. We further analyzed examples including enzymes functioning against pH fluctuations, metabolic state change of *Artemia* embryos, kinetic insulation of fluctuations in metabolic networks, and possible synthetic networks with various properties. The work fills the missing gap between studies on intramolecular and network dynamics, and suggests that the conformational dynamics of some enzymes may be evolutionally selected, and should be taken into considerations in network dynamics studies.

b. Introduction

Molecules in a cell interact with each other to form an interconnected complex network regulating every aspect of the cell dynamics. It becomes an active research area on understanding the design principles of biological regulatory networks. Several structural motifs have been proposed to possess certain dynamic properties and corresponding physiological functions [1-5]. For example, it has been widely discussed on how a network functions robustly despite all the stochastic processes in a biological system. In almost every existing study, the focus is on network topology. Intramolecular dynamics are assumed to be fast compared to dynamics involving intermolecular interactions, and unnecessary for considerations. That is, molecules are treated as mere structure-less vortices or edges within a network, e.g. the one shown in Figure 5.1.

However, numerous experimental evidences challenge this view. Dynamic disorder, or dynamic heterogeneity, has been discussed extensively in the physical chemistry and biophysics communities. It refers to the phenomena that the 'rate constant' of a process is actually a random function of time, and is affected by some slow protein conformational motion. Since the pioneering work of Frauenfelder and coworkers on ligand binding to myoglobin [6], extensive experimental and theoretical studies have been performed on this subject (see for example ref. [7] for further references). Recently, single molecule enzymology and NMR measurements demonstrated directly that the catalytic activity of several enzymes at single molecule level is slowly fluctuating [8-14]. These studies suggest that the existence of dynamic disorder in macromolecules is a rule rather than the exception [15]. Consistently, biochemistry studies reveal that a large number of enzymes involve conformational changes comparable or even slower than

the actual chemical bond forming and breaking processes, and show non-Michaelis-Menten kinetics. Hysteretic enzymes refer to “those enzymes which respond slowly (in terms of some kinetic characteristic) to a rapid change in ligand, either substrate or modifier, concentration” [16]. Mnemonic behavior refers to the following model for enzymes with memory [17, 18]: an enzyme molecule has (at least) two conformers with different stability and catalytic activity; conformer 1 is more stable without the substrate, but substrate binding changes the relative stability, and at the end of an enzymatic cycle a product release generates free conformer 2 more likely, which converts to conformer 1 given sufficient waiting time before new substrate binding; increasing substrate concentration decreases the waiting time for substrate binding, and thus more enzymes are locked in conformer 2. The catalytic activity of a mnemonic enzyme varies with substrate concentration. The phenomena discussed in these different fields all originate from the fact that proteins are not rigid bodies, but are ever-fluctuating entities with broad time scale distribution from picoseconds to hours. The slow end of the time scale is comparable to many network level processes. Therefore it is natural to ask the possible consequences of molecular level fluctuations on network dynamics. Furthermore, is the intramolecular dynamic property of a macromolecule a consequence of natural selection? Frieden noticed that “*it is of interest that the majority of enzymes exhibiting this type of (hysteretic) behavior can be classed as regulatory enzymes*” [19].

Figure 5.1 schematically shows that enzymatic reactions within a network may have complex dynamics involving enzyme conformational changes. This work is to fill the missing gap between decades of accumulations of molecular level experimental data

and observations, and analysis in the context of network dynamics. We focus on examining the basic dynamic properties and functional roles of those enzymes with profound slow conformational changes in network dynamics. Therefore, we adopt minimal models representing the enzymes and networks, and leave enzyme models, which are more sophisticated and complex but also may be distractive, for future studies [20].

c. Results

Enzyme with slow conformational changes can serve as noise filter and adaptation motif: We first analyzed the representative enzymatic reaction shown in Figure 5.1. We set the rate constants for those reactions represented by dashed lines to be zero for simplicity, and choose other rate constants subject to detailed balance requirements. Figure 5.2a shows that this simple motif with slow conformational change filters high frequency stochastic fluctuations of the substrate concentration [S]. The power spectra in Figure 5.2b further shows that, assuming the input substrate concentration subject to white-noise like fluctuations, with the chosen parameters the motif filters both high and low frequencies. For further analysis, we examined the system response to monochromatic sinuous [S] fluctuations. While this analysis is normally used for linear systems, our usage is justified noticing that nonlinear contribution to the responses is negligible for the system we examine. As shown in Figure 5.2c, an enzyme with slow conformational changes has a finite response time, thus variation of the product concentration ΔP can follow the low but not high frequency substrate fluctuations. Figure 5.2d shows that ΔP_m, the maximum change of product concentration under sinuous variation of [S] increases with the conformational change

rate between ES and E'S, β_e. In these calculates the rate for the reverse reaction between ES and E'S α_e changes proportionally to keep α_e / β_e constant. It has higher dependence on β_e at lower frequency. Consequently, as shown in Figure 5.2d, at a fixed β_e value ΔP_m can be either a monotonic decreasing function of the [S] varying frequency ω, or has a maximum at certain resonant frequency, similar to what observed in Figure 5.2b.

Figure 5.2e-h show another property of the motif. Upon a sudden and sustained increase of [S], the product concentration [P] relaxes to a new steady state, which may be higher than, close to, or counter-intuitively lower than the original steady state. We examine the system dynamics upon varying the three rate constants shown in Figure 5.1, α_e, β_e and k_1, while keeping other parameters fixed. The detailed balance requirement constrains the three parameters further that $\alpha_e/(\beta_e k_1)$ must be kept constant. With certain parameters, [P] increases temporally then decreases from a maximum value. The ability of the system to respond to a change then relax to a preset value is essentially adaptation. Adaptation is an important dynamic property observed in many biological systems. Numerous studies have been focused on identifying network structures giving rise to adaptation [1, 4, 21]. Notice here that the adaptation can be achieved by a *single* enzymatic reaction. Following standard measures on adaptation, Figure 5.2g and h show how sensitivity (defined as the difference between the peak response and initial value) and precision (defined as the difference between the final and initial values) vary with enzyme conformational change rate. Adaptation requires slow conformational change. When conformational change is no longer rate-limiting, ΔP simply increases with ΔS as

one expects intuitively. Physically one can understand the dynamic property of the system as follows. Notice that in the network of Figure 5.1a, a complete enzymatic cycle can either go through E' → E→ES→ or E'→E'S→ ES. The two pathways compete for the limited source of enzyme molecules. At low [S], there is sufficient time for a newly released enzyme in the form E' from a complex E'P to convert to E before binding to a substrate molecule, thus takes the first pathway. Upon increasing [S], however, more reactions may take the second pathway. In the case that E'S→ ES is the rate-limiting step, the effective turn-over rate drops since many enzyme molecules are trapped in the E'S state. Figure 5.2h confirm this picture. With a fixed value of β_e, increasing α_e, and so k_1, lead to more trapped E'S and thus lower [P].

We also examined the network in Figure 5.2b, which can similarly filter substrate and modulate fluctuations. Below we use several examples to examine the functional roles of slowly-changing enzymes as molecular noise filters, and possible building blocks of larger networks with certain dynamic properties.

Filtering and buffering upstream or environmental fluctuation: The catalytic activity of each enzyme is pH-sensitive, and drops dramatically when the environmental pH value deviates away from its optimal pH value. For example, a change as small as 0.05 pH unit can substantially inhibit the enzyme activity of phosphoructokinase, an important enzyme in the glycolysis cycle [22, 23]. However, despite tight regulations, intracellular pH inevitably fluctuates transiently [24, 25], which may be detrimental. The negative feedback mechanism frequently appeared in cellular regulation networks is not practical here given the large number of enzymes involved. Instead Nature may have designed a

much simpler solution using slow conformational changes. Numerous enzymes show hysteretic response to pH fluctuations. One example is nitrate reductase, which catalyzes the reduction of nitrate to nitrite, a rate-limiting (thus a regulatory) step in the nitrate assimilation process in higher plants and algae [26-29]. Another example is alkaline phospatase (AP) which is also physiologically important. Phospatases are a large class of enzymes responsible for removing phosphate groups from other molecules. They counteract kinases, which add phosphate groups to molecules, and play important roles in cell regulation. AP gets its name because its optimum pH >7. In human being, AP is present in every tissue throughout the body. Experiments show that upon changing environmental pH values, AP activity adapts hysteretically to the change as slow as two hours [30]. We generalize the classical diprotonic model for enzyme pH dependence, as shown in Figure 5.3a. Each enzyme molecule has two protonable sites, with only the monoprotonated form catalytically active. Each molecule stochastically interconverts between two conformations with different proton affinity. The model correctly gives the pH dependence of enzyme catalytic activity (see Figure 5.3b). Subject to transient pH changes, Figure 5.3c & d show that slower conformational interconversion rate leads to slower enzyme response, which provides response time for the intracellular pH regulation toolkits before resulting in detrimental effects.

Recently, intramolecular dynamics of the *Mycobacterium tuberculosis* protein tyrosine phosphatase PtpB [12], and the Von Willebrand factor-binding protein for blood coagulation [31] have been experimentally characterized. Slow conformational changes may likely play similar buffering roles in these systems.

Reconciling ultrasensitivity and robustness: Cells often need to change their phenotypes and subphenotypes upon environmental change. Figure 5.4a shows one example. Changing the intracellular pH value of brine shrimp *Artemia* embryos from >7.9 to 6.3 (e.g. due to deprivation of oxygen) leads the cell to switch from a metabolically active state to a dormant state with very low metabolic activities. The embryo can survive in this dormant state for several years and switch back to normal state upon changing intracellular pH value back to basic values. Figure 5.4b shows two basic dynamic behaviors with dramatic system property changes frequently found in regulatory networks [32]. The upper panel shows a sigmoidal shaped response curve, which allows the system to response to pH value change sensitively. However, the system may switch back and forth undesirably between the two high and low enzyme activity states upon fluctuations of pH near point c. The lower panel shows a bistable response. That is, the system may have two steady states with a controlling parameter, e.g. pH, at a given value between a and b in the lower panel of Figure 5.4b. Bistability allows a system to resist small amplitude fluctuations with the capacity increases upon increasing the value (b-a), and avoids frequent dramatic changes of the cell state. For example, the system initially staying at the lower branch remains until pH value >b. However, larger capacity to resist fluctuations also means a larger value of (b - a) and less sensitive response to pH value changes. Therefore robustness to transient fluctuations, and sensitivity to (sustained) changes of the controlling parameters are two seemingly opposite requirements to the regulatory network.

For *Artemia* embryos, Hand and Carpenter found that this transition is mediated by the hysteretic enzyme trehalase [33]. As illustrated in Figure 5.4a, the disaccharide trehalose

is a main energy source used by the embryo, which is converted to glucose by the enzyme trehalase. The end-product, ATP, can inhibit this conversion reaction. Trehalase can form a polymerized complex with doubled mass and reduced enzyme activity. Remarkably, at basic conditions the monomer form is more stable, and the dimer-to-monomer transition takes place in less than 10 mins. Conversely, at pH = 6.3, it takes more than an hour for the monomer-to-dimer transition to finish. Our modeling studies show that with the available experimentally measured parameter values, the system can give rise to sigmoidal response curve to the pH value (upper panel of Figure 5.4b), but not bistability with the network shown in Figure 5.4a. For transient fluctuations around the transition point c for a sigmoidal response (Figure 5.4c), the hysteretic enzymes cannot response quickly before the large fluctuations die off (see the solid line of Figure 5.4d). Consequently, an *Artemia* embryo in the dormant state can respond to pH changes sensitively and converts to the active state. Once in the active state, the embryo is robust against transient fluctuations without switching back to the dormant state. On the other hand, Figure 5.4e shows a hypothetical system with bistable response. With certain rare large amplitude fluctuation, the system response may jump from one branch to another one, and be trapped for a prolonged period before another rare large amplitude fluctuation brings it back.

Insulating local network fluctuations: Biological networks are highly interconnected. It is analogous to a spider's web. When one stripe is pulled, will it disturb the whole network? Clearly it would be generally detrimental to the proper function of a biological network. For metabolic networks, some metabolic intermediates are highly toxic. Large concentration fluctuations of these species are undesirable to cells. There are many

ways to restrain their damage to cells. One possibility is to carefully insulate their dynamics from fluctuations of other parts of the network. Most hysteretic enzymes identified in the early days are regulatory enzymes in metabolic networks. Frieden summarized some typical network motifs with hysteretic enzymes abstracted from realistic networks such as *E Coli* Threonine synthesis pathway. We analyzed two of them shown in Figure 5.5. For both networks, the end-product inhibition mechanism can remove fluctuations of F at the expense of inducing fluctuations of F' in another parallel pathway sharing common ancestor metabolites. Hysteretic enzymes reduce the coupling between these two pathways. The results show that slower enzyme conformational change leads to smaller F' response. The two networks shown in Figure 5.5 respond to F fluctuations differently. In the first network (upper), longer F fluctuations lead to larger and more sustained F' fluctuations, thus F' responses to the duration of F' fluctuations. In the second network (lower), F' responses to the rate of F change. Faster F change results in larger F' response. Figure 5.S1 provides additional results supporting the above observations. The observed differential and integral response behaviors are essentially the same as those of the more complicated kinetic insulation networks of Behar et al. [2].

Building blocks for larger networks: As already illustrated by some of the above examples, incorporating hysteretic enzymes into larger network structures can lead to desirable dynamic properties. Figure 5.6a & b show two additional examples. As demonstrated in Figure 5.6c & d, a cascade of hysteretic enzyme catalyzed reactions shows sharper filtering and resonance spectra on increasing the cascade length.

Coupling a hysteretic catalyzed reaction with another reaction with sigmoidal shaped response also lead to sharper resonance spectrum, as shown in Figure 5.6e.

e. Discussions

In this work, we demonstrate that intramolecular conformational fluctuations can couple to cellular network dynamics, and have important physiological functions. Specifically we show that enzymes can use slow intramolecular conformational changes to buffer transient system fluctuations, functionally replacing some more complex network motifs involving several molecule species. For example, compared to the example in Figure 5.4, one widely-discussed network motif selectively responding to sustained signals is the coherent feed-forward loop motif [34]. The network dynamics discussed in Figure 5.5 closely resembles that of Behar et al [2]. We used several examples to illustrate possible functions of hysteretic enzymes, and suggest that one can also use hysteretic enzyme catalyzed reactions to engineer networks with certain dynamic properties.

Existing experimental information on slow conformational fluctuations focuses on enzymes. One expects that it may be ubiquitous for proteins and other macromolecules to have conformational fluctuations spanning a broad distribution of time scales. It requires further experimental studies to test this hypothesis. The molecular fluctuation dynamics, especially some regulatory proteins, is likely under selection pressure. We suggest that the biological consequences of the phenomenon can only be fully understood in the context of network dynamics.

We leave other possible functional roles of slow intramolecular fluctuation for future studies. For example at low copy numbers the observed enzyme catalytic activity fluctuations may contribute to noises in a network. Xing also proposed possible roles of

conformational dynamics in allosteric regulation [20]. Fraunfelder et al. provided another prospective on the function of protein conformational fluctuations [35]. Their work also suggests possible mechanisms of protein-protein interactions through coupling between the dynamics of proteins, solvation shell, and the solvent. The concept of dynamic disorder can also be further generalized in cell network studies. Suppose that the dynamics of a network is described by a set of ordinary differential equations d**x**/dt = f(**x**,c), with **x** the concentrations of species involved. The set of “constants”, such as rate constants, total molecule concentrations, are often slowly varying quantities, due to conformational fluctuations as discussed in this work, stochastic synthesis and degradation, etc [36]. In cell biology this phenomenon of dynamic disorder is usually called “nongenetic heterogeneity” [37]. When the corresponding deterministic dynamics of a network is near a transition point, e.g., a bifurcation point, consequences of the transient parameter fluctuations can be further amplified and temporarily frozen [38], as illustrated in Figure 5.4e, which may explain the observed larger and slower time scale (in days or longer) stochasticity [39].

f. Methods

All calculations were performed through solving the corresponding rate equations in the form of ordinary and stochastic differential equations with Matlab. Numerical details, model parameters, and the Matlab codes can be found in the online Supporting Information.

g. Acknowledgement

We thank Hans Fraunfelder, Haw Yang for helpful discussions. This work is supported by National Science Foundation Grant EF-1038636.

h. References

1. Alon, U., *An introduction to systems biology: Design principles of biological circuits*. 1 ed. mathematical & computational biology series2007: Chapman and Hall/CRC. 320.
2. Behar, M., H.G. Dohlman, and T.C. Elston, *Kinetic insulation as an effective mechanism for achieving pathway specificity in intracellular signaling networks.* Proc Natl Acad Sci U S A, 2007. **104**: p. 16146-16151.
3. Brandman, O., et al., *Interlinked fast and slow positive feedback loops drive reliable cell decisions.* Science, 2005. **310**(5747): p. 496-498.
4. Ma, W., et al., *Defining Network Topologies that Can Achieve Biochemical Adaptation.* Cell, 2009. **138**(4): p. 760-773.
5. Gardner, T.S., C.R. Cantor, and J.J. Collins, *Construction of a genetic toggle switch in Escherichia coli.* Nature, 2000. **403**(6767): p. 339-342.
6. Austin, R.H., et al., *Dynamics of Ligand-Binding to Myoglobin.* Biochemistry, 1975. **14**(24): p. 5355-5373.
7. Zwanzig, R., *Rate-Processes with Dynamic Disorder.* Acc. Chem. Res., 1990. **23**(5): p. 148-152.
8. Xie, X.S. and H.P. Lu, *Single-molecule enzymology.* J. Biol. Chem., 1999. **274**(23): p. 15967-15970.
9. English, B.P., et al., *Ever-fluctuating single enzyme molecules: Michaelis-Menten equation revisited.* Nat. Chem. Biol., 2006. **2**(2): p. 87-94.
10. Min, W., et al., *Observation of a power-law memory kernel for fluctuations within a single protein molecule.* Phys. Rev. Lett., 2005. **94**(19): p. 198302.

11. Lu, H.P., L. Xun, and X.S. Xie, *Single-molecule enzymatic dynamics.* Science, 1998. **282**: p. 1877-1882.

12. Flynn, E.M., et al., *Dynamic Active-Site Protection by the M. tuberculosis Protein Tyrosine Phosphatase PtpB Lid Domain.* J. Am. Chem. Soc., 2010. **132**(13): p. 4772-4780.

13. Eisenmesser, E.Z., et al., *Enzyme dynamics during catalysis.* Science, 2002. **295**(5559): p. 1520-1523.

14. Henzler-Wildman, K.A., et al., *A hierarchy of timescales in protein dynamics is linked to enzyme catalysis.* Nature, 2007. **450**(7171): p. 913-916.

15. Min, W., et al., *Fluctuating enzymes: Lessons from single-molecule studies.* Acc. Chem. Res., 2005. **38**(12): p. 923-931.

16. Frieden, C., *Kinetic Aspects of Regulation of Metabolic Processes. The hysteretic enzyme concept.* J. Biol. Chem., 1970. **245**(21): p. 5788-5799.

17. Rabin, B.R., *Co-operative effects in enzyme catalysis: a possible kinetic model based on substrate-induced conformation isomerization.* Biochem. J., 1967. **102**: p. 22c-23c.

18. Ricard, J., J.-C. Meunier, and J. Buc, *Regulatory behavior of monomeric enzymes. 1. The mnemonical enzyme concept. .* Eur. J. Biochem., 1974. **49**(1): p. 195-208.

19. Frieden, C., *Slow Transitions and Hysteretic Behavior in Enzymes.* Ann. Rev. Biochem., 1979. **48**(1): p. 471-489.

20. Xing, J., *Nonequilibrium dynamic mechanism for allosteric effect.* Phys. Rev. Lett., 2007. **99**: p. 168103.

21. Barkai, N. and S. Leibler, *Robustness in simple biochemical networks.* Nature, 1997. **387**(6636): p. 913-917.

22. Hand, S.C. and J.F. Carpenter, *pH-induced hysteretic properties of phosphofructokinase purified from rat myocardium.* Am J Physiol Regul Integr Comp Physiol, 1986. **250**(3): p. R505-511.

23. Hand, S.C., *Oxygen, pH_i and arrest of biosynthesis in brine shrimp embryos.* Acta Physiologica Scandinavica, 1997. **161**(4): p. 543-551.

24. Heiple, J.M. and D.L. Taylor, *Intracellular pH in single motile cells.* J. Cell Biol., 1980. **86**(3): p. 885-890.

25. FitzHarris, G. and J.M. Baltz, *Regulation of intracellular pH during oocyte growth and maturation in mammals.* Reproduction, 2009. **138**(4): p. 619-627.

26. Ruoff, P. and C. Lillo, *Evidence for increased proton dissociation in low-activity forms of dephosphorylated squash-leaf nitrate reductase.* Biophysical Chemistry, 1997. **67**(1-3): p. 59-64.

27. Kaiser, W.M. and S.C. Huber, *Correlation between apparent activation state of nitrate reductase (NR), NR hysteresis and degradation of NR protein.* J. Exp. Bot., 1997. **48**(7): p. 1367-1374.

28. Huber, S.C. and J.L. Huber, *Metabolic activators of spinach leaf nitrate reductase: Effects on enzymatic activity and dephosphorylation by endogenous phosphatases.* Planta, 1995. **196**(1): p. 180-189.

29. EchevarrÌa, C., S.G. Maurino, and J.M. Maldonado, *Reversible inactivation of maize leaf nitrate reductase.* Phytochemistry, 1984. **23**(10): p. 2155-2158.

30. Behzadi, A., R. Hatleskog, and P. Ruoff, *Hysteretic enzyme adaptation to environmental pH: change in storage pH of alkaline phosphatase leads to a pH-optimum in the opposite direction to the applied change.* Biophys. Chem., 1999. **77**: p. 99-109.

31. Kroh, H.K., P. Panizzi, and P.E. Bock, *Von Willebrand factor-binding protein is a hysteretic conformational activator of prothrombin.* Proc Natl Acad Sci U S A, 2009. **106**(19): p. 7786-7791.

32. Tyson, J.J., K.C. Chen, and B. Novak, *Sniffers, buzzers, toggles and blinkers: dynamics of regulatory and signaling pathways in the cell.* Curr. Opin. Cell Biol., 2003. **15**(2): p. 221-231.

33. Hand, S.C. and J.F. Carpenter, *pH-Induced Metabolic Transitions in Artemia Embryos Mediated by a Novel Hysteretic Trehalase.* Science, 1986. **232**(4757): p. 1535-1537.

34. Shen-Orr, S.S., et al., *Network motifs in the transcriptional regulation network of Escherichia coli.* Nat Genet, 2002. **31**(1): p. 64-68.

35. Frauenfelder, H., et al., *A unified model of protein dynamics.* Proc. Natl. Acad. Sci. USA, 2009. **106**(13): p. 5129-5134.

36. Sigal, A., et al., *Variability and memory of protein levels in human cells.* Nature, 2006. **444**(7119): p. 643-646.

37. Spencer, S.L., et al., *Non-genetic origins of cell-to-cell variability in TRAIL-induced apoptosis.* Nature, 2009. **459**(7245): p. 428-432.

38. Wu, Z., et al., *Amplification and Detection of Single-Molecule Conformational Fluctuation through a Protein Interaction Network with Bimodal Distributions.* J. Phys. Chem. B, 2009. **113**(36): p. 12375-12381.

39. Chang, H.H., et al., *Transcriptome-wide noise controls lineage choice in mammalian progenitor cells.* Nature, 2008. **453**(7194): p. 544-547.

40. Ricard, J. and A. Cornish-Bowden, *Co-operative and allosteric enzymes: 20 years on.* Eur. J. Biochem., 1987. **166**(2): p. 255-272.

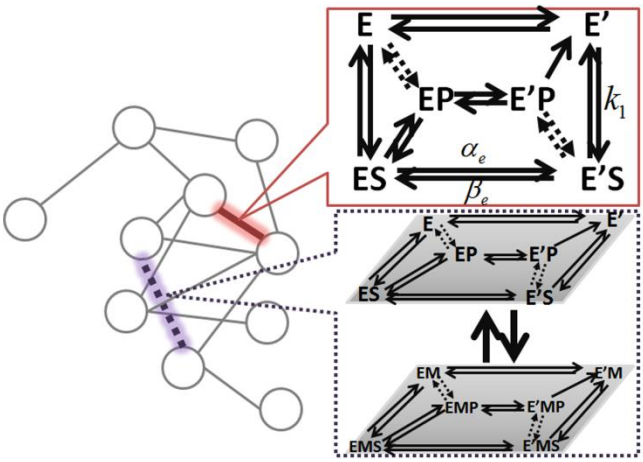

Figure 5.1 Edges in biological regulatory networks representing enzymatic reactions may have complex dynamics for substrate-to-product transition (a) and regulation by modulating molecules M (b).E and E' refer to different conformations of the same enzyme. S, P, and M are substrate, product, and regulator, respectively. These two models are adapted from [16, 40].

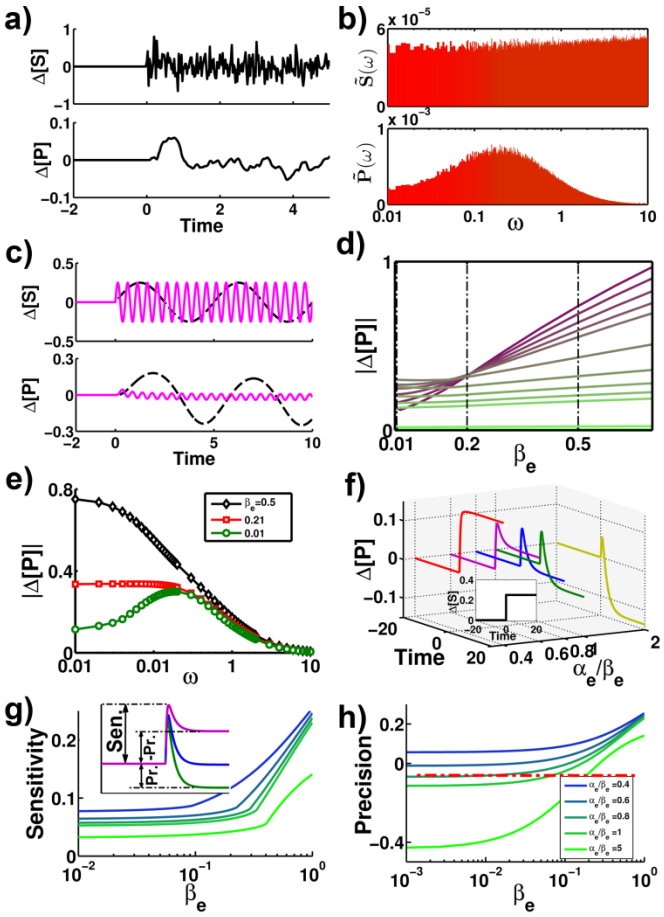

Figure 5.2 Enzyme with slow conformational change (motif a in Figure 5.1 without the dashed connections for simplicity) may serve as noise filter and adaptive motif. a) A typical trajectory of substrate and product derivation from their steady state values with fluctuations. b) Power spectrum of the substrate and product fluctuations. (c) Mono frequency analysis of fluctuation buffer with slow enzyme conformational changes. Upper panel: regulatory signal. Lower Panel: downstream product response. (dashed line: low frequency, solid line: high frequency). The enzyme conformational transaction rate $\alpha = 0.01$. (d) The product oscillation amplitude P_m under sinuous substrate concentration fluctuations versus the transition rate constant between ES and E'S, β_e. The substrate oscillation frequency takes value ω=0.02, 0.04, 0.06, 0.08, 0.1, 0.2, 0.4, 0.6, 0.8, 1 from dark to light lines. (e) The product oscillation amplitude versus ω for the three β_e values shown in panel c. (f) Trajectories of product

response upon sudden change of substrate concentration (inserted plot) under different values of α_e / β_e (the ratio between transition rate constants ES→E'S and E'S→ES). Enzyme fluctuation can generate positive (red line), adaptive (purple, blue and green lines), and negative responses (yellow line). (g)-(h): sensitivity and precision (defined by the inserted plot) of the response curves in panel h versus β_e at a given value of α_e / β_e.

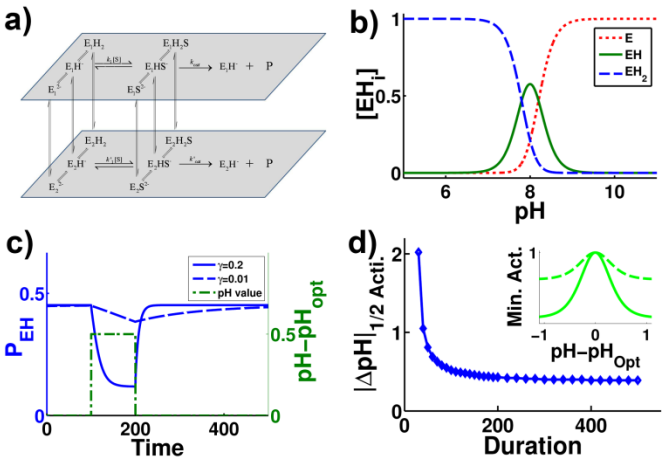

Figure 5.3 Slow conformational change allows enzymes to buffer pH fluctuations. Model parameters are chosen to resemble alkaline phosphatase. (a) A simple diprotonic model with conformational change. (b) The steady state percentage of the active form EH has an optimum pH value. (c) Change of P_{EH} for an enzyme with fast (solid line) and slow (dashed line) conformational change Υ upon sudden and transient pH change (dot dashed line). The steady state P_{EH} is normalized to 1 here. (d) pH change needed for $\Delta P_{EH} = ½$ in panel c versus duration of the pH change. The inserted plot is ΔP_{EH} versus $\Delta pH = pH - pH_{opt}$ with sustained (solid line) and transient (dashed line) pH fluctuation.

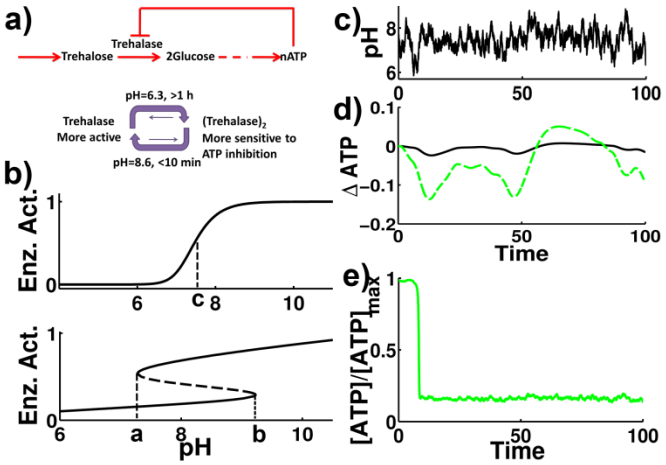

Figure 5.4 Model study of the Brine Shrimp Embryo metabolic regulatory network. (a) Basic network. (b) Two typical response curves for biological systems switching between two distinct states. (c) pH fluctuations lead to different ATP production fluctuation patterns with a sigmoidal response curve (d), (solid line: slow Trehalase conformational change; dashed line: fast conformational change) and hypothetical bistable response curve (e).

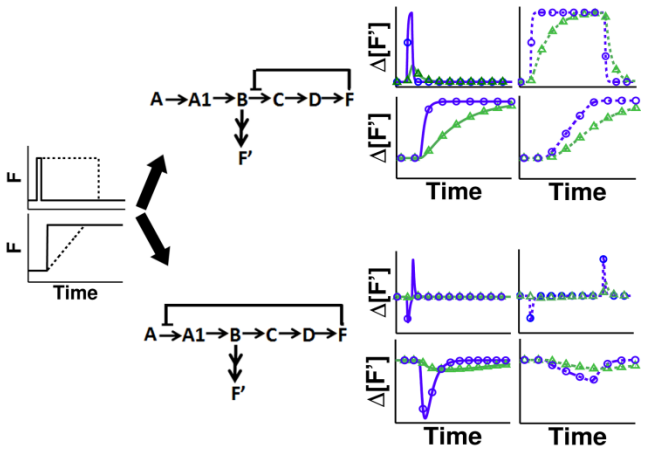

Figure 5.5 Dynamics of metabolic networks with end-product inhibition. Left: Different patterns of introduced end product F fluctuations. Middle: Two typical metabolic networks. The regulatory enzymes are modulated by end product F and are hysteretic. Right: Induced F' fluctuations. Curves with circles and triangles correspond to results with fast and slow enzyme

conformational changes, respectively. Solid and dashed curves refer to F' fluctuations induced by the corresponding F fluctuations shown in the left panel.

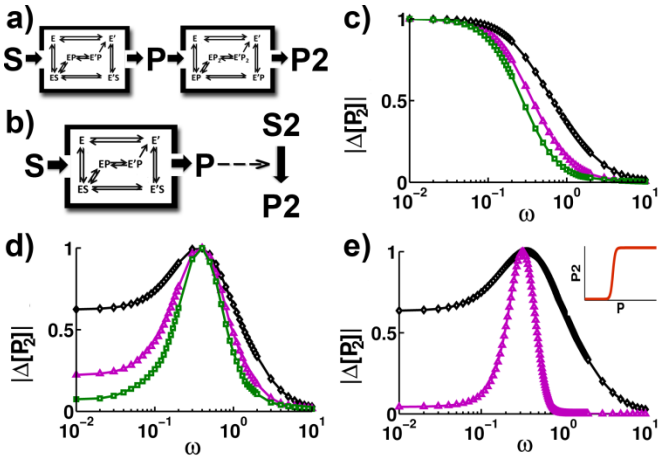

Figure 5.6 Construct networks with hysteretic enzymes. (a) Cascade of enzymatic reactions. (b)The product of reaction 1 with hysteretic enzyme regulates reaction 2 sigmoidally. (c) Normalized ΔP_2 versus frequency ω of [S] oscillations for the cascade with 1 (diamond), 2 (triangle), and 3 (square) enzymatic reactions. (d) Same as c except with different parameters to have resonance. (e) ΔP_2 vs ω for network in b.

i. Supporting Information

Model details and parameters

Fig. 5.2 in the main context investigates the behaviors of motif in Fig. 5.1a. The detailed ordinary differential equations (ODEs) describing the motif are

$$\frac{d[E]}{dt} = k_{ES\_S}[ES] - k_{S\_ES}[E][S] + \beta[E'] - \alpha[E];$$
$$\frac{d[E']}{dt} = k_{E'S\_S}[E'S] - k_1[E'][S] - \beta[E'] + \alpha[E];$$
$$\frac{d[P]}{dt} = k_{E'P\_P}[E'P] - k_{out}[P];$$
$$\frac{d[ES]}{dt} = -k_{ES\_S}[ES] + k_{S\_ES}[S][E] + \beta_e[E'S] - \alpha_e[ES] + k_{EP\_ES}[EP] - k_{ES\_EP}[ES]; \quad \text{(S1)}$$
$$\frac{d[EP]}{dt} = -k_{EP\_ES}[EP] + k_{ES\_EP}[ES] - k_{EP\_E'P}[EP] + k_{E'P\_EP}[E'P];$$
$$\frac{d[E'P]}{dt} = k_{EP\_E'P}[EP] - k_{E'P\_EP}[E'P] - k_{E'P\_P}[E'P];$$
$$[E'S] = [E_{total}] - [E] - [E'] - [ES] - [EP] - [E'P];$$

where the parameters except the ones prescribed in Fig. 5.2 are set as $\beta = 1$, $\alpha = 1$, k_{ES_S}=10, k_{S_ES}=10, $k_{E'S\_S}$=5, $k_{E'P\_P}$=20, $k_{EP\_E'P}$=10, $k_{E'P\_EP}$=10, k_{ES_EP}=10, k_{EP_ES}=10, k_{out}=0.5, E_{total}=10.

For the stochastic simulation (Fig. 5.2a-b), [S] can be written as

$$\frac{d[S]}{dt} = -a([S] - [S_0]) + b\zeta(t); \quad \text{(S2)}$$

where (t) refers to white noise drawn from a normal Gaussian distribution, and < (t) (t')> = (t-t'). For monochromatic sinuous [S] fluctuations, we have

$$[S] = [S_0] + \frac{1}{2} A\sin(2\pi\omega(t - t_0)) \quad \text{(S3)}$$

The value of A and ω can be read directly from Fig. 5.2c-e.

For the metabolic networks mentioned in Fig. 5.5, they are abstracted from Threonine (F)/Lysin (F') synthesis pathway. The equations to describe the network2 (Lower Panel) in Fig. 5.5 can be written as

$d[A]/dt = - v_{EAA1I} - v_{EAA1III} + v_{In1}$

$d[A1]/dt = v_{EAA1I} + v_{EAA1III} - v_{EA1B}$

$d[B]/dt = v_{EA1B} - v_{EBCI} - v_{EBCII} - v_{EBF'}$

$d[C]/dt = v_{EBCI} + v_{EBCII} - v_{ECD}$

$d[D]/dt = v_{ECD} - v_{EDF}$

$d[F']/dt = v_{EBF'} - v_{Out2}$

$d[EAA1I]/dt = -k_a*[EAA1I] + k_b*[EAA1III] + k_{fb}*[EAA1I\_F] - k_f*[EAA1I]*[F]^4$

$d[EAA1I\_[F]]/dt = -k_{fb}*[EAA1I\_F] + k_f*[EAA1I]*[F]^4$

$d[EAA1III]/dt = k_a*[EAA1I] - k_b*[EAA1III] + k_{fb3}*[EAA1III\_F] - k_{f3}*[EAA1III]*[F]^4$

$v_{[EAA1I]} = k_{[EAA1I]} * [EAA1I]_t * ([A] / (K_{[A]1} + [A]))$

$v_{[EAA1III]} = k_{[EAA1III]} * [EAA1III]_t * [A] / (K_{[A]3} + [A])$

$v_{[EA1B]} = V_{m[EA1B]} * [A1] / (K_{[A1]} + [A1])$

$v_{[EBCI]} = k_{[EBCI]} * [EBCI]_t * [B] / (K_{[B]1} + [B])$

$v_{[EBCII]} = k_{[EBCII]} * [EBCII]_t * [B] / (K_{[B]2} + [B])$

$v_{[ECD]} = V_{m[ECD]} * [C] / (K_{[C]} + [C])$

$v_{[EDF]} = V_{m[EDF]} * [D] / (K_{[D]} + [D])$

$v_{EBF'} = V_{mE[F']} * [B] / (K[F'] + [B])$

$v_{Out2} = (k_{Out2}) * [F']/(K_{Mout2} + [F'])$

$v_{In1} = k_{In1}$

$[EBCII]_t = [EBC]_t - [EBCI] - [EBCI\_F]$

$[EBCI]_t = [EBCI] + [EBCI\_F]$

$[EBCII\_Thr] = [EBC]_t - [EBCI] - [EBCI\_F] - [EBCII]$

$[EAA1III]_t = [EAA1]_t - [EAA1I] - [EAA1I\_F]$

$[EAA1I]_t = [EAA1I] + [EAA1I\_F]$

$[EAA1III\_F] = [EAA1]_t - [EAA1I] - [EAA1I\_F] - [EAA1III]$

where $k_f=100$; $k_{f3}=100$; $k_{eb}=1$; $k_e=1$; $k_{e3}=0.1$; $k_b=k_a*k_{eb}$; $k_{fb}=k_f*k_e$; $k_{fb3}=k_{f3}*k_{e3}$; $k_{[EAA1]I}=0.6$; $k_{[EAA1]III}=0.06$; $k_{[EBC]I}=0.4$; $k_{[EBC]II}=0.04$; $V_{m[EA1B]}=0.25$; $V_{m[ECD]}=0.4$; $V_{m[EDF]}=0.2$; $V_{mE[F']}=0.4$; $K_{[A]1}=0.3$; $K_{[A]3}=0.3$; $K_{[A1]}=0.2$; $K_{[B]1}=0.25$; $K_{[B]2}=0.25$; $K_{[C]}=0.1$; $K_{[D]}=0.3$; $K_{[F']}=0.5$; $k_{Out1}=0.4$; $K_{Mout1}=4$; $k_{Out2}=0.6$; $K_{Mout2}=4$; $k_{In1}=0.1$; ka (Enzyme conformation change rate) is changeable in the model. [F] is fluctuating as indicated in the Fig. 5.5.

The ODEs of other networks mentioned in the main context can be written in similar fashion based on the motifs given in Figures 3-6. All simulations are performed with Matlab. The codes are available upon request.

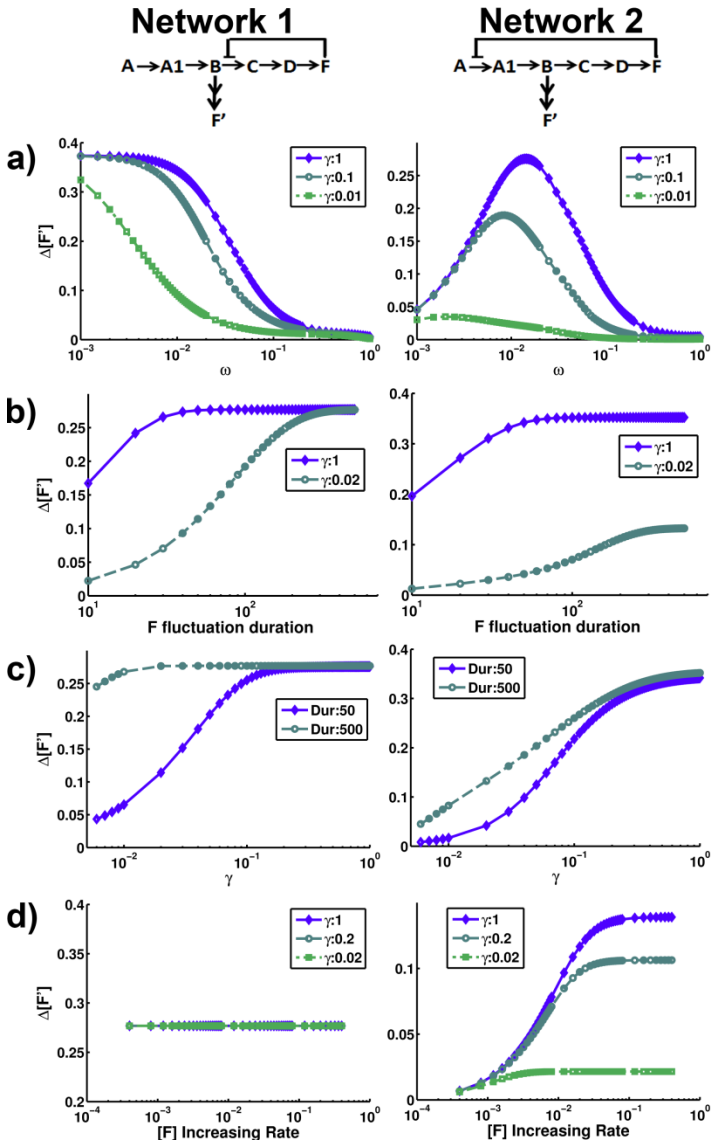

Figure 5.S1 **Detailed signal dependence of the two metabolic networks in Fig 5.** (a) The dependence of F' variation on F fluctuation frequency shows high frequency filtering with network 1, and resonance with network 2. (b) $\Delta[F']$ versus F fluctuation duration at different enzyme conformational change rates γ. With network 1, $\Delta[F']$ with different values converge to the same value upon increasing the F fluctuation duration. With network 2, $\Delta[F']$ is larger with larger γ values . (c) $\Delta[F']$ versus γ at different F fluctuation duration. With network 1, the $\Delta[F']$ value is less sensitive to γ with more sustained F fluctuations. With network 2, the $\Delta[F']$ value is

sensitive to γ with both short and more sustained F fluctuations. (d) $\Delta[F']$ versus the increasing rate of F fluctuations. Network 2, but not network 1, response to the increasing rate of F changes.

Chapter 6

Amplification and detection of single molecule conformational fluctuation through a protein interaction network with bimodal distributions

Zhanghan Wu [1], Vlad Elgart [1], Hong Qian [2], Jianhua Xing [1]*

[1]Department of Biological Sciences, Virginia Polytechnic Institute and State University, Blacksburg, VA and

[2]Department of Applied Mathematics, University of Washington, Seattle, WA

a. Abstract

A protein undergoes conformational dynamics with multiple time scales, which results in fluctuating enzyme activities. Recent studies in single molecule enzymology have observe this “age-old” dynamic disorder phenomenon directly. However, the single molecule technique has its limitation. To be able to observe this molecular effect with real biochemical functions *in situ*, we propose to couple the fluctuations in enzymatic activity to noise propagations in small protein interaction networks such as zeroth order ultra-sensitive phosphorylation-dephosphorylation cycle. We showed that enzyme fluctuations could indeed be amplified by orders of magnitude into fluctuations in the level of substrate phosphorylation | a quantity widely interested in cellular biology. Enzyme conformational fluctuations sufficiently slower than the catalytic reaction turnover rate result in a bimodal concentration distribution of the phosphorylated substrate. In return, this network amplified single enzyme fluctuation can be used as a novel biochemical “reporter” for measuring single enzyme conformational fluctuation rates.

b. Introduction

The dynamics of an enzyme is usually characterized by a rate constant describing its catalytic capacity, which is a standard practice on studying dynamics of enzymes and enzyme-involved networks. Recent advances in single molecule techniques allow examining enzyme activities at single molecule levels [1-13]. It is found that the rate "constant" of an enzyme is in general a broad distribution. Physically, it is because the enzyme conformation is under constant fluctuation at varying time scales [13, 14]. Single molecule techniques can measure the instant rate constants at a given conformation. The single molecule results are consistent with extensive early biochemistry and biophysics studies. Biochemists have long noticed that protein conformational fluctuations (which can be in the time scale from subsecond to minutes and even hours) can be comparable and even slower than the corresponding chemical reactions (usually in the range of subsecond) [15]. Slow conformational motions result in hysteretic response of enzymes to concentration changes of regulatory molecules, and cooperative dependence on substrate concentrations [15-18]. In physical chemistry, the term dynamic disorder is used for the phenomenon that the rate of a process may be stochastically time-dependent [19]. Extensive experimental and theoretical studies exist since the pioneering work of Frauenfelder and coworkers [20]. Allosteric enzymes can be viewed as another class of examples. According to the classical Monod-Wyman-Changeux model and recent population shift model, an allosteric enzyme coexists in more than one conformation [21, 22]. Recent experiments also show that the conformational transition of an allosteric enzyme happens in micro- to millisecond time scale or longer [23]. Xing proposed that in general internal conformational change

should be considered on describing enzymatic reactions, and it may have possible implication on allosteric regulation mechanism [24]. Wei *et. al* also suggested a similar formalism for describing enzymatic reactions [25]. Current single molecule enzymology studies focus on metabolic enzymes. It remains an important unanswered question if dynamic disorder is a general phenomenon for enzymes, e.g., the enzymes involved in signal transduction. While the technique reveals important information, the single molecule approach also has strict requirement on the system to achieve single molecule sensitivity, which limits its usage for quick and large scale scanning of enzymes.

In this work we discuss an idea of coupling molecular enzymatic conformational fluctuations to the dynamics of small protein interaction networks. Specifically we will examine a phosphorylation/dephosphorylation cycle (PdPC) [26]. Our analysis will be applicable to other mathematically equivalent systems, such as GTP-associated cycle, or more general a system involving two enzymes/enzyme complexes with opposing functions on a substrate. As an example for the latter, the system can be an enzymatic reaction consuming ATP hydrolysis (*e.g.*, a protein motor) coupled to a ATP regeneration system--in this case ATP is the substrate. The PdPC is a basic functional module for a wide variety of cellular communications and control processes. The substrate molecules can exist in the phosphorylated and dephosphorylated form, which are catalyzed by kinase and phosphatase respectively at the expense of ATP hydrolysis. The percentage of the phophorylated substrate form depends on the ratio of kinase and phosphatase activities in a switch like manner called ultra-sensitivity. Through the PdPC, slow conformational (and thus enzymatic activity) fluctuations at the single molecule level can be amplified to fluctuations of substrate phosphorylation forms by several

orders of magnitude, and make it easier to detect. The coupling between molecular fluctuations and network fluctuations itself is an interesting biological problem. Recent studies revealed that the intrinsic/extrinsic noise, when it is introduced into the biological system, has significant influences on the behavior and sensitivity of the entire network [27-34]. Unlike the noise sources studies previously, the internal noise due to dynamic disorder shows broad time scale distributions. Its effect on network-level dynamics is not well studied [35]. We will show that a bimodal distribution of the PdPC substrate form can arise due to dynamic disorder, which may have profound biological consequences.

c. The model

A PdPC is shown in Figure 6.1a. X and X* are the unphosphorylated and phosphorylated forms of the substrate, respectively. We assume A is the phosphatase obeying normal Michaelis-Menten kinetics. The kinase E, on the other hand, can assume two conformations with different catalytic capacity. In general an enzyme can assume many different conformations. The two state model here can be viewed as coarse-graining. The set of reactions describing the system dynamics are listed below:

$$X + E_1 \underset{k_{1b}}{\overset{k_{1f}}{\rightleftharpoons}} XE_1 \underset{k_{+b}}{\overset{k_{+f}}{\rightleftharpoons}} X^* + E_1,$$

$$X + E_2 \underset{k_{1b'}}{\overset{k_{1f'}}{\rightleftharpoons}} XE_2 \underset{k_{+b'}}{\overset{k_{+f'}}{\rightleftharpoons}} X^* + E_2,$$

$$X^* + A \underset{k_{2b}}{\overset{k_{2f}}{\rightleftharpoons}} X^* A \underset{k_{-b}}{\overset{k_{-f}}{\rightleftharpoons}} X + A,$$

$$E_1 \underset{\beta}{\overset{\alpha}{\rightleftharpoons}} E_2, E_1X \underset{\beta'}{\overset{\alpha'}{\rightleftharpoons}} E_2X.$$

To ensure proper detailed balance constraint, each pair of forward and backward reaction constants are related by the relation $\Delta\mu^0 = -k_B T \ln(k_f / k_b)$, with $\Delta\mu^0$ the standard chemical potential difference between the product(s) and the reactant(s), k_B the Boltzmann constant, T the temperature. Exceptions are the three chemical reaction steps, which we assume couple to ATP hydrolysis, and thus extra terms related to ATP hydrolysis free energy $\Delta\mu_{ATP}$ are added. we assume $\Delta\mu^0 + \Delta\mu_{ATP}/2 = -k_B T \ln(k_f / k_b)$ for each of these reactions, so one ATP molecule is consumed after one cycle. In general the conformer conversion rates $\alpha, \beta, \alpha', \beta'$ are different. For simplicity in this work, we choose $\alpha = \beta = \alpha' = \beta'$ unless specified otherwise.

Let's define the response curve of the system to be the steady-state percentage of X* as a function of the catalytic reactivity ratio between the kinase and the phosphatase ($\bar{\theta} \equiv (p_1 k_+ + p_2 k_{+'}) N_{E_t} / (k_- N_{A_t})$, where p_i is the probability for the kinase to be in conformer i), and N_{E_t} and N_{A_t} are total numbers of kinase and phosphatase molecules. At bulk concentration, for both fast and slow kinase conformational change, the response curve shows usual sigmoidal but monotonic dependence (see Figure 6.1b) [26]. Here we only consider the zero-th order regime where the total substrate concentration is much higher than that of the enzymes.

However, the situation is different for a system with small number of molecules. For simplicity let's focus on the case with one kinase molecule. Physically, suppose that

the average reactivity ratio $\bar{\theta} \sim 1$ (not necessarily exactly at 1), but the corresponding $\theta_1 \equiv k_+ / (N_{A_t} k_-) > 1$ and $\theta_2 \equiv k_{+'} / (N_{A_t} k_-) < 1$. Consequently, the substrate conversion reactions are subject to fluctuating enzyme activities, an manifestation of the molecular level dynamic disorder. Because of the ultra-sensitive nature of the PdPC, small enzyme activity fluctuation (in the vicinity of $\theta = 1$) can be amplified into large fluctuations of substrate forms (in the branches of high or low numbers of X*). The relevant time scales in the system are the average dwelling time of the kinase at the new conformation τ_K, and the average time required for the system to relax to a new steady-state substrate distribution once the kinase switches its conformation τ_S. The former is related to the conformer conversion rates. The latter is determined by the enzymatic reaction dynamics as well as the number of substrate molecules. If the kinase conformational switch is sufficiently slow ($\tau_K >> \tau_S$), so that on average for the time the kinase dwelling on each conformation, the substrate can establish the steady state corresponding to θ_i, which is peaked at either high or low N_{X^*}. Then the overall steady-state substrate distribution is a bimodal distribution, which is roughly a direct sum of these two single peaked distributions. This situation resembles the static limit of molecular disorders [19]. Increasing conformer switching rates tends to accumulate population between the two peaks, and eventually results in a single-peaked distribution ($\tau_K < \tau_S$). A critical value of α (or β) exists where $\tau_K \sim \tau_S$, and one peak of the distribution disappears. There are two sets of (τ_K, τ_S) corresponding to the transition from conformer 1 to 2, and vice versa. In principle, in the slow enzyme conform conversion regime where the substrate shows non-unimodal distribution ($\tau_K > \tau_S$), one

can extract molecular information of the enzyme fluctuations from the greatly amplified substrate fluctuations. This is the basic idea of this work.

d. Numerical studies

To test the idea, we performed stochastic simulations with the Gillespie algorithm [36] using the parameters listed in Table 6.1 and Appendix A. Figure 6.1c shows that with a single slowly converting two-state kinase, the number of X* jumps between high and low values, and shows bimodal distribution (see Figure 6.1d). Figure 6.2 gives systematic studies on this phenomenon. There exist two critical values of α, α_1, α_2. With $\alpha < (\alpha_1, \alpha_2)$, the substrate distribution has two well-separated peaks (Figure 6.2a). On increasing α, the two original peaks diminish gradually while the the region between the two peaks accumulates population to form a new peak (Figure 6.2b). The two original peaks disappear at $\alpha = \alpha_1$ and $\alpha = \alpha_2$ respectively, and eventually the distribution becomes single-peaked (Figure 6.2c-e). Figure 6.2f summarizes the above process using the distance between peaks. The results divide into three regions. The point of transition between the left and the middle regions indicates disappearance of the left peak (corresponding to Figure 6.2c). That between the middle and the right regions indicates disappearance of the right peak (corresponding to Figure 6.2d).

Figure 6.2g shows that the critical value of α decreases with the total substrate number N_{Xt}. An increased number of N_{Xt} gives a larger τ_S, which requires a larger τ_K (slower conformation conversion rate) in order to generate a multi-peaked distribution. Figure 6.2g also compares theoretical (see below) and simulated critical α values at

different values of N_{X_t}. The plot shows that the simulation results agree reasonably with the theoretical predictions, although the simulated critical α is slightly smaller than the theoretical values, which means that the peak disappears earlier on increasing fluctuation rate α. The discrepancy of the two could be due to stochasticity of enzymatic reactions, which is fully accounted for in the simulations, but neglected in the theoretical treatment. The broader distribution leads to an earlier disappearance of peaks. This argument is supported by the fact that the difference between theoretical and simulated critical α is getting closer when the substrate number becomes larger, so fluctuations due to enzymatic reactions are further suppressed.

In the above discussions, we focus on a system with a single copy of the two-state kinase molecule. Appendix B shows that a simulation result with multi-state model gives similar behaviors. Figure 6.3a shows that with multiple copies of enzymes, the substrate distribution of a PdPC can show similar transition from bimodal (or multi-modal in some cases) to unimodal behaviors, but the critical values of α are smaller (corresponding to slower conformational change) than those for the single kinase case . In these calculations, we scale the system proportionally to keep all the concentrations constant.

Possible biological significances of the bimodal distributions will be discussed below. Here we propose that additionally one can use the phenomenon to extract single molecule fluctuation information, especially the conformer conversion rates. Conventionally the information is obtained through single molecule experiments [6, 13]. For simplicity here we focus on the single enzyme case only. Suppose that an enzyme

fluctuates slowly between different conformers, and one can couple a single molecule enzyme with a PdPC (or a similar system) with fast enzymatic kinetics. Then the conformational fluctuation dynamics at the single molecule level will be amplified to the substrate form fluctuations by orders of magnitude. Figure 6.4 gives the result of such an experiment simulated by computer. The trajectory clearly shows two states. To estimate the time the system dwelling on each state, we define the starting and ending dwelling time as the first time the number of substrate molecules in the X* form reaches the peak value of N_{X^*} distribution corresponding to that state in the forward and backward direction of the trajectory (see Figure 6.4a). The above algorithm of finding the dwelling time may miss those with very short dwelling time so the substrate may not have enough time to reach the peak value, as seen in the trajectory. Nevertheless, the obtained dwelling time distributions are well fitted by exponential functions. The exponents give the values of α and β, in this case $\sim 0.8\times 10^{-3}$ for both of them, which are good estimations of the true value 10^{-3}.

e. Theoretical analysis

Analytical estimate of the critical points

Here we provide quantitative analysis of the above time scale argument. Let's define

$$g_1 = -\frac{k_+[E_t]x}{K_{M+}+x}, h_1 = \frac{k_-[A_t]([X]_t - x}{K_{M-}+[X_t]-x}, \quad (1)$$

and similar expression for the case that the kinase assumes conformer 2 except k_+ is replaced by $k_{+'}$. Then the kinetics of a PdPC with one two-state kinase molecule is governed by a set of Liouville equations under the Langevin dynamics approximation [19, 37, 38],

$$\partial_t \rho_1(x) = \frac{1}{2\Omega}\partial_{xx}\left[(g_1 + h_1)\rho_1(x)\right]$$

$$-\partial_x\left[(-g_1 + h_1)\rho_1(x)\right] - \alpha\rho_1(x) + \beta\rho_2(x), \tag{2}$$

$$\partial_t \rho_2(x) = \frac{1}{2\Omega}\partial_{xx}\left[(g_2 + h_2)\rho_2(x)\right]$$

$$-\partial_x\left[(-g_2 + h_2)\rho_2(x)\right] + \alpha\rho_1(x) - \beta\rho_2(x), \tag{3}$$

where $\rho_i(x)$ is the probability density to find the system at kinase confomer i and the number of substrate form X being x, Ω is the system volume. For mathematical simplicity in the following derivations, we assume that for a given kinase conformation, the substrate dynamics can be described continuously and deterministically. This approximation is partially justified by the relative large number of substrates. Then one can drop the diffusion term containing Ω, and solve the above equations analytically (see Appendix C). The theoretical steady state solutions of $\rho(x) = \rho_1(x) + \rho_2(x)$ are also plotted in Figure 6.2. Since in our analysis we neglected stochasticity of enzyme reactions due to the finite number of substrates, the analytical solutions are bound by the two roots (x_1, x_2) of the equations,

$$f_1(x_1) = 0,\ f_2(x_2) = 0. \tag{4}$$

In the case of fast switching rates, the solutions vanish at the turning points (x_1, x_2), and become identically zeros outside of the interval $[x_1, x_2]$. Physically it means that the enzyme equilibrates quickly and the rest of the system `feels' only averaged reactivity of two enzyme's states.

In the regime of slow switching rates, the steady state solutions $\rho_1(x)$ and $\rho_1(x)$ have two integratable singular points at (x_1, x_2). The solutions diverge at these points (although integration of ρ_i over x is still finite). Of course, the neglected `diffusion' term due to substrate fluctuations becomes important in this situation. This term smears the singularities at the turning points (x_1, x_2). Kepler $et \quad al.$ noticed similar behaviors in their simulation results. However, in order to estimate the critical values of the switching rates α_c and β_c, which correspond to transition between unimodal and bimodal distribution, the set of equations Eq. (2) and Eq. (3) are sufficient.

Even within this approximation the analytical prediction of the transition points agrees well with the simulation results. The conditions for disappearance of these two single points are,

$$\alpha \geq \alpha_c = \partial_x f_1(x_1), \beta \geq \beta_c = \partial_x f_2(x_2). \tag{5}$$

Note that $1/\alpha$ (or $1/\beta$) is the average dwelling time of an enzyme configuration τ_K, and $1/\alpha_c$ (or $1/\beta_c$) is the relaxation time after the system linearly deviates from the single conformer steady state (at x_1 or x_2), which are τ_S in the previous discussions. Figure 6.2f & g show good agreement between the critical points obtained by simulation

and by Eq. (5) . The agreement becomes better for larger number of substrates, suggesting that the discrepancy between the simulated and theoretical results are due to neglecting substrate fluctuations in the theoretical treatment.

Multi-enzyme systems

For N independent two state kinases the probability to have k kinases in conformer 1 has following binomial distribution

$$\pi(k,t) = \binom{k}{N} p_1^k (1-p_1)^{N-k}, \tag{6}$$

where we defined

$$p_1(t) = p_1^s - (p_1^s - p_1^i)e^{-(\alpha+\beta)t}, \tag{7}$$

where p_1^i is initial probability to be in the state 1, and the steady state probability p_1^s is given by $p_1 = \beta/(\alpha+\beta)$.

Note that binomial distribution Eq. (6) becomes normal in the case $N \to \infty$. Therefore, in this limit one can represent overall concentration of the enzymes as (cf. with equation S8 in [29])

$$E_t = E + \xi(t), \tag{8}$$

where $\xi(t)$ is Gaussian noise with correlation function decaying *exponentially* fast, see Eq. (7) . Hence, only when the switching rates α and β are fast (*i.e.*, no dynamic disorder) the white noise approximation used in reference [29] is expected to work well,

since in this case exponential decay of the correlation function can be safely replaced by δ-function. Recently Warmflash *et.al* also discussed the legitimacy of using the δ-function approximation [39].

Let us calculate noise-noise correlator explicitly. One gets

$$\langle n(t)n(t')\rangle \equiv \sum_{n,n'} nn' P(n,t \mid n',t')P(n',t'), \tag{9}$$

where $P(n,t \mid n',t')$ is the conditional probability to have n enzymes in conformer 1 at time t, provided that at time t' the number of enzymes in conformer 1 is *exactly* n'. The second term in the product, $P(n',t')$, is the probability to have n' enzymes in conformer 1 at time t' and it depends on initial conditions. However, for late times $t > t' \gg (\alpha+\beta)^{-1}$ it can be safely replaced by the steady state distribution:

$$P(n',t') \sim \pi_s(n'). \tag{10}$$

As for conditional probability, we derive

$$P(n,t \mid n',t') = \pi(n,t-t'), \tag{11}$$

where dependence on the number n' comes from the initial conditions in Eq. (7) :

$$p_1^i = 2^{-N}\binom{n'}{N}. \tag{12}$$

It means that $p_1(t-t')$ in Eq. (7) depends implicitly on n', and hence will be defined as $p_1(n',t-t')$. After some algebra we get

$$\langle n(t)n(t')\rangle = N\sum_{n'} n' p_1(n', t-t')\binom{n'}{N}(p_1^s)^{n'}(1-p_1^s)^{N-n'}. \quad (13)$$

It is easy to check that the first term in the expression for $p_1(n', t-t')$, namely p_1^s, adds the contribution $\langle n(t)\rangle\langle n(t')\rangle$ for a late times. Therefore, one obtains a two time correlation function

$$\langle n(t)n(t')\rangle - \langle n(t)\rangle\langle n(t')\rangle = \sigma^2 e^{-(\alpha+\beta)(t-t')}, \quad (14)$$

exponentially decaying in time with correlation strength σ that can be explicitly obtained from the Eq. (13) .

f. Discussion and concluding remarks

Slow conformational fluctuations have been suggested to be general properties of proteins, and result in dynamic disorder. However, so far only metabolic enzymes have been directly examined at the single molecule level. If demonstrated, the existence of dynamic disorder in general may greatly modify our understanding of dynamics of biological networks (e.g., signal transduction networks). It provides a new source of in general non-white noises. In this work, we exploit the ultrasensitivity of a PdPC (or a similar system as discussed previously) to amplify molecular level slow conformational fluctuations. The method may be used experimentally for quick screening and qualitative/semi-quantitative estimation of molecular fluctuations in signal transduction networks. Here we propose a possible experimental setup. One adds one or a few kinases, corresponding phosphatase (with its amount adjusted so the average activity ratio $\bar{\theta} \sim 1$), a relatively large amount of substrate molecules, and ATP regeneration

system in an isolated chamber. Experimentally one may consider the micro-fabrication technique produced high density small reaction chambers used previously in single molecule protein motor and enzyme studies [7, 40]. Containers may stochastically contain different number of molecules of the kinase, phosphatase, with some of them giving the desired $\bar{\theta} \sim 1$. Monitoring substrate fluctuations ($e.g.$, through fluorescence) may reveal information about molecular level fluctuations. In general protein fluctuation is more complicated than the two-state model used here. The latter should be viewed as coarse-grained model. In this work for simplicity we didn't consider possible conformational fluctuations of the phosphatase and even the substrate (which may act as enzymes for other reactions). Including these possibilities make the analysis more difficult, but won't change the conclusion that molecular level fluctuations can couple to fluctuations at network levels and be amplified by the latter.

There are several studies on systems showing stochasticity induced bimodal distribution without deterministic counterpart. [29, 37, 41-45] In eukaryotic transcription, a gene may be turned on and off through binding and dissociation of a regulating protein, which may result in bimodal distribution of the expressed protein level. The process is mathematically equivalent to the problem we discussed here. Physically the mechanism of generating a bimodal distribution is trivial. The system (PdPC) has a fluctuating parameter, the ratio of the overall enzyme activity θ (not $\bar{\theta}$). When the parameter fluctuates sufficiently slow, the distribution is approximately a mixture of localized distributions corresponding to different parameter values, and thus may have more than one peak. This situation is fundamentally different from macroscopic bistable systems, which have more than one steady state for a given set of parameters, and

usually some feedback mechanism is involved. Possible biological significances of a network generating bimodal distributions without deterministic counterpart has been suggested in the literature [29, 41, 43]. It remains to be examined whether the mechanism discussed in this work is biologically relevant, or reversely evolution has selected signal transduction proteins showing minimal dynamic disorder [35]. As shown in Figure 6.2g and Figure 6.3, with fixed enzyme molecular property, a system reduces to unimodal distributions on increasing the system size. Therefore the mechanism of dynamic disorder induced bimodal distribution plays a significant role only for small sized systems. We want to point out that Morishita $et.al.$ [46] has theoretically suggested that signal transduction cascades have optimal performance with only ~ 50 copies per specie, which makes the dynamic disorder mechanism plausible. In a real system it is more likely that noises arising from dynamic disorder, which has broad time-scale distribution, will couple with sources from other processes, such as enzyme synthesis and degradation, and may result in complex dynamic behaviors. Therefore physical chemistry studies of molecular level protein dynamics may provide important and necessary information for understanding cellular level dynamics.

g. Appendices

Appendix.A

Here we show how we make connections between the equations for bulk analysis and the ones for stochastic simulations with molecular number. For example, if we have a reaction

$$X + E_1 \underset{k_{1b}^0}{\overset{k_{1f}^0}{\rightleftharpoons}} XE_1,$$

we can write down the ODE equations for this reaction

$$\frac{d[XE_1]}{dt} = k_{1f}^0[X][E_1] - k_{1b}^0[XE_1].$$

First of all, we choose $1/k_{-f}$ as our time unit, where k_{-f} is the rate constant for the backward enzymatic step. Then,

$$\frac{d[XE_1]}{dt} = k_{1f}[X][E_1] - k_{1b}[XE_1].$$

with $k_{1f} = k_{1f}^0 / k_{-f}$, $k_{1b} = k_{1b}^0 / k_{-f}$. If we want to deal with variables in the unit of molecular numbers instead of concentration, we then have

$$\frac{d\left(\frac{N_{XE_1}}{N_A V_0}\right)}{dt} = k_{1f}\frac{N_X}{N_A V_0}\frac{N_{E_1}}{N_A V_0} - k_{1b}\frac{N_{XE_1}}{N_A V_0}$$

where N_A is Avogadro constant. V_0 is the volume of the system. We can further simplify the expression,

$$\frac{dN_{XE_1}}{dt} = k_{1f}\frac{N_X N_{E_1}}{N_A V_0} - k_{1b}N_{XE_1}$$

In all of our simulations, we kept a constant value for the substrate concentration $N_{X_t}/(N_A V_0) = 1$. Then,

$$\frac{dN_{XE_1}}{dt} = \frac{k_{1f}}{N_{X_t}} N_X N_{E_1} - k_{1b} N_{XE_1}$$

Appendix.B: Multi-state enzyme fluctuation

In general, an enzyme fluctuates continuously along conformational coordinates. One should consider the two-state model discussed in the main text as a coarse-grained model. Here we will use a more complicated model to show that our main conclusions still hold in general case. We consider an enzyme diffuse slowly along a harmonic potential of coordinate x, $G(x) = x^2$, where we have chose the units so $G = 1k_BT$ at $x = 1$. Motion along the conformational coordinate couples to the enzymatic reaction rate constants with an exponential factor $k_{+f} = k_{+f}^0 \exp(\lambda x)$, where $\lambda = -0.5$. One specific example is that x is the donor-acceptor distance for an electron-transfer reaction. We model the diffusion as hopping among 10 discrete states. The conversion rate constant between enzyme conformations α_i is at 10^{-2}. The backward rate constant is then determined by the detailed balance requirement $\beta_i = \alpha_i \exp(-(x_i^2 - x_{i-1}^2)/k_BT)$. Other parameters are the same as in the 2-state enzyme simulations. The reactions are listed below,

$$X + E_1 \underset{k_{1b}}{\overset{k_{1f}}{\rightleftharpoons}} XE_1 \underset{k_{+1b}}{\overset{k_{+1f}}{\rightleftharpoons}} X^* + E_1,$$

$$X + E_2 \underset{k_{2b}}{\overset{k_{2f}}{\rightleftharpoons}} XE_2 \underset{k_{+2b}}{\overset{k_{+2f}}{\rightleftharpoons}} X^* + E_2,$$

.....

$$X + E_{m-1} \underset{k_{(m-1)b}}{\overset{k_{(m-1)f}}{\rightleftharpoons}} XE_{m-1} \underset{k_{+(m-1)b}}{\overset{k_{+(m-1)f}}{\rightleftharpoons}} X^* + E_{m-1},$$

$$X + E_m \underset{k_{mb}}{\overset{k_{mf}}{\rightleftharpoons}} XE_m \underset{k_{+mb}}{\overset{k_{+mf}}{\rightleftharpoons}} X^* + E_m,$$

$$X^* + A \underset{k_{ab}}{\overset{k_{af}}{\rightleftharpoons}} X^* A \underset{k_{-b}}{\overset{k_{-f}}{\rightleftharpoons}} X + A,$$

$$E_1 \underset{\beta_1}{\overset{\alpha_1}{\rightleftharpoons}} E_2 \underset{\beta_2}{\overset{\alpha_2}{\rightleftharpoons}} ..... \underset{\beta_{m-2}}{\overset{\alpha_{m-2}}{\rightleftharpoons}} E_{m-1} \underset{\beta_{m-1}}{\overset{\alpha_{m-1}}{\rightleftharpoons}} E_m,$$

$$E_1 X \underset{\beta_{1'}}{\overset{\alpha_{1'}}{\rightleftharpoons}} E_2 X \underset{\beta_{2'}}{\overset{\alpha_{2'}}{\rightleftharpoons}} ..... \underset{\beta_{m-2}'}{\overset{\alpha_{m-2}'}{\rightleftharpoons}} E_{m-1} X \underset{\beta_{m-1}'}{\overset{\alpha_{m-1}'}{\rightleftharpoons}} E_m X.$$

Figure 6.5 shows that the reactant X shows a bimodal distribution if the enzymatic conformational fluctuation is slow. This result reiterates our suggestion that the ultrasensitive network amplifies small enzymatic activity fluctuations into large substrate number fluctuations.

Appendix.C

By omitting the diffusion terms in the Eq. (2) and Eq. (3) one derives for steady state:

$$\partial_x \left[f_1(x)\rho_1 \right] = \alpha\rho_1 - \beta\rho_2, \tag{15}$$

$$f_1(x)\rho_1 + f_2(x)\rho_2 = \text{const.} \tag{16}$$

For very fast switching rates α and β we expect an unimodal distribution centered somewhere in between two `turning' points x_1 and x_2, see Eq. (4) . Therefore, the steady state solution should vanish at these points and be identically zero outside an interval $[x_2, x_1]$.

In order to satisfy these boundary conditions, one has to set a constant in Eq. (16) to be zero. Hence, we obtain

$$\partial_x \left[f_1(x)\rho_1 \right] = \left[\alpha + \beta \frac{f_1(x)}{f_2(x)} \right] \rho_1. \tag{17}$$

The solution of the Eq. (17) depends, of course, on particular choice of the function $f(x)$. However, it is guaranteed that there is an *unique* root of the function $f(x)$ in the corresponding physical region of variable x [Samoilov et~al.(2005)Samoilov, Plyasunov, and Arkin]. Hence, the differential equation Eq. (17) is singular only at two points x_2 and x_1, which are the boundary points. One can find an asymptotic behavior of the steady state solution near these points:

$$\rho_1 \sim (x - x_2)^{a_2} (x_1 - x)^{a_1} g(x), \tag{18}$$

where $g(x)$ is analytic function of x in the interval $[x_2, x_1]$, satisfying condition $g(x_2) = g(x_1) = 1$. The exponents a_2 and a_1 are

$$a_2 = \frac{\beta}{f_2(x_2)} - 1, \tag{19}$$

$$a_1 = \frac{\alpha}{f_1(x_1)} - 1. \qquad (20)$$

Therefore, if the conditions Eq. (5) are satisfied, one expects unimodal distribution. Otherwise, there exists at least one additional peak in the distribution. In this case of the slow switching rates the equation Eq. (17) predicts divergence of the solution at one or both boundary points x_2 and x_1. This is an indication that diffusion terms that we omitted for our estimate become relevant. The diffusion terms makes the overall distribution finite.

h. Acknowledgments

We thank Alex Elgart, Jian Liu, and Wei Min for useful discussions.

i. References

1. Lu, H. P.; Xun, L.; Xie, X. S. *Science* 1998, **282**, 1877–1882.

2. Chen, Y.; Hu, D.; Vorpagel, E. R.; Lu, H. P. *The Journal of Physical Chemistry B* 2003, **107**,7947–7956.

3. Tan, X.; Nalbant, P.; Toutchkine, A.; Hu, D.; Vorpagel, E. R.; Hahn, K. M.; Lu, H. P. *The Journal of Physical Chemistry B* 2003, **108**, 737–744.

4. Lu, H. P. *Acc Chem Res* 2005, **38**, 557–65.

5. Liu, R.; Hu, D.; Tan, X.; Lu, H. P. *J Am Chem Soc* 2006, **128**, 10034–42.

6. English, B. P.; Min, W.; van Oijen, A. M.; Lee, K. T.; Luo, G. B.; Sun, H. Y.; Cherayil, B. J.;Kou, S. C.; Xie, X. S. *Nat. Chem. Biol.* 2006, **2**, 87–94.

7. Rissin, D. M.; Gorris, H. H.; Walt, D. R. *J Am Chem Soc* 2008, **130**, 5349–53.

8. Wang, X.; Lu, H. P. *J Phys Chem B* 2008, **112**, 14920–6.

9. Chen, P.; Xu, W.; Zhou, X.; Panda, D.; Kalininskiy, A. *Chemical Physics Letters* 2009, **470**,151–157.

10. Chen, P.; Andoy, N. M. *Inorganica Chimica Acta* 2008, **361**, 809–819.

11. Roeffaers, M. B. J.; De Cremer, G.; Uji-i, H.; Muls, B.; Sels, B. F.; Jacobs, P. A.;De Schryver, F. C.; De Vos, D. E.; Hofkens, J. *Proceedings of the National Academy of Sciences* 2007, **104**, 12603–12609.

12. Xu, W.; Kong, J. S.; Chen, P. *Phys Chem Chem Phys* 2009, **11**, 2767–78.

13. Min, W.; Luo, G. B.; Cherayil, B. J.; Kou, S. C.; Xie, X. S. *Phys. Rev. Lett.* 2005, **94**, 198302.

14. Xing, J.; Kim, K. S. *Phys. Rev. E* 2006, **74**, 061911.194

15. Frieden, C. *Ann. Rev. Biochem.* 1979, **48**, 471–489.

16. Frieden, C. *J. Biol. Chem.* 1970, **245**, 5788–5799.

17. Ricard, J.; Cornish-Bowden, A. Eur*. J. Biochem.* 1987, **166**, 255–272.

18. Ainslie, J., G. Robert; Shill, J. P.; Neet, K. E. *J. Biol. Chem.* 1972, **247**, 7088–7096.

19. Zwanzig, R. *Acc. Chem. Res.* 1990, **23**, 148–152.

20. Austin, R. H.; Beeson, K. W.; Eisenstein, L.; Frauenfelder, H.; Gunsalus, I. C. *Biochemistry* 1975, **14**, 5355–5373.

21. Monod, J.; Wyman, J.; Changeux, J. P. *J. Mol. Biol.* 1965, **12**, 88–118.

22. Kern, D.; Zuiderweg, E. R. P. *Curr. Opin. Struc. Biol.* 2003, **13**, 748–757.

23. Volkman, B. F.; Lipson, D.; Wemmer, D. E.; Kern, D. *Science* 2001, **291**, 2429–2433.

24. Xing, J. *Phys. Rev. Lett.* 2007, **99**, 168103.

25. Min, W.; Xie, X. S.; Bagchi, B. *J. Phys. Chem. B* 2008, **112**, 454–466.

26. Goldbeter, A.; Koshland, D. E. *Proc. Natl. Acad. Sci. U.S.A.* 1981, **78**, 6840–6844.

27. Swain, P. S.; Elowitz, M. B.; Siggia, E. D. *Proc. Natl Acad. Sci. USA* 2002, **99**, 12795–12800.

28. Levine, J.; Kueh, H. Y.; Mirny, L. *Biophys. J.* 2007, **92**, 4473–4481.

29. Samoilov, M.; Plyasunov, S.; Arkin, A. P*. Proc. Natl. Acad. Sci. U.S.A.* 2005, **102**, 2310–2315.

30. Samoilov, M. S.; Arkin, A. P. *Nat Biotech* 2006, **24**, 1235–1240.

31. Lepzelter, D.; Kim, K. Y.; Wang, J. J *Phys Chem B* 2007, **111**, 10239–47.

32. Thattai, M.; van Oudenaarden, A. *Proc Natl Acad Sci U S A* 2001, **98**, 8614–9.

33. Barkai, N.; Leibler, S. *Nature* 1997, **387**, 913–917.195

34. Miller, C. A.; Beard, D. A. *Biophys J* 2008, **95**, 2183–92.

35. Xing, J.; Chen, J. *PLoS ONE* 2008, **3**, e2140.

36. Gillespie, D. T. *J. Phys. Chem.* 1977, **81**, 2340–2361.

37. Kepler, T. B.; Elston, T. C. *Biophys. J.* 2001, **81**, 3116–3136.

38. Gillespie, D. T. *J. Chem. Phys.* 2000, **113**, 297–306.

39. Warmflash, A.; Adamson, D. N.; Dinner, A. R. *J Chem Phys* 2008, **128**, 225101.

40. Rondelez, Y.; Tresset, G.; Nakashima, T.; Kato-Yamada, Y.; Fujita, H.; Takeuchi, S.; Noji, H. *Nature* 2005, **433**, 773–7.

41. Paulsson, J. *Physics of Life Reviews* 2005, **2**, 157–175.

42. Blake, W. J.; KAErn, M.; Cantor, C. R.; Collins, J. J. *Nature* 2003, **422**, 633–7.

43. Artyomov, M. N.; Das, J.; Kardar, M.; Chakraborty, A. K. *Proc Natl Acad Sci U S A* 2007, **104**, 18958–63.

44. Karmakar, R.; Bose, I. *Phys. Biol.* 2006, **3**, 200–8.

45. Qian, H.; Shi, P.-Z.; Xing, J. *Physical Chemistry Chemical Physics* 2009

46. Morishita, Y.; Kobayashi, T. J.; Aihara, K. *Biophys J* 2006, **91**, 2072–81.

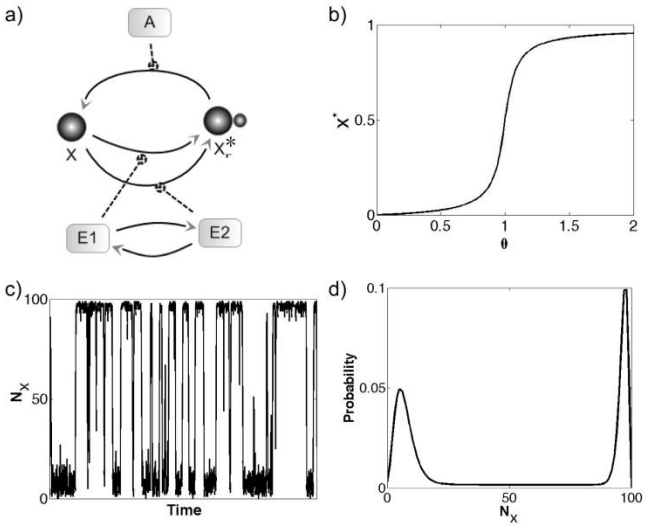

Figure 6.1 **A PdPC with a single kinase enzyme shows bimodal distribution of the substrate.** (a) Illustration of the PdPC. The kinase molecule has two slowly converting conformers with different enzyme activity. (b) The bulk response curve shows sigmoidal and monotonic zeroth-order ultrasensitivity. These results are obtained by solving the rate equations with the parameters given in Table 1. (c) A trajectory of the number of X with a single two state kinase. The total substrate number $N_{Xt} = 100$, conversion rate constant between two kinase states $\alpha = 0.001$, and other parameters are shown in Table 1. (d) The distribution of X corresponding to (c) shows bimodal distribution.

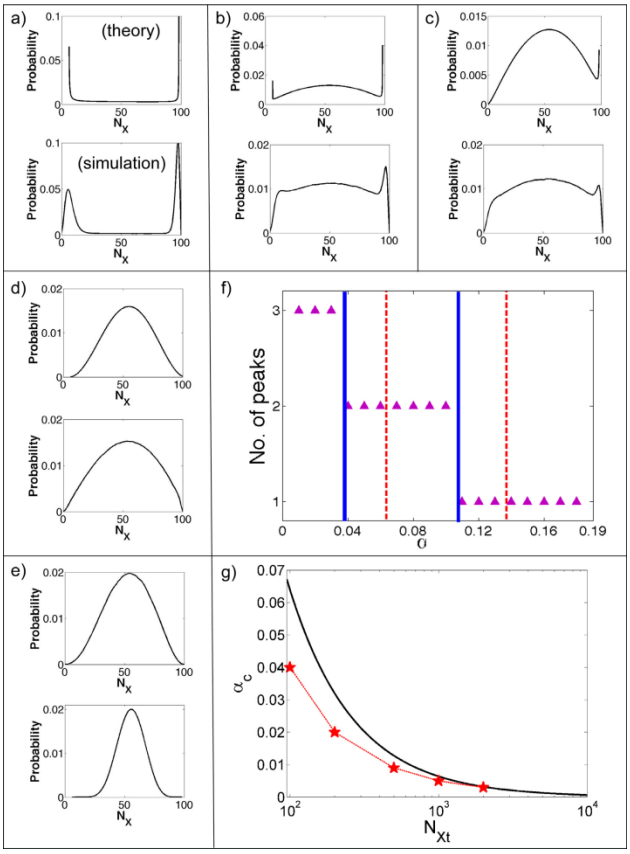

Figure 6.2 **Dependence of substrate distribution of a PdPC with a single two-state kinase enzyme on the kinase conformer conversion rates.** Total substrate molecule $N_{X_t} = 100$ unless specified otherwise. Simulation (s): lower, Theory (t): upper. For the parameters chosen, the theoretically predicted two critical points where the two peaks (singular points in the theory) disappear (Eq. (5)) are $\alpha_1 = 0.064, \alpha_2 = 0.137$. (a) $\alpha_t = \alpha_s = 0.001 << \alpha_1, \alpha_2$. (b) $\alpha_t = 0.055$ close to α_1. Corresponding $\alpha_s = 0.03$. (c) $\alpha_t = 0.064 = \alpha_1$. Corresponding $\alpha_s = 0.04$. (d) $\alpha_t = 0.137 = \alpha_2$. Corresponding $\alpha_s = 0.1$. (e) $\alpha_t = \alpha_s = 0.5 >> \alpha_1, \alpha_2$. (f) The number of peaks v.s. α (red stars). The vertical lines indicate the critical α values of peak disappearance from simulation (blue solid line) and theoretical prediction (red dashed line). The left blue solid line represents the disappearing of the first peak and the right blue solid line represents the disappearing of the second peak, leaving the distribution a single peak distribution. (g) The

simulated (stars with dashed line) and theoretically predicted (solid line) dependence of the critical α value on the total substrate number N_{Xt}. Numbers of all other species and the volume are increased proportionally to keep all the concentrations constant.

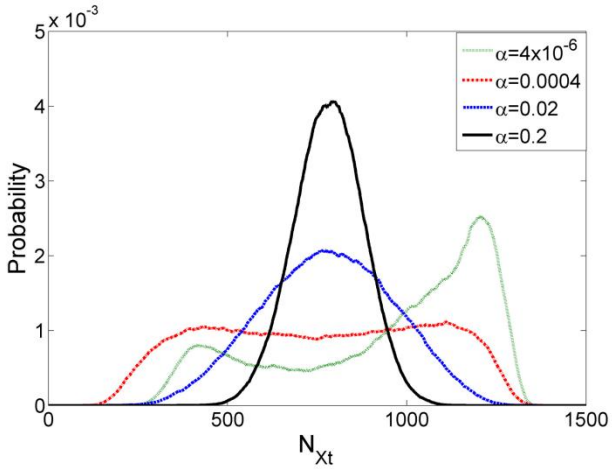

Figure 6.3 **A PdPC with 50 two-state kinase (and phosphatase) enzymes and 1500 substrates.** Other parameters are the same as in 1-enzyme case. the α values are: dotted line 4×10^{-6}, dash-dot line 0.0004, dashed line 0.02, and solid line 0.2.

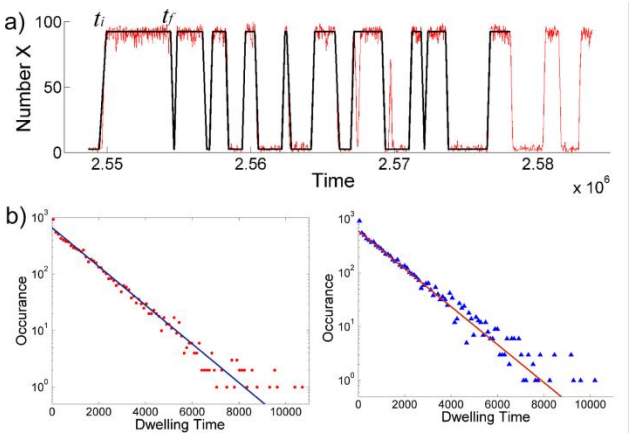

Figure 6.4 **Dwelling time distribution of a PdPC with a single two-state kinase enzyme** ($\alpha = 0.001$). (a) A typical trajectory with steps indicated (dark solid line). The initial and final times of one dwelling state are indicated as t_i and t_f, respectively. (b) The dwelling time distribution and exponential fitting of the upper (left panel) and lower (right panel) states. The fitting slopes are -7.9×10^{-4} and -8.1×10^{-4}, respectively.

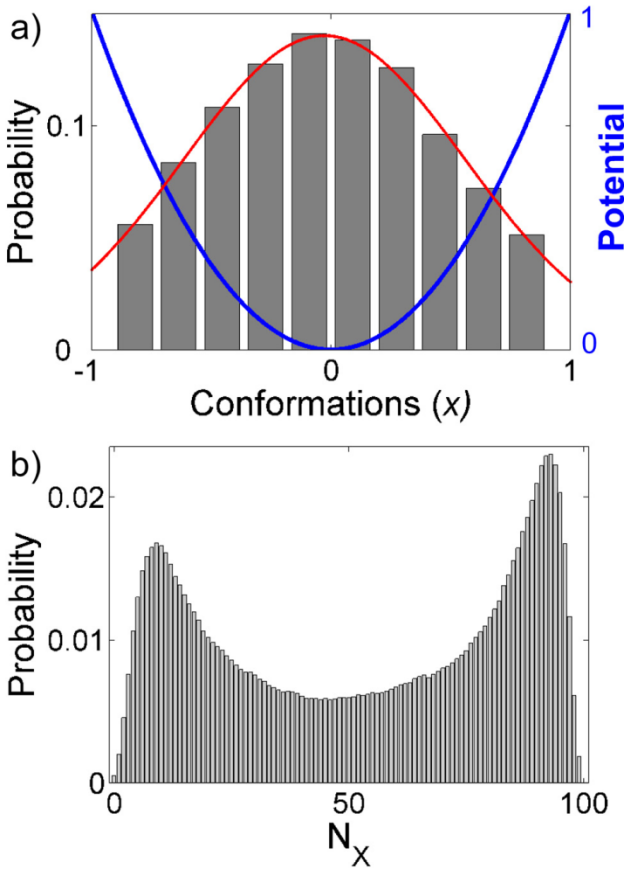

Figure 6.5 **Multi-State Enzyme fluctuation produced bimodal distribution.** (a) Enzyme conformation fluctuation along a harmonic potential (blue line) and the Boltzmann distribution (gray bars and red line). (b) The corresponding bimodal distribution of reactant X .

Parameters	Values
rate constant	in reduced unit
k_{1f}	50
k_{+f}	1.6
$k_{1f'}$	50
$k_{+f'}$	0.4
k_{2f}	50
k_{-f}	1
Free energy	in k_BT
$\Delta\mu_{ATP}$	–20
μ_{E1_X}	0
μ_{E1X}	–5
μ_{E1_X*}	0
μ_{A_X*}	0
μ_{AX*}	–5
μ_{A_X}	0
μ_{E2_X}	0
μ_{E2X}	–5

* See Appendix A

Table 6.1: **Simulation parameters**

Chapter 7

Conclusions and Future Work

In this work, I utilize the principles of statistical physics to understand selected biological process both in cellular and molecular level. The work on microtubule dynamics and mechanical response opens a new window to the potential novel drug design as well as extending the understanding of microtubule-related cellular behavior, for instance, cytoskeleton and mitosis. The thermodynamic and molecular mechanical analysis on microtubule dynamics and mechanical behavior demonstrate an effective way to couple the skills in statistical physics and problems in biological processes. Dynamic disorder analysis fills the gap between the research on macromolecular behavior and the system biology research on complex networks. We are able to demonstrate that the fluctuations in the single molecular level can have important consequences on network dynamics. This work opens a new path on network dynamic analysis.

Dynamic instability is a prominent property of MT dynamics. It has long been proposed that a GTP cap (i.e., one or a few layers of GTP-bound tubulins at the ends) is necessary for MT stability. Theoretical analysis also supports this model [1, 2]. In the model of VanBuren et al., the “sheet” structure was determined to be just an incomplete portion of an MT [2]. This model predicts that a “sheet” structure destabilizes an MT. They predict that “the sheet-like microtubules are more likely to be an intermediate to catastrophe than blunt-end microtubules”. Our hypothesis is just the opposite: the sheet-like structure is more likely to be an intermediate for the assembly process.

To study the effect of the GTP caps, Walker et al. used an ultra-violet microbeam to cut the ends of elongating MTs [3]. With the plus end cut off, an MT quickly shortens. With the minus end cut off, however, an MT resumes elongation. The plus and minus ends start with $\beta-\beta$ lateral and $\alpha-\alpha$ lateral bonds, respectively. Nogales et al. suggested that the minus end may not need a cap if the $\beta-\beta$ lateral bond for the GDP-tubulin is weaker than the $\alpha-\alpha$ lateral bond [4]. Molodtsov et al. argued against this proposal based on many experimental observations that the minus end depolymerizes faster than does the plus end [1]. However, their model in turn has difficulty explaining the experiment of Walker et al. The sheet structure introduces further asymmetry to the two ends since the elongation rates (and, thus, the sheet length) are different. This result implies that a faster depolymerization rate at the minus end does not necessarily rule out the proposal of Nogales et al. We will examine the dependence of MT stability on the sheet length and strength of lateral bonds.

MAPs consistent play important roles in microtubule behavior. There are many proteins that interact with microtubules *in vivo* to modify microtubule mechanical/chemical properties and assembly/disassembly dynamics. To understand a process as complex as MT dynamics, one has to start with simpler and better-controlled situations. With a model for unmodified microtubules developed, effects of MAPs can be added onto the model as external perturbations. This procedure allows us to separate the effect of the MAPs from the intrinsic mechanical and dynamic properties of the tubulin assemblies. VanBuren et al. studied the effect of XMAP215 on the microtubule elongation and shortening dynamics [2]. They introduced the effect of XMAP215 as modifying the

longitudinal and lateral bond strengths. We will examine how the dynamics and mechanical behaviors are affected by MAPs.

Currently, most of the sheet structures are observed *in vitro* (but not all, see [5]). A question may arise as to whether the sheet structures can be formed *in vivo*. A full investigation is clearly beyond the scope of this proposal and the capacity of modeling as well. But we can still partially address this question. We will examine the assembly/disassembly dynamics under physiological conditions (tubulin concentration, GTP/GDP concentrations, with and without various MAPs). Our model studies will predict whether one can observe the sheet structures at these conditions and how the size of sheet structure depends on various conditions (tubulin concentration, etc.).

In the area of dynamic disorder, we want to point out that some early experimental evidence for protein fluctuating dynamics was provided by Linderstrom-Lang and his amide proton hydrogen-deuterium exchange method [6-8]. The method is widely used to study protein folding dynamics. In recent years, inspired by the resurgent interest in dynamic disorder, which has redefined the field of protein dynamics, protein dynamics has become a focused research area.

Another related active research area explores how an enzyme evolves to acquire new catalytic function. “Many enzymes evolved from pre-existing enzymes via gene duplication” [9]. Precursor proteins are suggested to be conformationally heterogeneous, which is related to the dynamic disorder phenomenon; a new enzyme evolves through constraining protein heterogeneity and protein dynamics [10].

Systems biology is currently an active research field within cellular biology. It studies

how cells maintain their normal functions through interaction networks of biomolecules. The area is claimed as the “science of the 21st century”. People hope that research in the field may lead to fundamental understanding of important cellular processes and revolution of medical sciences. Researches in this field grow at an exploding rate, so I only provide a few representative references here [11-17]. A large focus has been on how the way biomolecules interact with each other (the topology of the network) couples to the cellular functions. All existing studies treat each biomolecular species as a node in the interconnected network without internal structure. However we suggest that biomolecules like proteins may have complex internal dynamics, and serve as functional motifs. The enzyme dynamic properties under molecular level may couple to the dynamics at network levels. The coupling may result in emergent new dynamic phenomena, and play important physiological functions [18]. This was also conjectured by biochemists [19], but has so far remained unexplored. Our research will be an important step to fill this gap.

References

1. Molodtsov, M.I., et al., *A molecular-mechanical model of the microtubule.* Biophys. J., 2005. **88**(5): p. 3167-3179.
2. VanBuren, V., L. Cassimeris, and D.J. Odde, *Mechanochemical Model of Microtubule Structure and Self-Assembly Kinetics.* Biophys. J., 2005. **89**(5): p. 2911-2926.
3. Walker, R.A., S. Inoue, and E.D. Salmon, *Asymmetric behavior of severed microtubule ends after ultraviolet-microbeam irradiation of individual microtubules in vitro.* J. Cell Biol., 1989. **108**(3): p. 931-937.

4. Nogales, E., et al., *High-Resolution Model of the Microtubule.* Cell, 1999. **96**(1): p. 79-88.

5. McIntosh, J.R., et al., *Fibrils Connect Microtubule Tips with Kinetochores: A Mechanism to Couple Tubulin Dynamics to Chromosome Motion.* Cell, 2008. **135**(2): p. 322-333.

6. Linderstrom-Lang, K., *Deuterium exchange between peptides amd water*, in *The Chemical Society's Special Publication No. 2*1955.

7. Englander, L.M., Y. Bai, and T.R. Sosnick, *Hydrogen exchange: the modern legacy of Linderstrom-Lang.* Protein. Sci., 1997. **6**(5): p. 1101-1109.

8. Qian, H. and S.I. Chan, *Hydrogen exchange kinetics of proteins in denaturants: a generalized two-process model.* J. Mol. Biol., 1999. **286**(2): p. 607-616.

9. O'Brien, P.J. and D. Herschlag, *Catalytic promiscuity and the evolution of new enzymatic activities.* Chem. Biol., 1999. **6**(4): p. R91-R105.

10. Zimmermann, J., et al., *Antibody evolution constrains conformational heterogeneity by tailoring protein dynamics.* Proc. Natl Acad. Sci. USA, 2006. **103**(37): p. 13722-13727.

11. Rao, C.V., D.M. Wolf, and A.P. Arkin, *Control, exploitation and tolerance of intracellular noise.* Nature, 2002. **420**(6912): p. 231-237.

12. Suel, G.M., et al., *Tunability and noise dependence in differentiation dynamics.* Science, 2007. **315**(5819): p. 1716-1719.

13. Cluzel, P., M. Surette, and S. Leibler, *An Ultrasensitive Bacterial Motor Revealed by Monitoring Signaling Proteins in Single Cells.* Science, 2000. **287**(5458): p. 1652-1655.

14. Barkai, N. and S. Leibler, *Robustness in simple biochemical networks.* Nature, 1997. **387**(6636): p. 913-917.

15. Janes, K.A., H.C. Reinhardt, and M.B. Yaffe, *Cytokine-Induced Signaling Networks Prioritize Dynamic Range over Signal Strength.* Cell, 2008. **135**(2): p. 343-354.

16. Gardner, T.S., et al., *Inferring genetic networks and identifying compound mode of action via expression profiling.* Science, 2003. **301**(5629): p. 102-105.

17. Brandman, O., et al., *Interlinked fast and slow positive feedback loops drive reliable cell decisions.* Science, 2005. **310**(5747): p. 496-498.

18. Xing, J. and J. Chen, *The Goldbeter-Koshland Switch in the First-Order Region and Its Response to Dynamic Disorder.* PLoS ONE, 2008. **3**(5): p. e2140.

19. Frieden, C., *Kinetic Aspects of Regulation of Metabolic Processes. The hysteretic enzyme concept.* J. Biol. Chem., 1970. **245**(21): p. 5788-5799.